Dynamic Modeling and Optimization of a Continuous Fluidized Bed Process for the Separation of Enantiomers by Preferential Crystallization

Dissertation
zur Erlangung des akademischen Grades

Doktoringenieurin
(Dr.-Ing.)

von M.Sc. Nadiia Huskova
geb. am 13.01.1994 in Donezk, Ukraine

genehmigt durch die Fakultät für Verfahrens- und Systemtechnik
der Otto-von-Guericke-Universität Magdeburg

Promotionskommission: apl. Prof. Dr. rer. nat. Heike Lorenz (Vorsitz)
Prof. Dr.-Ing. Andreas Seidel-Morgenstern (Gutachter)
Prof. Dr.-Ing. Michael Mangold (Gutachter)
Prof. Dr.-Ing. Andreas Bück (Gutachter)

eingereicht am: 05.01.2022
Promotionskolloquium am: 29.04.2022

Abstract

This thesis is concerned with investigating a purification process of chemical compounds called enantiomers using kinetically controlled preferential crystallization in fluidized beds. Attention is paid to three main aspects - the analysis of the crystallization process, its modeling, and subsequent application of the developed model to improve the process performance.

Typically, particles are not uniform, and different properties, such as size, shape, and internal composition, are distributed over the particle population. The distribution of these properties may significantly impact the process performance. Modeling crystallization processes in a simple way, such as calculating just yield using thermodynamics, does not provide important information about system evolution. In combination with the process kinetics, the Population Balance concept is applied in this study to construct a model and predict the crystal size distribution. The developed model describes the interaction between crystal growth, particle transport, and fluid dynamics in the non-isothermal case. In contrast to previous studies, the model equations distinguish between the target and the counter-enantiomer. Thus, the productivity of the process and the purity of the product can be evaluated. According to experimental conditions, periodic crystals removal is implemented based on the height of the fluidized bed. The results of the laboratory experiments generated in a parallel doctoral research project allowed the model validation using a racemic mixture of asparagine monohydrate and water as the solvent. Based on the good quantitative agreement between the experimental and simulation results, general conclusions are drawn to highlight the significant potential of the model. Moreover, the research identified the relevant operational parameters to ensure that the process is highly productive. The relevance of the model parameters is studied by performing a local sensitivity analysis. To assess the parameter influences, a normalized sensitivity function is applied. Using the results of the sensitivity studies, model-based process optimization is performed to improve process efficiency. The steady-state optimization, considering imposed constraints, made it possible to design an efficient set of geometry and operating conditions based on the attainable regions. It is demonstrated that the proposed optimal design of the crystallizer setup increases productivity, and additionally, it allows the absence of contamination in the final product.

This dissertation primarily demonstrates the applicability of the developed model of preferential crystallization in a fluidized bed to simulate the enantioseparation process. The performed numerical optimization provides recommendations for experimenters regarding efficient producing particles with predefined characteristics.

Kurzzusammenfassung

Diese Arbeit untersucht Reinigungsverfahren von chemischen Verbindungen, die Enantiomere genannt werden, unter der Verwendung einer fortschrittlichen Technik der kinetisch kontrollierten Kristallisation in Wirbelschichten. Dabei konzentriert sich die Arbeit auf die folgenden drei Aspekte: Die Analyse des Kristallisationsprozesses, dessen Modellierung und die anschließende Anwendung des entwickelten Modells zur Optimierung des Prozesses.

In aller Regel sind Partikel nicht einheitlich und deren verschiedene Eigenschaften, wie Größe, Form und die innere Zusammensetzung verteilen sich auf die gesamte Partikelpopulation. Die Verteilung dieser Eigenschaften kann erhebliche Auswirkungen auf die gesamte Prozessleistung haben. Eine Modellierung von Kristallisationsprozessen in einer vereinfachten Weise, wie z.B. zur bloßen thermodynamischen Berechnung der Ausbeute, liefert keine aussagenkräftigen Informationen über Details der Entwicklung im System.

Populationsbilanzen in Verbindung mit kinetischen Ausdrücken werden in diese Arbeit verwendet, um ein Modell zu konstruieren und die Kristallgröß enverteilungen vorherzusagen. Das entwickelte eindimensionale Modell beschreibt die Wechselwirkung zwischen Kristallwachstum, Partikeltransport und einer nicht isothermen Strömungsdynamik. Im Gegensatz zu früheren Studien und Arbeiten unterscheiden die Modellgleichungen zwischen dem Ziel- und dem Gegenenantiomer. So können die Produktivität des Prozesses und die Reinheit des Produktes bewertet werden. Entsprechend den Versuchsbedingungen wird die periodische Kristallentnahme in Abhängigkeit der Wirbelschichthöhe durchgeführt. Die Laborergebnisse der in einer parall durchgeführten Doktorarbeit ermöglichen eine Modellvalidierung unter Verwendung einer razemischen Mischung aus L-Asparagin-Monohydrat und Wasser als Lösungsmittel. Basierend auf der quantitativen Übereinstimmung zwischen den Labor- und Simulationsergebnissen werden daraus allgemeine Schlussfolgerungen abgeleitet, um das signifikante Potenzial des Modells zu bestätigen.

Die Relevanz der Modellparameter wird durch eine lokale Sensitivitätsanalyse untersucht. Um die Einflüsse der verschiedenen Parameter zu bewerten, wird eine normierte Sensitivitätsfunktion verwendet. Anhand der Ergebnisse der Sensitivitätsstudie wird eine modellbasierte Prozessoptimierung zur Verbesserung der Prozesseffizienz durchgeführt. Die stationäre Optimierung, unter Berücksichtigung der bestehenden

Restriktionen, ermöglicht es Form und Abmessung der Apparaturen sowie den Betriebsbedingungen, basierend auf den erreichbaren Bereichen, festzulegen. Es wird gezeigt, dass der vorgeschlagene optimale Entwurf des Aufbaus der Kristallisationsgefäße die Produktivität erhöht und darüber hinaus Verunreinigungen im Endprodukt verhindert. Diese Dissertation demonstriert die Anwendbarkeit des entwickelten Modells des ausgewählten Kristallisationprozesses in einer Wirbelschicht, um den Enantioseparationsprozess mit ausreichender Genauigkeit zu simulieren. Die durchgeführte numerische Optimierung ermöglicht es, Empfehlungen zu den Parametern der Apparate sowie den Betriebsparametern zu formulieren, um die Gewinnung von Partikeln mit bestimmten Eigenschaften sicherzustellen.

Table of Content

Introduction

Achieved over the last decades, improvements in technology and scientific capabilities in the pharmaceutical industry have allowed the development of drugs to treat various diseases. However, the process of bringing new medicines to market requires long-term clinical trials and investigations for delayed side effects. Development, preclinical phase, clinical trials, and regulatory approval of a new molecule take an average of 11.8 years (Deore et al., 2019). More and more patients are involved in research to obtain representative statistics, causing the average cost to rise steadily. In this regard, spatial isomers of already discovered drugs have significant research potential - compounds with the same molecular structure but differing in the arrangement of atoms in space (Chhabra et al., 2013). The current research in the chemical and pharmaceutical industries mainly focuses on studying the pharmacological properties of configurational spatial isomers of medicinal substances, including optical and geometric isomerism (Coutts and Baker, 1989).

The presented work focuses on chiral compounds characterized by optical activity. Enantiomers are very similar to each other, but they are not identical. The target and the counter-enantiomer have the same composition of molecule groups but differ in relative position in space (McConathy and Owens, 2003). The difference in enantiomer's structure is evident when superimposing their models on each other. Enantiomers have the same physical and chemical properties (boiling point, melting point, solubility, electrical conductivity, etc.). Still, depending on the orientation, enantiomers react differently with other chiral compounds - this explains their difference in physiological action. Chemical synthesis typically produces a 50:50% racemic mixture of enantiomers, separation of which is crucial for many applications. The meaning of dividing chiral substances into racemic conglomerate - dextrorotatory and laevorotatory - is that one of the enantiomers may be biologically inactive or less active, differs in metabolic pathways, and cause undesirable side effects (Eichelbaum, 1995).

Thalidomide case, detailed discussed in Chapter 2 of this work, has become tragic evidence of the importance of the chirality of molecules for the safety treatment (Tokunaga et al., 2018). In the early 1960s, this medicine was prescribed to pregnant women with insomnia and morning sickness (Eichelbaum, 1995). Earlier studies confirmed that the laevorotatory form of thalidomide had a sedative effect. Later it was discovered that the dextrorotatory form caused teratogenic effects. Due to the introduction of racemic formula to the market, thousands of children have been born with phocomelia. The thalidomide tragedy could have been avoided if the "wrong" D-form had been removed during clinical trials.

The operation of dividing racemic mixtures into their constituent optically active components is called separation. If at least one enantiomer can be isolated in pure form, the separation is called complete; otherwise, it is stated that the optically active compound contains an impurity of the second enantiomer (Wei et al., 2017). The separation of mixtures into sterically pure compounds is a difficult task that requires advanced separation techniques when microbiological, enzymatic, chemical, and other methods could be applied.

Crystallization processes discussed in Chapter 2 of this work have been demonstrated to be a promising approach to a posed separation problem. Under equilibrium conditions, both enantiomers are formed from racemic mixtures as enantiomorphic crystals. It does not matter whether the crystallization process occurs spontaneously at a low rate or if crystal seeding accelerates it. However, only the preferential crystallization approach based on seeding the crystallizer with particles of the desired enantiomer is discussed within the scope of this study.

In Chapter 2 of this work, a discussion on the properties of enantiomers is given, and an investigation of the variability of crystallization processes is described. The ternary solubility phase diagram is used to determine the conditions under which crystallization can occur. The initial phase must be supercooled or overheated due to the formation of a new phase when firstly, crystallization centers are formed, which turn into crystals and grow, changing the shape. Crystallization centers arise homogeneously in the volume of the initial phase and heterogeneously on the surfaces of foreign solid particles (primary nucleation) and near the surface of previously formed crystals of a new phase (secondary nucleation) (L’vov and Umantsev, 2021). Later, in Chapter 2, thermodynamic aspects of crystallization are discussed, and an example of the determination of the solubility isotherms is provided.

Crystallization begins at specific centers with nuclei, which are unit cells of the crystal lattice (Tóth et al., 2012). Each size of the initial solid crystals corresponds to a particular saturation value: the smaller the nucleus, the larger is saturation. The number of particles arising per unit time depends on the process conditions, while the spontaneous nucleation of crystals in a supersaturated solution depends on the residence time of the solution in the reactor. When the rate of nucleation is greater than the growth rate, a large number of small crystals are formed. Thus, changing the factors affecting the nucleation and growth rate makes adjusting the desired crystal size distribution possible. The size of the crystals is essential for subsequent processing - drying, settling, rinsing, and retaining moisture are easier with large crystals. In addition, the demand for adjustable crystal size is supported by industrial applications, and many studies reflect attempts to provide an efficient mechanism for controlling crystal size distribution (Igarashi and Ooshima, 2020; Paroli, 2012; Burcham and Jarmer, 2013). Thus, this work is concerned with studying a promising concept of fluidized bed crystallization (Binev et al., 2016), which is characterized by the ability to avoid undesirable particle size distribution.

Various amino acid systems relevant to the industry have been investigated to demonstrate the effectiveness of such a separation process, forming simple eutectic systems (Midler, 1975, 1976). The process concept of a fluidized bed relies on the fact that, under appropriate conditions, a defined quantity of crystals placed inside a reactor behaves like a fluid due to uprising solution flow. Seeding material is introduced by ultrasonic comminution, which grinds the large crystals to maintain the process continuity. Previous works (Binev, 2015; Temmel et al., 2018) devoted to the study of continuous crystallization in a fluidized bed confirmed the efficiency of the process and served as the basis for this thesis. The second Chapter concludes with an analysis of the setup for continuous preferential crystallization.

Following the discussion of the equipment required for continuous separation in fluidized beds, the narrative turns to process modeling. Designing a coupled continuous crystallization process has many degrees of freedom. Due to the relatively small operation window, the free operation and design parameters should be carefully selected. To study process behavior and predict characteristics of the crystallized material, a process model must be sufficiently detailed to capture all relevant parameters of the design process. Additionally, the numerical effort required to solve and optimize the model equations should not be too high. Models, which offer a reasonable compromise between these conflicting objectives, have been published (Mangold et al., 2015; Mangold et al., 2016; Binev, 2015). It can be shown that the process model presented in the following is based on the previous studies and refines several aspects of existing models.

Describing the interaction between crystal growth, particle transport, and fluid dynamics in the non-isothermal case, the model allows to evaluate not only the productivity of the process but also the purity of the withdrawn product due to distinguishes between the L- and the D-enantiomer and implementation of the empirical threshold to access nucleation.

A challenging aspect fully described in Chapter 3 is related to the modeling of the pulse-wise product withdrawal. The objective here is to find a simple yet sufficiently precise description for taking a fluid segment periodically out of the crystallizer by analyzing the arrangement of crystals in the reactor. The proposed model follows the widely used population balance approach (Hulburt and Katz, 1964) when not single particles are modeled, but the properties of a particle population consist of an infinite number of individuals. Using the PB equations, all the necessary characteristics can be calculated, and the effectiveness of the simulation can be determined by comparing the simulation results with laboratory experiments in Chapter 4.

Case study

To demonstrate the applicability and performance of the fluidized bed approach, the model study is performed with the chiral amino acid asparagine (C4H8N2O3, abbreviated as Asn). L-Asparagine (from now on referred to as L-Asn) is an amino acid used to treat various brain, liver, and kidney problems. L-Asn is biosynthesized from Aspartic acid and Ammonia by asparagine synthesis (Jaques et al., 1981).

According to historical records, asparagine was the first amino acid to be isolated. For the first time, it was done in 1806 in a crystalline form from asparagus juice (Annales de chimie, 1806) which most likely served as a prerequisite for the chosen name. However, asparagus was not the only source from which synthesis of asparagine was possible. A few years after, in 1809, a substance with very similar properties has been extracted from licorice root (Annales de chimie, 1809). Nowadays, it is well known that in nature, mostly L-asparagine can be found in plant sources such as soy, potatoes, nuts, and animal sources - eggs, fish, and seafood.

Determining the structure of asparagine also required a few decades of intensive research. The first formulation was done in 1833 (Petroianu, 2010). The final structure was discovered in 1888 due to D-asparagine isolation (Gal, 2012). Italian chemist Arlando Piutti for the first time, isolated D-Asparagine, the enantiomer known before L-Asparagine. Using an ingenious synthetic scheme, he investigated the resulting component and made conclusions about the chirality of asparagine. Piutti noticed the differences in the properties of the components, such as the taste of asparagine: L-Asparagine was without taste, while its counter-enantiomer was sweet. This study, based on the difference in the human sense of smell, led to the conclusion about the chirality of asparagine. D-type is much less common in nature. However, it can be found in some microorganisms and pea seedlings.

Asparagine crystallizes from aqueous solutions as a monohydrate. Several works have shown that this single-crystal material undergoes a structural phase transition under high pressure and low temperature (Moreno and Soriano-García, 1999). Taking into account the proposed concept of the fluidized bed crystallization, racemic asparagine monohydrate (Asn·H2O) and the respective enantiopure D- and L-Asn·H2O was chosen as modeled chiral system. In this work, the amino acid is present as an optically active molecule with two mirror enantiomers called L-Asn or D-Asn. In the literature, it is possible to find other names as (S) or (+) for the L enantiomer, while (R) or (-) for the D (Meierhenrich, 2008).

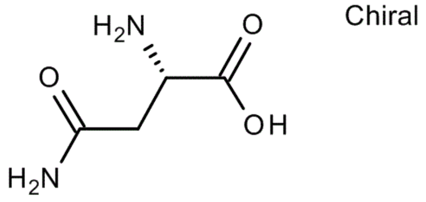

Figure 1.1 Structural formula of the asparagine enantiomers.

Asparagine monohydrate is a white crystalline powder. Furthermore, the physical and chemical material properties of the studied enantiomers are identical, and some of them are summarized in Table 1.1.

Table 1.1 Physical and chemical material properties

Molecular formula	$C_4H_8N_2O_3$
Molar mass	132.12 $[gmol^{-1}]$
Appearance	crystalline powder
Density	1540 $[kgm^{-3}]$
Melting point	235 [°C]

The required thermodynamic properties characterize the phases are summarized in Table 1.2.

Table 1.2 Thermodynamic properties of the phases

Heat capacity of the solid phase at 24°C (Binev et al., 2016):	$c_{p_{solid}}$	1372 $[Jkg^{-1}K^{-1}]$
Average heat capacity of the aqueous solution:	$c_{p_{liquid}}$	4180 $[Jkg^{-1}K^{-1}]$
Density of the solid phase at ambient temperature (Köllges and Vetter, 2018):	ρ_{solid}	1540 $[\mathrm{kg\ m^{-3}}]$
Average density of the liquid phase (own measurement):	ρ_{liquid}	1010 $[\mathrm{kg\ m^{-3}}]$
Process enthalpy (Jaques et al., 1981):	ΔH_{cryst}	$-229\ [kJkg^{-1}]$

Solubility data of the system

A fundamental study of the solubility of the D-/L-Asn·H2O system was described in detail (Petrusevska-Seebach, 2012). Additional analyses were performed and summarized later in (Gänsch, 2017). The obtained data about the solubility of different mixtures of D-/L-Asn·H2O system and water used as a solvent is presented in Figure 1.2. In the course of the study, the interval from 15℃ to 45℃ was covered. As shown in Figure 1.2(a), as the temperature rises, solubilities increase. The system indicates nearly ideal behavior - the ratio between the mass fractions of the racemic mixture and the pure enantiomer is about 2. Thus, the solubility of one enantiomer shouldn't be influenced by the presence of the other enantiomer.

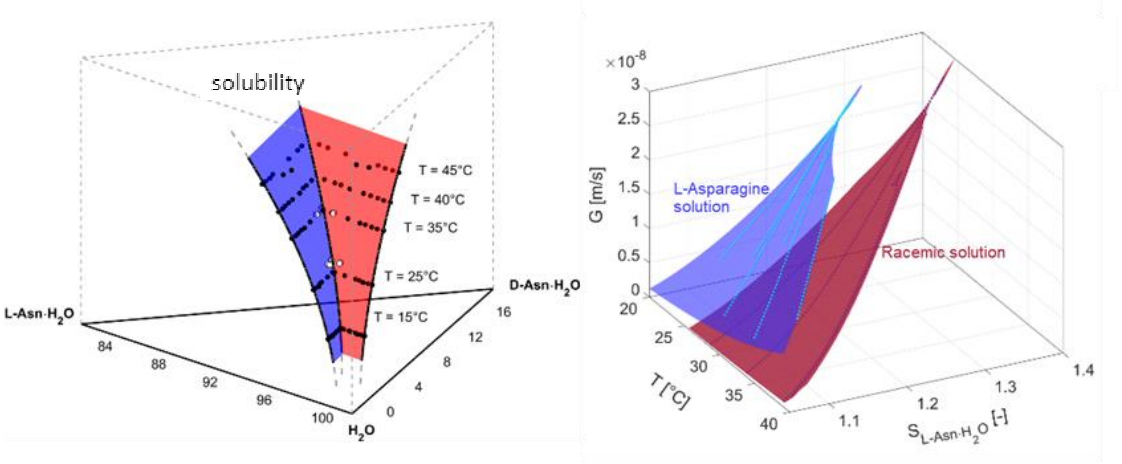

Figure 1.2 Solubilities presented as a function of temperature in the ternary L-Asn·H2O/D-Asn·H2O/water system. All axes are given in mass fractions ×100 (wt%) (left). Growth kinetics of L-Asn·H2O seed crystals from racemic and pure L-Asn solutions as functions of supersaturation, S, and temperature, T (right). (Figures adapted from (Petrusevska-Seebach, 2012) with copyright permission).

As it is known from the study (Temmel et al., 2018), the solubility courses for both enantiomers D- and L –Asn·H2O are almost identical. Compared to the work (Gänsch, 2017), the study described in (Temmel et al., 2018) shows differences in measurements above 50 °C. For the current study, the reference temperature is considered to be between 30 °C and 40 °C.

Kinetic data for the studied chiral system

The estimation procedure of the growth kinetics from racemic asparagine solutions and the nucleation/growth kinetics from pure L-Asn solutions is provided in (Binev, 2015). Referring to (Gänsch, 2017), nucleation and growth parameters could be used to assess the driving force of crystallization. The growth rates in enantiopure solution exceed those in racemic solution over the entire region of supersaturations and crystallization temperatures studied. The growth rate (G) for a given supersaturation (S) and temperature (T) can be calculated for the system using the following equations.

$$G = k_g \cdot (S-1)^{n_g} \cdot \exp \cdot \left(-\frac{E_g}{R \cdot T}\right), \tag{1.1}$$

where $k_g = 8.43 \cdot 10^6\ ms^{-1}, n_g = 2.47, E_g = 76.74\ kJmol^{-1}$.

The listed kinetic parameters, adapted from (Temmel et al., 2018), pertaining to the studied chiral system must be corrected if the thermodynamic properties change. Further kinematic theories can be found in the literature (Mullin, 2001). A broad study of the kinetics of asparagine can be found in (Petrusevska-Seebach, 2012). In Chapter 4, all characteristics of the study system are used to demonstrate and validate the developed model. All calculations are performed using the crystallizer geometry introduced in (Gänsch et al., 2021).

After the validation step, the model study procedure examines the dependence of the process productivity and crystal size on the height of the fluidized bed. Local sensitivity analysis is performed to determine a set of parameters that can be optimized to improve process performance. For a better understanding, all the parameters are divided into groups, each of the groups represents thermodynamic, operating, geometrical, and modeling parameters, respectively. Chapter 4 concludes by identifying the most influential parameters for subsequent model-based process optimization.

In Chapter 5, a systematic model-based optimization approach to improve the Continuous crystallization of asparagine monohydrate in a fluidized bed reactor is given. This Chapter begins with the literature review briefly introduces the current stage in model-based control of crystallization and methodology for obtaining optimal solutions. The steady-state optimization, considering imposed technical and kinetic constraints, is proposed to design an efficient set of operating and geometrical crystallization conditions. The empirical approach to assessing product contamination factors is considered in particular. In addition to the mathematical optimization problem of finding relevant parameters, this work aims to optimize the resources needed to obtain numerical solutions. Due to their ability to speed up the procedure of finding numerical solutions, a parallel version of the genetic algorithm and multiprocessing computations are considered. Lastly, this work concludes with the model-based optimization results and final remarks given in Chapter 6.

Part 1. Chirality, crystallization, and process modeling

The first part of this work contains fundamental knowledge about separation processes that purify fluids by forming solids, problems when separating enantiomers, aspects of the crystallization technique, its driving forces, and thermodynamic aspects. Chapter 3 explains the basic processes modeling approaches and diagrams of the model constituents and their dependencies. A model predicting the overall behavior of enantiomers with preferential crystallization in a fluidized bed in the non-isothermal case is developed and described. A general environment for understanding and modeling the crystallization process is proposed and described without specifying a particular chemical system.

2. Background

The main object of this Chapter is to discuss important theoretical aspects of the crystallization process, emphasizing chiral compounds and approaches for their purification. Chapter 2 begins with information about enantiomers and their structural features. Ternary phase diagrams are given and discussed as a research tool for providing a fundamental understanding of separation experiments. Due to the relevance of Solid-Liquid Equilibria diagrams in the chemical engineering community, this approach will help us to understand the basic idea behind the enantioselective crystallization process studied within this work.

The crystallization process is characterized by two essential phenomena, nucleation, and crystal growth, driven by the compound's thermodynamic and chemical properties. The particular influence of nucleation and growth is discussed to understand and properly operate the process within the metastable zone. To build up an understanding of the crystallization process, it is necessary to gain knowledge about the concepts involved. Later in Chapter 2, meaningful information about process variances is given, and recently developed crystallization techniques are analyzed. Finally, Chapter 2 reviews the basic principles of crystallization in a fluidized bed. Agreeing with a fluidized bed approach, the following Chapter 3 is devoted to the general model development.

Problem statement

More than ten million substances have been created in organic chemistry over the past two centuries (Dengale et al., 2016). The synthesis of new organic compounds is becoming more and more widespread, which is explained primarily by the need to solve fundamental problems, for example, to identify the relationship of a chemical substance with its reactivity. On the other hand, high demands from society also encourage the rapid development of organic chemistry. One of the reasons is the need for an arsenal of affordable and effective drugs to prevent and treat diseases. Chemists and pharmaceutical researchers are working together to resolve this challenge.

New medication must meet a number of stringent requirements. First of all, the substance must have high activity, selectivity, and duration of the therapeutic effect. Furthermore, the substance should be characterized by high purity and storage stability. The cost of production should not be too high, and the profitability upon sale, in contrast, should be significant. All these factors determine the lifetime of the drug among similar drugs that exist on the market. Toxicological studies of a potential drug receive the most serious attention.

Consequently, the time between conception in the laboratory and product launch on the market is significantly longer. The need for a thorough investigation of medication toxicity was first felt in the late 1960s when it was discovered that thalidomide presented in racemate form did not possess the required purity. The thalidomide tragedy (Speirs, 1962), which became infamous worldwide, as well as the subsequent failures with the use of ritonavir, drew the attention of scientists to the search for a compromise between the use of effective chiral compounds and the potential danger that arises from a poor understanding of their behavior.

Examples for the relevance of chirality

Thalidomide is responsible for one of the biggest medical disasters, causing various congenital disabilities in more than thousands of children worldwide between 1957 and 1962. Medicament consisting of thalidomide was mainly prescribed as a sleeping drug to pregnant women to relieve morning sickness. (Tokunaga et al., 2018). Later the use of thalidomide-containing medicaments was designated as the cause for malformation of the limbs in newborns. In 1962 thalidomide was banned in Germany over the next year worldwide. However, the unique pharmacological action against various diseases led to increased interest and research on thalidomide. It was later used in Israeli clinics to treat leprosy, and after a few decades, it was approved by the FDA and classified as an orphan drug (Wu et al., 2015). A comprehensive study of the current applicability of thalidomide is given in (Franks et al., 2004).

Another example associated with the use of chiral compounds is ritonavir (Louie, 2019). Initially, ritonavir was treated as an antiretroviral drug and used in advance Human Immunodeficiency Virus (HIV). Later on, like many other drugs, ritonavir showed polymorphism; its molecules could form more than one type of crystal. During development in 1996, only the form that is now called polymorphic form I was studied. A few years after, in 1998, polymorphic form II was discovered with significantly reduced solubility than the original crystal form. This more stable (and, accordingly, less soluble) crystalline form changed the bioavailability of the drug. Following this discovery in the late 1990s, Abbott (now AbbVie) took the original capsules off the market. This encouraged patients to switch to Norvir suspension while researchers worked to resolve the issue. Conventional tablets were replaced with gelatin capsules with a refrigerated storage condition to solve the crystallization of the starting material. In 2000, the American chemical-pharmaceutical corporation Abbott (AbbVie) received FDA approval for the Kaletra tablet formulation (called Lopinavir / Ritonavir), which contains ritonavir that does not require refrigeration (Louie, 2019).

Since chirality can affect drug stability, desired effects on the human organism, and bioavailability like in the discussed examples, it is of great interest in pharmaceutical development.

2.1 Enantiomers and racemic mixtures

In a general sense, chirality is a fundamental property of bulk objects. The term "chiral" was introduced at the end of the 19th century. It became firmly established in chemistry only in the 1970s due to the theoretical study of optically active substances. A chiral molecule does not match its mirror image. Two possible forms of mirror images are called enantiomers. Basically, in an achiral environment, the enantiomers of a chiral substance exhibit the same physical and chemical properties, but they rotate plane-polarized light into opposite directions and react at different rates with a chiral substance or with an achiral substance in a chiral medium. To summarize, optical isomers differ in two characteristics: their interaction with plane-polarized light and how they react with other chiral molecules. (Liu, 2021).

Optical activity of enantiomers

Optical isomerism has a history of over 200 years. The French physicist Malus discovered optical activity in 1808. Two light beams appear when ordinary light (oscillating in any of the planes intersecting the beam direction) passes through an Icelandic spar crystal (crystalline calcium carbonate). This phenomenon is known as birefringence: two beams of light are plane-polarized on mutually perpendicular planes, which means electromagnetic oscillations of each beam take place in the same plane (Anderson et al., 2020). In this case, the Nicolas prism acts as a light polarizer. The polarimeter has two Nicol prisms through which the light passes sequentially: if the prisms are parallel, the intensity of the transmitted beam does not decrease; if the angle between the prisms is sharp or obtuse, the beam intensity decreases. In 1813, the French physicist Biot discovered that several substances (such as sugar or turpentine), when placed between two Nicol prisms, change the angle at which the extinction of light is observed. Based on these studies, Biot demonstrated that light is polarized differently by the substances studied (Asimov, 1994). The optical activity of isomers was discovered when the second prism (originally perpendicular to the first) was rotated by the same angle. When the effect is detected only in a solid state of a compound, it is evident that rotation is a property of the crystal. Figure 2.1 shows how the plane-polarized light has been rotated when passed through to the isomers.

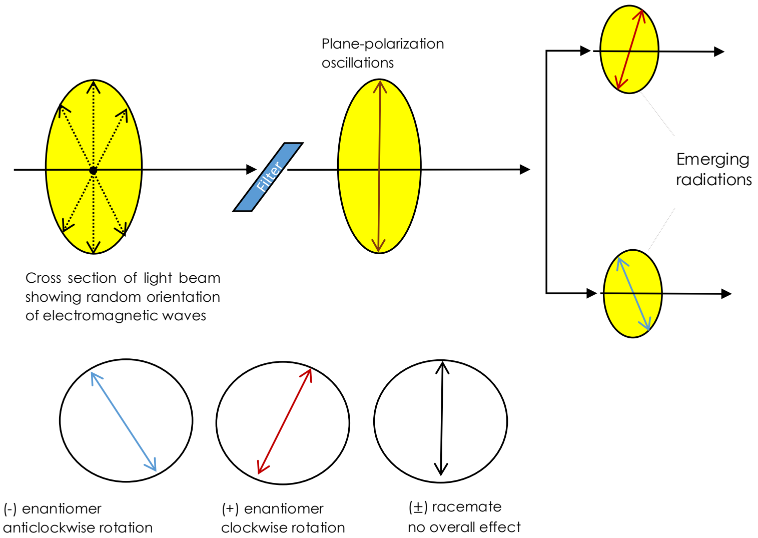

Figure 2.1 Demonstration of the interaction of enantiomers with plane-polarized light.

Pasteur made essential discoveries in stereochemistry in the late 19th century (Gal, 2019). The scientist was aware of two acids isolated from sediment in wine barrels: tartaric acid, which rotates the polarization plane to the right [now called (+) tartaric acid], opposite to this (-) tartaric acid, and racemic acid, which does not rotate [now called (±) tartaric acid]. Considering crystalline salts of (+) tartaric acid (sodium-ammonium salt) with the help of magnifying glass, Pasteur noticed that crystals are dissymmetric but have the same configuration. A closer look at the sodium ammonium salts of racemic acid revealed that they are dissymmetric but still possess different configurations. One part has chirality (or arrangement) as the salt of (+) tartaric acid, and the other - the opposite.

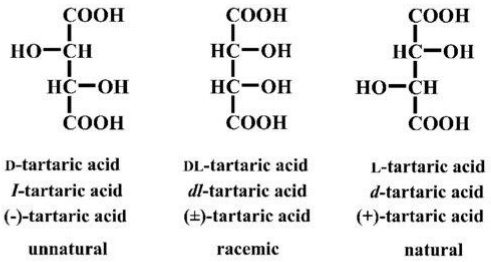

Figure 2.2 Structure of different types of tartaric acids. Adapted from (Sakurai, 2005)

Using tweezers and a magnifying glass, Pasteur separated two types of crystals of racemic acid salt. Then he dissolved them separately in water and found that solutions are optically active, with one rotating the plane of polarization to the right, like a solution of a salt of tartaric acid, and the other at the same angle to the left. Thus, Pasteur mechanically carried out what is currently called the separation of the original mixtures of racemic modification. Pasteur correctly attributed optical activity of (+) tartaric acid dissymmetry of the molecules themselves and not crystals (since the latter disappears upon dissolution). He found that unnatural (-) tartaric acid is specular, where (+) tartaric acid indicates a mixture of equal amounts of (+) and (-) acids and nine inactive acids because of mutual compensation.

The notion that optical activity is caused by asymmetry (chirality) of molecules was developed in 1874 in the works of Le Bel in France and Van't Hoffa in Holland. By this time, it was already known that carbon is tetravalent; it forms bonds with four atoms or groups (Kekule, 1858). Van't Hoff (Nobel laureate Prize 1901) suggested that these four atoms or groups are located around the central carbon atom at the tetrahedron's vertices. Apart from carbon, chiral centers can direct the formation of silicon, tin, tetravalent nitrogen, and phosphorus atoms in quaternary ammonium salts and oxides of tertiary amines and phosphines. As well as an asymmetric carbon atom, the central atom of these compounds has a tetrahedral configuration.

Enantiomers (or optical antipodes) are stereoisomers that refer to the image of one object and the image of the other (Ariëns, 1984). Well-known items related by such enantiomeric relationships are right and left gloves, screws (and nuts) with right and left threads. Enantiomeric objects interact in the same way as symmetrical objects. So, right and left gloves fit equally into a rectangular box; screws with right and left threads are similarly easy to screw into a wooden board. In addition, the configuration of a chiral object cannot be established if it is in an entirely symmetric environment. Still, it can be found that it is opposite to its enantiomer's composition or shows its relationship with the configuration of another chiral object. For example, the chirality of the right glove can be defined as analogous to the chirality of the right hand and opposite to the chirality of the left hand. All of the above holds for chiral molecules as well.

The internal relationship of atoms and groups in molecules is the same in enantiomers (the distance between the thumb and forefinger is the same for the right and left gloves). As a result, enantiomers behave similarly to achiral chemicals or when measuring scalar quantities. Both share the same scalar physical properties (melting point, pressure vapor, boiling point, refractive index, density, ultraviolet and infrared spectra, nuclear magnetic resonance spectrum, mass spectrum, dipole moment, acidity, etc.). However, enantiomers react with chiral reagents at different rates (the ratio of the left and right gloves to the right hand is different) and behave differently when measuring non-scalar physical quantities, such as optical rotation or dispersion of optical rotation. A significant difference in the behavior of enantiomers to chiral reagents is seen in the example of biochemical reactions between chiral substrates and enzymes. Usually, the reactivity of the two enantiomers concerning the enzyme is so different that only one of the two enantiomers will react. Differences in taste, smell, and pharmacological properties of enantiomers are explained by their unequal interaction with chiral enzymatic systems in the human body (Moore et al., 2021).

Racemates. Separation of enantiomers

Racemate (schematically shown in Figure 2.2) is a set of equal amounts of dextrorotatory (+) and levorotatory (-) enantiomeric molecules of the same substance. Obviously, racemates exist only at the macroscopic and not at the molecular level; individual molecules, if chiral, are either right or levorotatory, but not in both directions simultaneously. Depending on the nature of the phases, racemates can be racemic mixtures, racemic compounds, or racemic solid solutions (Figure 2.5). The conversion of a racemate into a pure enantiomer or into a mixture in which one enantiomer is present in excess is called deracemization and is of most significant interest within this work. Deracemization is an ideal but challenging strategy for converting a racemic mixture into a single enantiomer. Currently, racemates are resolved using chemical methods. Through chemical reactions, the enantiomers are converted into diastereomers. Due to their different physical and chemical properties, these diastereomers can be separated by standard separation techniques.

In the chemical industry, two main generic approaches are used for obtaining enantiopure compounds:

a) asymmetric synthesis;
b) enantiomer separation (chiral resolution).

A very detailed review of existing ways to obtain pure enantiomers is given in the works (Lorenz and Seidel-Morgenstern, 2014; Ager, 2005). Figure 2.3 is given to summarize described approaches.

In the last decade, significant progress has been made in asymmetric synthesis by applying fermentation, asymmetric catalysis, or chiral building block techniques. Although achieved success, these techniques can be cost-intensive and challenging to scale up (Ager, 2005; Xiouras, 2019). Desire to ensure a high efficiency explains the increased interest in both the pharmaceutical and chemical industries in developing a low-cost, reliable, and widely applicable approach to separation enantiomers. An alternative to asymmetric synthesis is the synthesis of enantiopure solid material from the racemic mixture using various methods, among which chromatography and selective crystallization are the most established. Detailed descriptions of process concepts can be found in (Ahuja, 1998; West, 2011; Lim et al., 2010).

In this work, the main focus is on the racemic approach and the use of crystallization-based methods.

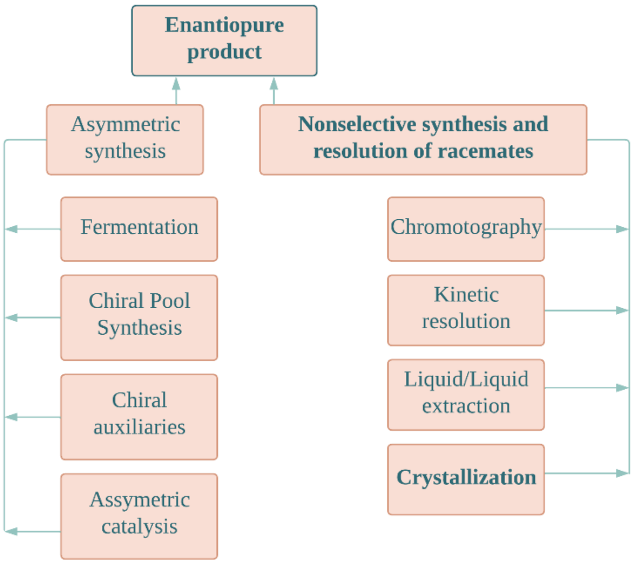

Figure 2.3 Schematic representation of various pathways leading to enantiopure solid products (the pathway studied in this work is given in bold); adapted from (Lorenz and Seidel-Morgenstern, 2014)

Achieved over last decades success in understanding the thermodynamic and kinetic fundamentals makes crystallization widely applicable and cost-efficient manufacturing methods in the chemical and pharmaceutical industries (Murakami, 2007). Compared to other chiral resolution methods, crystallization has significant advantages, such as a theoretical 100% yield and 100% enantiomeric purity. As a result of the simplicity and robustness of these methods, they have attracted a lot of research and have been successfully used to resolve racemates. However, some limitations must be addressed, including limited applicability (5 % - 10% of chiral organic molecules), scalability, and processing times, resulting in low productivity (Xiouras, 2019). This work attempts to avoid low productivity through the design of a continuous crystallization process. In the next Section, the basic concepts of crystallization are summarized, and a detailed description of the applied approaches for increasing productivity is given.

2.2 Crystallization as a technique for enantioseparation

Pasteur's experiment, which was already described earlier in this Chapter, aroused the broad interest of researchers in the application of crystallization for the separation of enantiomers. Crystallization is the basic process of the transition of liquids or gases into a solid form. Looking around, we can consider that such a complicated process accompanied humanity throughout its existence. The formation of minerals, tooth enamel, the skeleton of living organisms, and the construction of snowflakes are all examples of crystallization processes observed daily. This fundamental principle of state change has been scaled up and applied in metallurgy, pharmaceuticals, and other high-tech industries within industry development. In addition, crystallization is an integral part of many technological processes. The physicochemical characteristics of polymers, plastics, and other organic synthesis products are closely related to the crystallization process (Geller et al., 1996). Chemical technology is closely related to the operations of nucleation and growth of crystals. They are crucial for such stages as phase separation, methods of cleaning products, and the formation of a compound's physicochemical characteristics. All of the above gives the right to assert that the role of crystallization is significant and multifaceted and is not limited only to the problems of racemate resolution.

During crystallization, two main stages are distinguished: the formation of crystal nuclei and crystal growth. If the rate of the first stage is higher than the rate of the second, then a finely dispersed solid phase and a large number of crystals are formed. If the growth rate of crystals is ahead of nuclei formation, then a small number of larger crystals are created. Supersaturation or overcooling is the driving force behind the crystallization process. Supersaturated solutions are solutions whose concentration exceeds the equilibrium concentration. To characterize the degree of supersaturation, the following notation is given:

$$S = \frac{c}{c^*},$$

[2.1]

where c = concentration of the liquid phase;
c^* = saturation concentration;
S = Supersaturation.

The overcooling Temperature usually estimates the corresponding degree of overcooling

$$\Delta T = T_{sat} - T_{cryst}$$

[2.2]

The crystallization rate in the system is determined by the rates of nucleation and growth of individual crystals. Naturally, everything that affects the growth rate is reflected in the kinetics of the crystallization process as a whole.

2.2.1 Thermodynamic aspects of crystallization

The application of crystallization techniques for the enantioseparation problem requires a comprehensive knowledge of the fundamental solid-liquid equilibria (SLE), which form the thermodynamic basis of all crystallization processes (Lorenz and Seidel-Morgenstern, 2014).

Solubility equilibria

Solubility depends on the nature of the solute, solvent, and pressure or temperature conditions. For most substances, solubility increases with increasing temperature. For saturated solutions of such substances, supersaturation occurs with a decrease in temperature, and up to a specific concentration (limiting concentration of supersaturation), the solution remains unstable. However, this limitation is explained by the existence of the metastability region. The concept of supersaturation and the existence of the so-called metastable zone, introduced at the turn of the last century, help understand the behavior of a crystallizing system (Ostwald, 1897). Ostwald first introduced the terms labile (unstable) and metastable supersaturation, referring to supersaturated solutions in which the spontaneous deposition of the solid phase, in the absence of crystallizing solid material, will or will not occur, respectively. Based on extensive research into the relationship between supersaturation and spontaneous crystallization, Miers (Miers and Isaac, 1907) pointed out a super solubility curve for every solute-solvent system that is almost parallel to the solubility curve shown in Figure 2.4.

The equilibrium-phase diagram (Miers and Isaac, 1907) gives a basic understanding of why the crystallization process occurs and which type of operation might be the most efficient for producing a specific substance. The borders of the metastability region are defined by the nature of the solute and the solvent and operating regime (Jones, 2002).

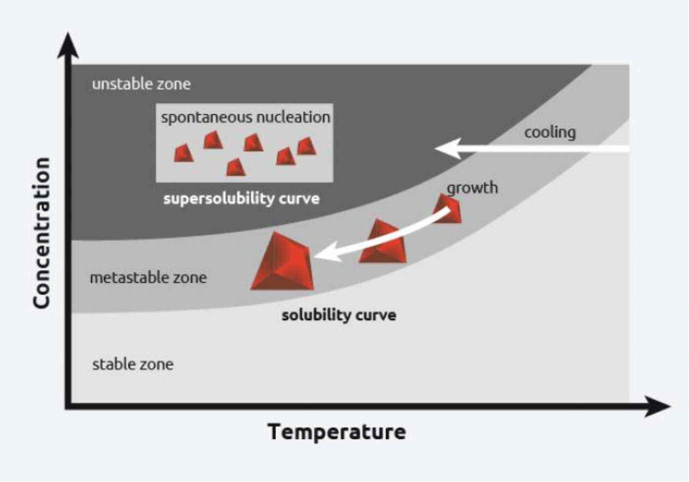

Figure 2.4 Solubility/Supersolubility diagram (adapted from Syrris, 2021)

Presented in Figure 2.4 solubility diagram can be distinguished into three regions:

- Unstable region;
- Metastable zone;
- Stable region.

Crystal growth and nucleation are impossible since all existing particles will be completely dissolved within the stable region. The supersaturated metastable zone is the region where crystals will grow, but nucleation will not occur. Finally, the unstable zone defines as a section where a solution will nucleate spontaneously. The “capacity” of a solvent is typically expressed as the mass of solute that can be dissolved in a given mass of pure solvent at one given temperature. The temperature coefficient of solubility is also an essential factor determining the resulting yield. When the temperature coefficient has a positive value, increasing temperature will increase solute solubility and solution saturation. The solubility of a solute in a chosen solvent defines as the concentration of that solute in its saturated solution. Approaching solution from the oversaturated and undersaturated states, the accuracy of the solubility determination can be proven.

Solid-liquid equilibria diagram

The thermodynamic equilibrium between a liquid and solid phase is graphically represented in phase diagrams. There are two types of relevant phase diagrams for the crystallization technique - the binary melt phase diagram and the ternary solubility phase diagram. A ternary phase diagram of the two enantiomers in a specific solvent will be considered within the framework of this work. The ternary solubility phase diagram shows a three-dimensional representation of the three-component system called ABC. Composition is measured along the sides of the basal triangle, and temperature (or pressure in some cases) is measured along a vertical axis; the temperature is considered constant due to the graphical representation on an equilateral triangular diagram.

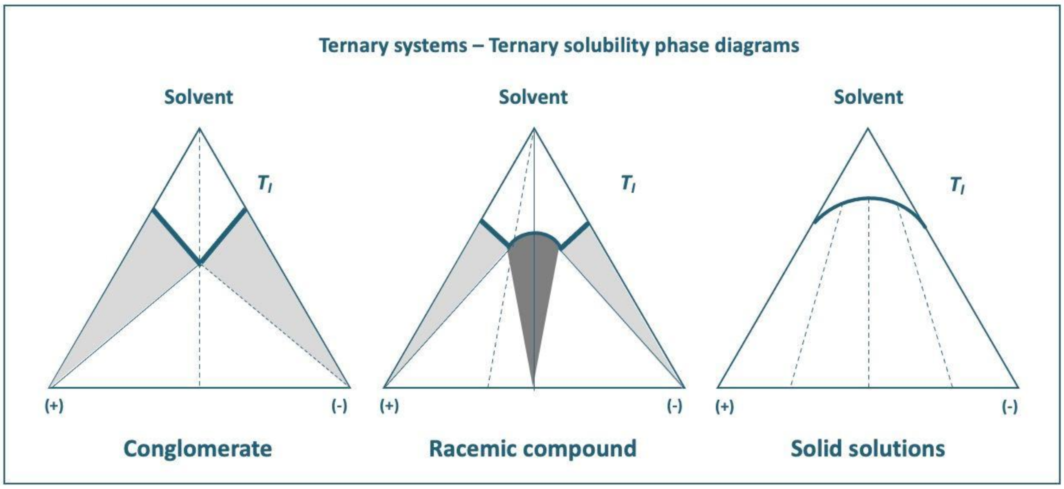

Figure 2.5 Schematic representation of isothermal cuts for a chiral system's ternary solubility phase diagram at a certain temperature T_1; adapted from (Lorenz and Seidel-Morgenstern, 2014).

The isothermal slices represent a system of two enantiomers and solvent in the form of an equilateral prism. Solid green lines represent solubility isotherms for each product type. Different two or three-phase regions may be observed below the solubility isotherms based on the chosen chiral system. A Light grey area shows the regions where enantiomers can be crystallized into a solid phase in an equilibrium state. The dark grey part defines where crystals from the racemic compound and pure conglomerates will be formed. The last diagram in Figure 2.5 illustrates the complete formation of solid solution. In this case, both enantiomers integrate into the crystals. An exemplarily ternary phase diagram is shown in Figure 2.6.

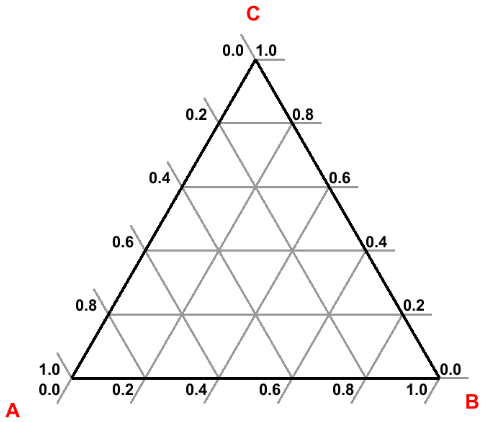

Figure 2.6 Exemplary ternary phase diagram for a system of two enantiomers – A and B, and a solvent – C.

The phase equilibria in ternary systems can be affected by four variables – temperature, pressure, and the concentration of any two of the three components. For the third compound, the following rule is applied:

$$c_A + c_B + c_C = 1 \tag{2.3}$$

Based on [2.3], the mass fraction of the desired compound reads:

$$c_A = \frac{m_A}{m_A + m_B + m_c}$$

where m_A, m_B, m_C – a mass of the corresponding component.

[2.4]

Determination of the solubility isotherms and solubility concentration

The liquid phase of a studied system contains three components: the two types of enantiomers – A and B, as well as a solvent – C; c_A denotes the mass fraction of the A enantiomer; c_B is the mass fraction of the B enantiomer; c_{AB} is the total mass fraction of enantiomers in the liquid phase, calculated by $c_{AB} = c_A + c_B$. Finally, c_C is the mass fraction of the solvent.

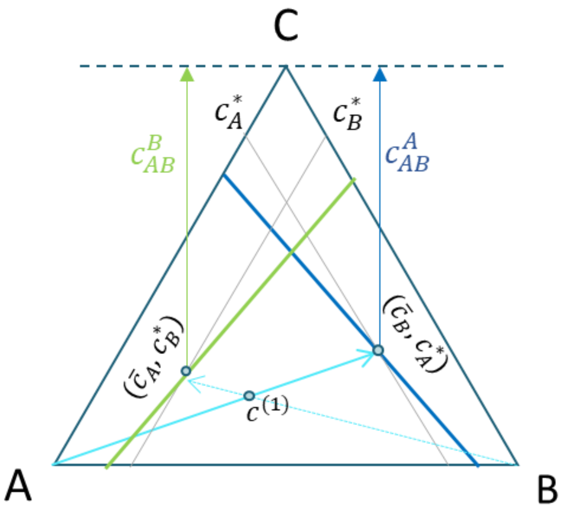

Figure 2.7 Representation of the ternary system with components A crystals, B crystals, and solvent – C; blue line – solubility isotherm c_{AB}^A of A enantiomer; green line – solubility isotherm c_{AB}^B of B enantiomer; solid cyan line – change of liquid phase composition due to the formation of A crystals; dashed cyan line – change of liquid phase composition due to formation of B crystals.

The equations for determining the solubility isotherms of each monohydrate read

$$c_{AB}^A = K_1 + K_2 T + K_3 T^2 + K_4 c_B$$
$$c_{AB}^B = K_1 + K_2 T + K_3 T^2 + K_4 c_A$$

[2.5]

c_{AB}^A is the solubility isotherm of A enantiomer; c_{AB}^B is the solubility isotherm of B enantiomer, $K_1 \dots K_4$ are coefficients defining the solubility areas. Assuming that the liquid phase is initially in a state denoted as $\boldsymbol{c}^{(1)}$ in Figure 2.7, its composition will change due to the formation of solid crystals. If only A-crystals form, the ratio $\frac{\boldsymbol{c_B}}{\boldsymbol{c_{solv}}}$ remains constant, which means that the state change occurs along an auxiliary line through the A corner and $\boldsymbol{c}^{(1)}$ (solid cyan line in Figure 2.7)**.** This line is given by:

$$\frac{c_B}{1 - c_{AB}} = \frac{c_B^1}{1 - c_{AB}^1} = \text{const} = k$$

[2.6]

Crystal growth comes to an end, when c_A falls below the saturation concentration c_A^* on the solubility isotherm, i.e., when the cyan line intersects the blue isotherm in a point $c_A = c_A^*$, $c_B = \bar{c}_B$. Evaluating this condition, one obtains

$$\bar{c}_B = \frac{k \cdot (1 - K_1 - K_2 T - K_3 T^2)}{1 + k \cdot K_4}$$

[2.7]

$$c_A^* = K_1 + K_2 T + K_3 T^2 + \bar{c}_B (K_4 - 1)$$

[2.8]

The value of the supersaturation S_A is the ratio of the distance from the solubility line to the theoretical saturation concentration, written as:

$$S_A = \frac{c_A^1}{c_A^*}$$

[2.9]

The supersaturation for the B-enantiomer can be derived in the same way.

The saturation concentrations expressed as mass fractions of A and B - enantiomers is named c_A^*, can be determined for a given temperature, T (in K), and mass fraction of the solvent, c_C.

When the parameters $K_1 \dots K_4$ are known, the saturation concentration can be calculated from [2.8]. Available data on $K_1 \dots K_4$ for the simulated chiral system is presented in (Petrusevska-Seebach, 2012).

2.2.2 Crystallization kinetics

One of the main questions arising during the investigation of crystallization reaction is the description of the process kinetics, consisting of the following stages: creating supersaturation, nucleation, and crystal growth. The kinetics of crystallization is influenced by temperature, supersaturation of the solution, mixing mechanism, the presence of impurities, the physicochemical properties of the resolution, the design of the apparatus, etc. A detailed description of the phenomena and factors accompanying crystallization kinetics is given in (Mandelkern, 2016; Tavare, 1995; Nývlt, 1985).

Nucleation

Referring to Figure 2.4, the most interesting experimental fact is that in the region of supersaturated solutions, two subregions can be distinguished - metastable and labile. The solution can exist within the metastable region without changes "kinetically" for a very long time, although it is not a thermodynamic equilibrium. Only if seed material is placed in this region, crystal size will increase. In the second, labile, region due to spontaneous fluctuations of temperature, density, pressure, etc., the concentration of the substance also changes locally, and this easily leads to the formation of a new phase. The supersaturation is decreasing, and the concentration of the solution gradually approaches equilibrium due to the precipitation of a new phase. The length of the metastable region depends on the chemical characteristics and structure of the system (Mersmann and Bartosch, 1998). "Formation of a new phase" is a collective and vague term since it simply implies that a new phase is forming. In fact, even by observing the existence of two regions - labile and metastable - it is evident that an initial step - nucleation - needs to be performed for a new phase to grow. In other words, the process of the formation of a new phase can be considered as a two-stage, that is, consisting of forced nucleation stage and spontaneous growth stage.

The most common thermodynamic theory of nucleation by J. Gibbs and M. Volmer (Gibbs, 1873) takes into account the balance of free energy due to a decrease in the energy of the system during the formation of the nucleus and an increase in energy associated with the appearance of the interface (the nucleation surface). The main reason for forming a nucleus is the transition of a substance to a thermodynamically more stable state with stronger bonds in the crystal lattice. Because the change in entropy during the transition from a solution or gas phase to a solid phase is negative, the difference in entropy cannot decrease the system's free energy. Features of different types of nucleation are summarized in Table 2.1.

Table 2.1 Different types of nucleation and their characteristics

Nucleation type	Features
Homogeneous	Gibbs free energy theory: balance between the energy of chemical bonds in the bulk state and the energy of formation of a new surface (Gibbs, 1873).

	Volmer – Frenkel - Weber theory: spontaneous occurrence of hetero-phase fluctuations and their further evolution due to sequential attachment of individual molecules, using a quasi-stationary distribution of nuclei (Frenkel, 1924).
	Ostwald ripening: time evolution of an ensemble of nuclei with different radii - absorption of a small nucleus by large (Schmelzer and Abyzov, 2017).
	Non-stationary conditions: the presence of an induction period
	Crystalline nuclei: the shape is determined by the Gibbs-Curie condition - the minimum surface energy of the nucleus (Li et al., 2016).
Heterogeneous	This type of nucleation occurs if the cooled solution contains fines of another phase or some surface, for example, the walls of the apparatus.
Nucleation in a viscous melt	It is necessary to consider the limited molecular mobility and the exponential dependence of the viscosity of a cooling solution on temperature, the presence of a maximum nucleation rate at a certain temperature (below the temperature of the maximum crystal growth rate).

According to Gibbs&Volmer theory (Gibbs, 1873), the chemical potential of a metastable state exceeds the chemical potential of the corresponding equilibrium phase state. The larger the absolute value of $\Delta\mu$, the less stable the metastable state. However, a viable nucleus does not appear immediately but successively goes through the stages of growth from a cluster of several molecules to a particle. The concept of a metastable state implies that this state corresponds to a local minimum of the thermodynamic potential and, therefore, is stable concerning small changes in the system's parameters.

The Gibbs theory predicts the theoretical possibility of the formation of the nucleus. Still, it cannot explain their formation mechanism, the distribution of nuclei over size and growth rates, etc. From the point of view of achieving practical goals would be crucial information. The first satisfactory theory of the emergence of a new phase was proposed by Volmer and Weber (1926) and then generalized and developed by Frenkel based on statistical mechanics (1939).

Crystal growth

Crystal growth is a spontaneous heterogeneous process that occurs when the interface between the initial and new phases has already been formed in the system at the nucleation stage (Vekilov, 2007). The presence of a driving force is essential, i.e., a deviation from thermodynamic equilibrium, which causes such a redistribution of components between the nutrient medium and the growing crystal, resulting in a growth of its size or a change in its shape. A typical example of growing crystals is their growth from a nutrient medium, which must be a gaseous or liquid phase. Such environment is transferred into a metastable (in fact, labile) state, that is, due to specific influences, it is supersaturated - under certain specified conditions - with one or more components, the excess of which is gradually released in the form of the crystalline phase to the crystallization centers present in the system.

Since the surface of the crystal is constantly exposed to a nutrient medium with unsaturated bonds, the crystal should grow whenever a substance is present in the immediate vicinity that can saturate these bonds (Geller et al., 1996). Supersaturation, which can be expressed both through cooling and through a change in vapor pressure, is defined by the difference in chemical potentials at the interface between the crystalline phase and the metastable nutrient medium. Crystal growth can be described using various theories. At the phenomenological level, three classical types of crystal growth are distinguished:

1. Island growth (Vollmer-Weber, VW) (Nilsen et al., 2007). This mechanism is the complete opposite of layer-by-layer growth. The condition for its implementation is the predominance of the interaction between the nearest atoms over the interaction of these atoms with the substrate.
2. Layer-by-layer growth (Velikov, 2002). Each layer in this growth mechanism appears after the previous layer has grown completely. This growth mechanism is also called Frank-van der Merve (FVM) growth.
3. Layer-plus-island growth (Stranski-Krastanow, SK) (Stranski and Krastanow, 1938). Combined growth mechanism in which the first layer completely covers the surface of the substrate, and three-dimensional islands grow on it. Many factors

can lead to this mechanism, particularly an increase in the degree of supersaturation in the system.

A schematic representation of the growth mechanisms is given in Figure 2.8.

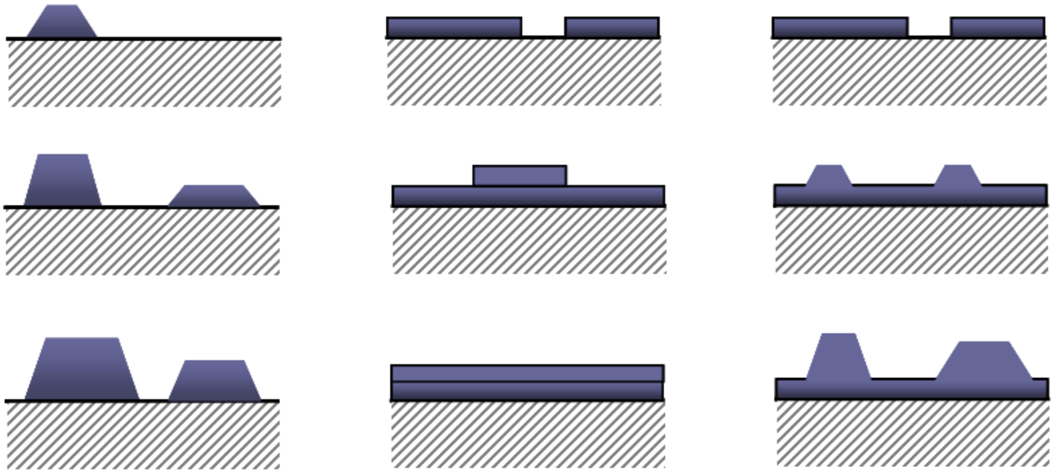

Figure 2.8 Cross-section views of the three primary modes of crystal growth including (left) Volmer–Weber (VW), (middle) Frank–van der Merwe (FVM), and (right) Stranski–Krastanow (SK). Adapted from (Wikipedia [Growth modes], 2008).

The equations describing the growth rate of crystals will be discussed in detail in the next Chapter of this work.

2.2.3 Other methods of obtaining supersaturated solutions

The ways of obtaining supersaturated solutions can be divided into isothermal and polythermal. Schematic representation of existing methods is given in Figure 2.9. Isothermal methods include approaches associated with the removal of the solvent, layering, or chemical interaction.

The simplest example of transferring a solution to a supersaturated state is removing the solvent by evaporation. Evaporative crystallization is carried out by evaporating the solution above its saturation concentration when the temperature is maintained at a constant level. Typically, Evaporative crystallization is applied when processing solutions little dependent on temperature. An example of such a reaction can be a supersaturated solution such as sodium chloride with a low temperature coefficient of solubility (Nizhegorodova et al., 2015).

Whenever another compound is introduced into a system, the solubility of the crystallized substance changes, thus forming a supersaturated solution. An example would be a liquid mixed with a solution that reduces the solubility of the target component. Ethanol introduced into the solution often causes crystallization of the dissolved salt since its solubility in a mixed solution is much lower (Herfurth et al., 2016).

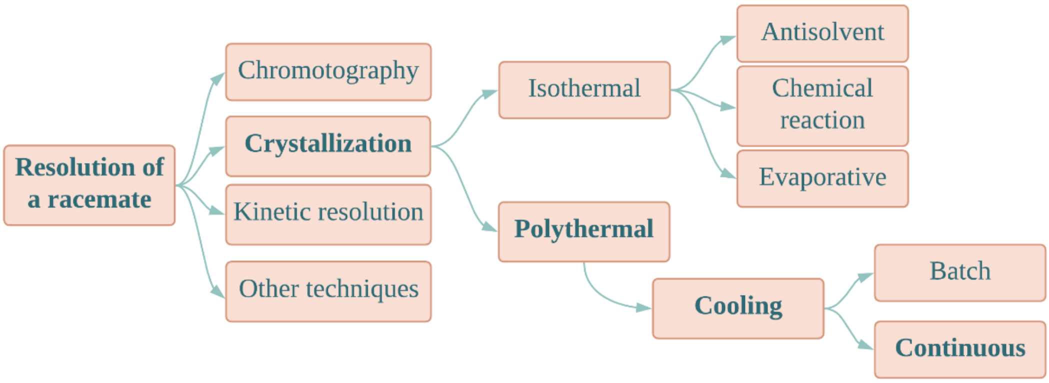

Figure 2.9 Schematic representation of the variability of crystallization techniques

Polythermal methods for obtaining supersaturated solutions are based on the dependence of the solubility of substances on temperature. Cooling the solution gradually leads to the fact that the content of the substance in it becomes higher than the equilibrium one. Supersaturation in this manner is commonly used for compounds with a significant temperature coefficient of solubility. Different approaches to the polythermal methods are close to each other and differ typically in the applied cooling strategy. The rate of creation of supersaturation in both polythermal and isothermal methods is an important parameter that has a significant impact on crystallization.

2.3 Process variants

Various authors classify equipment used to obtain supersaturated solutions differently. Crystallizers can be classified according to the way the process operates: batch and continuous action; by the size of the crystals received: with adjustable and unregulated crystal size; by the method of solution cooling. Referring to Figure 2.9, crystallizers can be classified according to the process of obtaining supersaturation. All crystallizers can be roughly divided into two groups:

- apparatus for polythermal crystallization (using solution cooling);
- device for isothermal crystallization (with solvent removal or antisolvent adding).

It should be noted that there are also combined crystallizers in which supersaturation is created through the use of both methods - cooling and subsequent removal of part of the solvent. However, the fraction of the evaporating solution is very small (about 5-10%), which makes it possible to classify the vacuum crystallizers to the group of polythermal apparatuses.

Continuous and batch crystallization

As shown in Figure 2.9, the crystallization process and required equipment can also be classified according to the operating mode. The batch manufacturing approach has been widely used in the industry since the very beginning, and today it remains a widely applicable technology (Orehek et al., 2012). A good overview of the mechanisms of batch crystallization is given in (Janse, 1974).

Many industries, including chemical, pharmaceutical, and others, use batch crystallization to produce crystals because there are several benefits associated with batch crystallization - maintenance is relatively low, and the equipment is quite simple, the procedure can be applied for different substances since the process parameters can be easily adjusted to the changed conditions (Myerson, 2002).

In both laboratory and industrial applications, batch crystallization offers several advantages. Many industrial batch crystallizers are used to produce crystalline materials with desirable properties and qualities. In contrast, laboratory batch crystallizers are commonly used to characterize crystallization kinetics and CSDs and determine how operating conditions affect these characteristics.

Crystallization in batches is affected by several factors. Among these are periodical cycle time, supersaturation profiles, external seeding, provided CSD control, growth rate dispersions, and mixing mechanism. Difficulties that may arise when operating process in a batch mode are associated with ensuring a constant level of supersaturation, when variation in crystallization temperature along the process may result in reduced product quality, lower productivity, and expanded crystal size distribution. Figure 2.10 (a) shows an example of a batch crystallization system consisting of a stirrer, crystallizer, and product outlet.

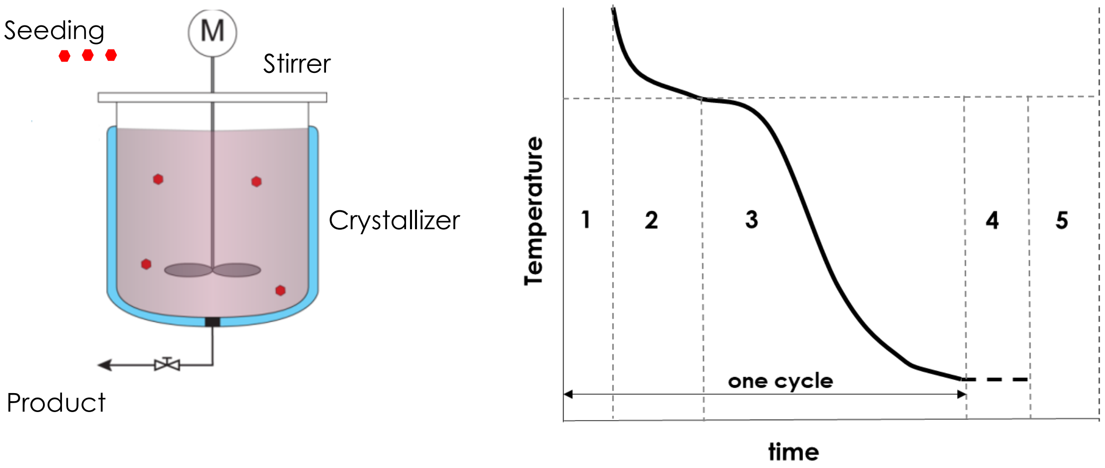

Figure 2.10 (a) Scheme of a batch crystallizer apparatuses, and (b) schematic representation of a batch cycle consisting of 5 sub-steps: filling the crystallizer with a saturated solution [1], cooling solution [2], duration of a periodic cycle [3], removing suspension [4], and cleaning the crystallizer [5].

Several steps are performed during the crystallization process in batch mode. For a cooling crystallizer, the periods of a cycle are shown in Figure 2.10 (b). The one-component system is prepared by filling the crystallizer with a saturated solution [1] and cooling it until nuclei are formed due to supersaturation conditions [2]. The homogeneity of the solution is provided by a stirrer, shown in Figure 2.10 (a). Formation of the desired crystal size distribution is observed while periodic cycle [3]. Following the process, the crystal suspension is fed through the valve to a solid-liquid separation facility where it is separated from the mother liquor [4]. After that, cleaning of the crystallizer [5] is done to prepare for the next operational cycle (Janse, 1974). This simple setup shown in Figure 2.10 (a) and easy adjusting of the process parameters make batch-crystallization processes attractive for the industry (Mersmann, 2001).

Semi-batch crystallizers, also known as fed-batch crystallizers, offer similar features to batch crystallizers. They are constructed to deal with high heat or prevent product contaminations. In continuous crystallization, the semi-batch mode is employed only during dynamic phases, such as the start-up and shutdown of a process. In spite of the broad applicability of the batch processes, the number of studies on continuous crystallization systems has increased rapidly over the last years. Very good overviews of recent progress in continuous crystallization can be found in (Zhang et al., 2017) and (Jiang and Braatz, 2019). In the work of (Orehek et al., 2012), an overview of continuous solution crystallization in the pharmaceutical industry is given, and aspects of transitions from batch crystallization to continuous are discussed.

A continuous crystallization process involves a continuous flow of mother liquid and a continuous withdrawal of the product. In contrast to batch crystallization, continuous processes operate in a steady-state regime, for which many well-proven control strategies are available (Köllges and Vetter, 2018).

The most commonly used continuous systems can be classified as follows:

- the mixed-suspension mixed-product removal (MSMPR) reactor;
- the plug flow reactor (PFR);
- and the continuous oscillatory baffled crystallizer (COBC).

In continuous crystallization, MSMPR crystallizers are the most widely used. Due to their easy operation, they have been applied in a pharmaceutical context in various configurations. Examples of these works can be found in (Wong et al., 2012; Alvarez and Myerson, 2010; Zhang et al., 2012). The advantage of MSMPR crystallizers is the high mixing intensity required for the homogenization of the suspension. Thus, the system behaves as ideally mixed, i.e., in every element of the reactor, the mixing rate is uniform regardless of its location.

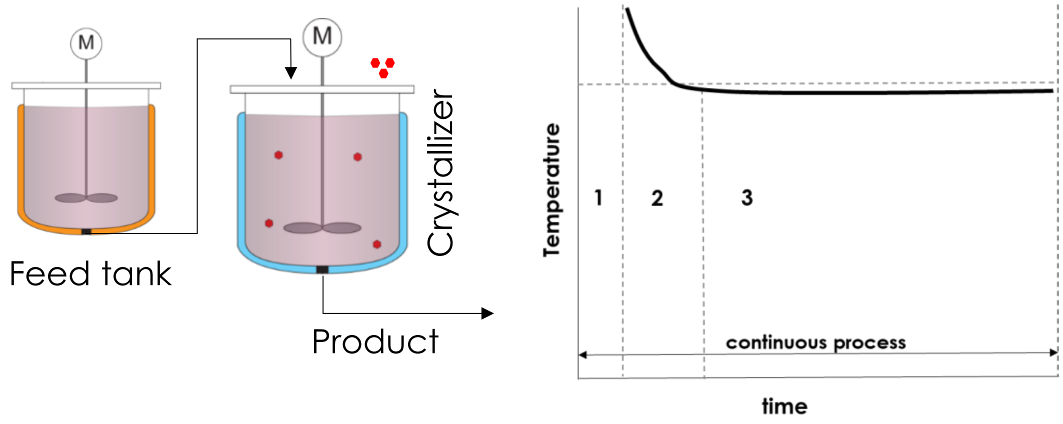

Figure 2.11 (a) Scheme of a continuous crystallization operation, and (b) schematic representation of a continuous system in a steady-state regime.

The system for operating a continuous crystallization using a batch-crystallizer proposed by Binev in (Binev et al., 2016) is shown in Figure 2.11 (a). In the beginning, the feed tank is filled with a saturated solution of the crystallizing material [1]. The crystallizer operates under a cooling temperature profile to ensure desired supersaturation level [2]. In turn, it causes the substance crystals to grow [3], and over time, part of them settle to the bottom of the crystallizer. A "quasi-steady state" can be established by maintaining a constant supersaturation level.

The underlying mechanism that allows preferential crystallization to occur is an existence of a kinetic window for a seeded supersaturated system, where a single enantiomer can be separated from a racemic compound. Regardless of the particular method, the preferential growth of one enantiomeric crystal phase from a solution containing both enantiomers does not represent an equilibrium condition but rather a metastable state. Continuous crystallization technology has the significant advantage of permitting enantiomeric concentrations to be controlled in the solution phase to achieve stereoselective crystallization.

The significant advantage of adapting continuous crystallization technology to achieve stereoselective crystallization lies in managing the relative concentration of the two enantiomers in the solution phase. Since the concentration of both enantiomers is nearly constant during the CPC process, the counter-enantiomer concentration never reaches the critical level for observing spontaneous nucleation (the Ostwald's limit), allowing crystallization of the seeded enantiomer to occur with less control and less explicit requirements for the process parameters.

The review paper (Rougeot and Hein, 2015) introduces the main techniques for continuous preferential crystallization. Several chiral materials have been successfully resolved by the CPC technique. Despite having similar concepts, each process differs depending on the type of apparatus used. Within this work, we discuss three main approaches for Continuous preferential crystallization:

- Single crystallizer, seeded with pure enantiomer, is connected with feed tank to renew the mother liquor.

It is most similar to classical batch crystallization to combine one crystallizer with the feed tank. A supersaturated solution of the racemic mixture is seeded with a pure enantiomer in a single reactor vessel. The mother liquor is continuously replaced with crystal-free supersaturated racemic mixtures, and an overflow regulates excess mother liquor to avoid the nucleation of the counter-enantiomer.

- Setup of two crystallizers, connected by the circulation of a crystal-free liquid.

The concept of the second approach is illustrated in Figure 2.12. The theoretical study of this approach is given in (Elsner et al., 2011) and (Rougeot and Hein, 2015). Examples of modeling crystallization processes using coupled crystallizers are presented in the works of (Qamar et al., 2013).

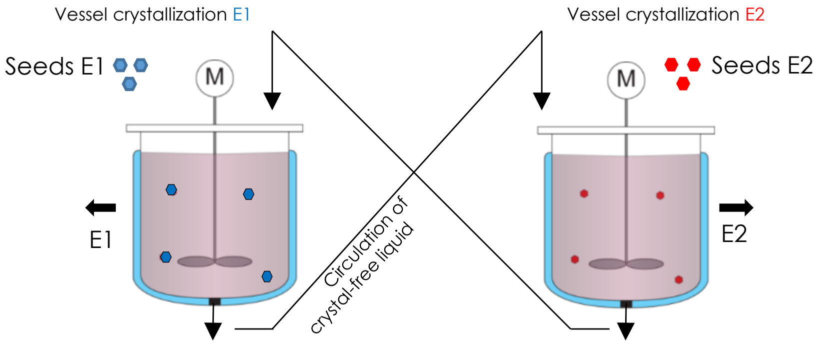

Figure 2.12 Scheme of a continuous crystallization operation using a setup of two crystallizers connected by the crystal-free liquid phase

- Three containers system, where two separate crystallizers (one for each enantiomer) are coupled with a reactor filled with a racemic mixture.

An advanced variation of the continuous preferential crystallization approach involves a three-container system, where two crystallizers are connected in parallel to a single dissolver. It works by simultaneously crystallizing both enantiomers into single crystallizers while the racemic mixture is gradually dissolved in the feed tank. As in other variants, no crystalline liquid phase is continuously circulating.

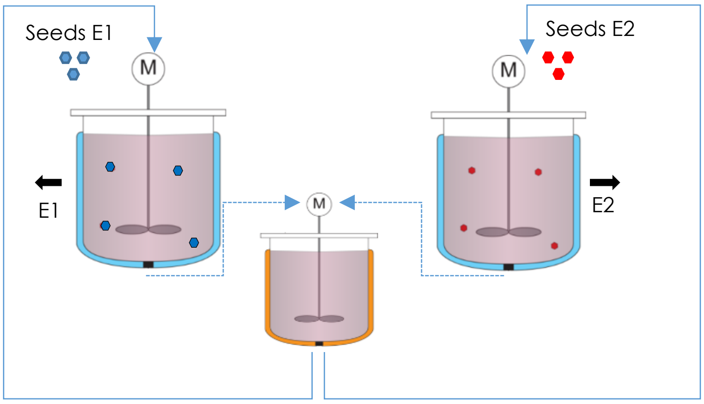

Figure 2.13 Scheme of a continuous crystallization operation using two crystallizers connected by the reactor fed with the racemic mixture

As described at the beginning of this Section, preferential crystallization carried in continuous mode has many advantages over bath process operation. However, understanding the equipment used to ensure continuous crystallization is a significant advantage described in (Rougeot and Hein, 2015) should be mentioned when applying the three-containers system.

This technique allows recovery from a failed resolution when the solid growing phase becomes contaminated by the counter-enantiomer without stopping and restarting the process. One of the main limitations of preferential crystallization is the spontaneous nucleation of the unseeded enantiomer: once the first nucleus appears, the desired enantiomer’s excess will drop off rapidly. When preferential crystallization operates in a single batch mode, contamination of the product means the resolution cycle fails. In the case of the operating process in a continuous regime, crystallizers can be heated to a temperature above the dissolver temperature to ensure dissolution. When the purity of the solid phase returns to an acceptable level, the temperature of the crystallizers can be adjusted to its original value (lower than the dissolver's), and the separation of enantiomers can resume using normal operating conditions.

2.4 Principles of crystallization in fluidized beds

Before moving to the Chapter on modeling the crystallization process, the theoretical aspects of continuous preferential crystallization in a fluidized bed will be discussed within this Section. Examples of good research on developing design rules of continuous preferential crystallization in fluidized beds are given in (Shih et al., 2017; Priambodo et al., 2017). Two scientific works recently investigated a setup for preferential crystallization of enantiomers that contributed greatly to understanding the fluidized bed concept are given in (Temmel et al., 2018; Binev, 2015). Those works showed that both types of crystals could be produced continuously with high purity when coupling two crystallizers and dissolver following the principles of a fluidized bed. Since applying the approach is strongly dependent on the crystallizer geometry, the main aspect of plant setup and behavior of the solid and the liquid phases is discussed in this Section. Using the scientific findings of (Qamar et al., 2013), (Lorenz and Seidel-Morgenstern, 2014), and (Binev, 2015), Figure 2.14 illustrates the basic structure of the continuous fluidized bed production plant.

The main components of the described crystallization system are two identical crystallizers. Due to the parallel connections, a reaction occurs in each crystallizer simultaneously. It is possible to produce two output streams in parallel; each of them contains a single enantiomer. The crystallizers are constantly supplied with a saturated solution of a racemate via a feed tank. The racemic mixture is introduced at the bottom of the crystallizer; the produced crystalline material is withdrawn in the middle of each crystallizer. At the beginning of the process, fixed amounts of enantiopure seed crystals are initially given in each of the two crystallizers. Thus, one crystallizer initially contains the desired enantiomer, while the counter-enantiomer seeds the other. The selective growth of seed crystals reduces the supersaturation of solution in both reservoirs. Solutions consisting of the remaining enantiomer leave the crystallizer at the top and return to the feed tank along the heated lines (dotted lines in Figure 2.14). Meanwhile, particles of a certain size are withdrawn in the form of a suspension from the middle of the crystallizer.

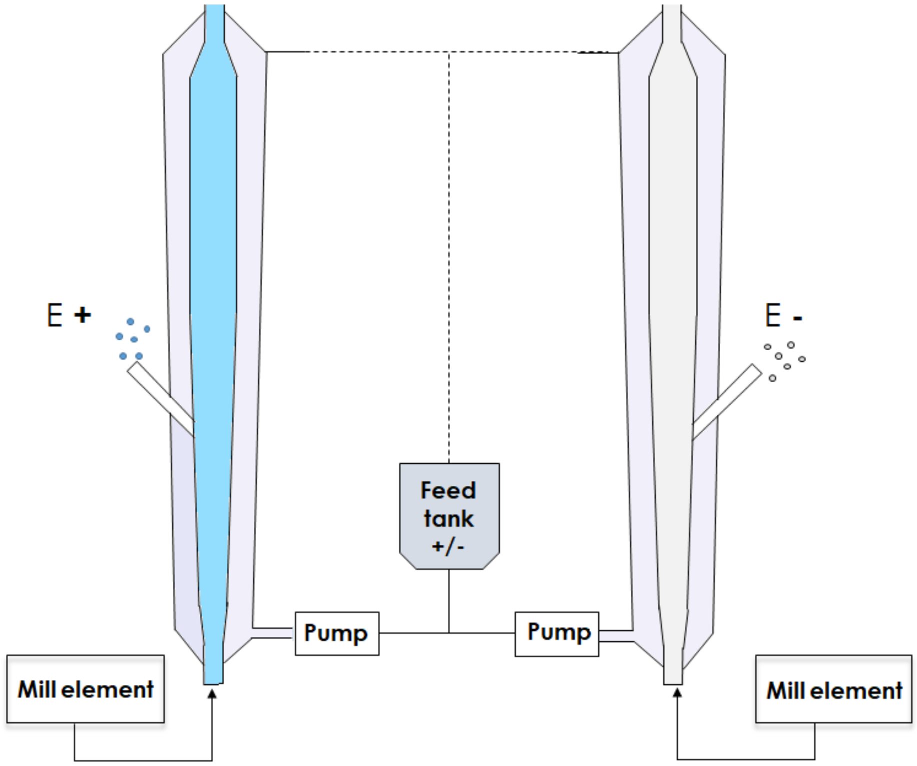

Figure 2.14 Simplified setup of the continuous crystallization process in fluidized beds

To ensure the process is operated continuously, particles smaller than a specific size leave the crystallizer at the upper part. In comparison, the larger particles, which sink to the bottom, are transported to the ultrasonic mill element, where they are crushed into small fines. The particles obtained as a result of crushing are returned to the crystallizer as seeding material. The provided process setup has the advantage of recycling unwanted enantiomers and crystals outside of the desired crystal size distribution (too small or too large particles).

Fluidized bed crystallization is a process of suspending seed crystals in a fluid by circulating a solution through a crystallizer. By keeping the flow rate constant, the crystals will not settle down or flow out of the crystallization vessel, and the supersaturation of the process will remain constant (Myerson, 2002). Fluidization is a physical phenomenon in which a solid material behaves similarly to a liquid (Eslahpazir et al., 2011). Typically, this process occurs when a liquid (liquid or gas) moves upward through the granular material. This fluidization process is based on the equality of the drag force of the upward moving liquid and particles and the gravity force of a single particle. Under such conditions, particles move relative to each other, which is similar to the behavior of single molecules in the liquid. It is important to note that the application of the fluidization concept is closely related to the geometry of the crystallizer since process performance is affected (Midler, 1975; 1976). The general scheme of the fluidized bed crystallizer is shown in Figure 2.15.

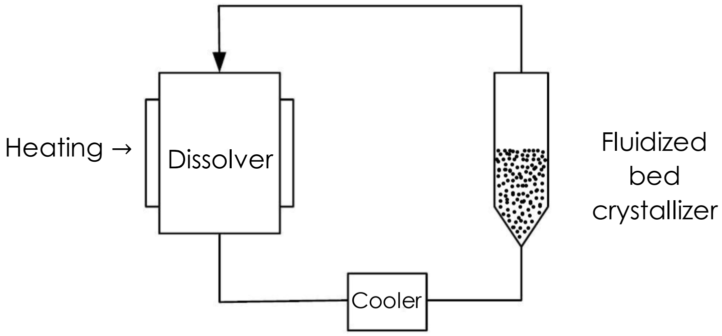

Figure 2.15 General scheme of a fluidized bed crystallization setup (adapted from Tung et al., 2009).

Typically, the fluidized bed crystallizer has a relatively long tapered crystallizer column beneath a cylindrical column. The product withdrawal outlet is placed above the tapered Section. The bottom part of the crystallization setup contains a milling element that fractures large crystals that settle at the bottom against the liquid flow. The resulting crystal breakup produces a relatively small amount of fines. At the bottom of the tapered column, the fluidizing liquid moves at high speeds, and fractured crystals are carried upward, serving as seeds for crystallization, replacing the particles removed as the product. Compared to other methods, crystallization in a fluidized bed has several advantages: a good solid mixing operation provides uniform temperature distribution throughout the reactor, a high mass and heat transfer rate, and easy solid handling.

The equipment used for crystallization in a fluidized bed is shown in Figure 2.16, and it is consists of:

- a double jacketed feed tank, which is the solution reservoir;
- a stirrer;
- double jacketed tubular fluidized bed crystallizers;
- gear pumps;
- peristaltic pumps;
- ultrasonic baths.

The same as described in (Binev, 2015), the connecting pipes between the feed tank and crystallizer are heated, while the rest of the crystallization setup is thermo-isolated. The homogenization of the solution is provided through an electric stirrer with a constant stirring rate. Using a gear pump, the solution is pumped into the bottom of a crystallizer at a constant flow rate. The saturated solution is cooled inside the crystallizer to provide a desired level of supersaturation. Once the solution leaves the top of the crystallizer, it is fed into the feed tank, enriched by dissolving the excess solid feed, and thus becomes saturated again. The working solution can be circulated continuously as long as the feed tank and the FBC are saturated.

When operating a crystallizer in a fluidized bed, the height of the crystal layer is determined by photo sensors. Two photo sensors are installed in the cylindrical portion of the crystallizer for this purpose. The location of the sensors determines the volume of the withdrawn suspension and the decrease in the fluidized bed height.

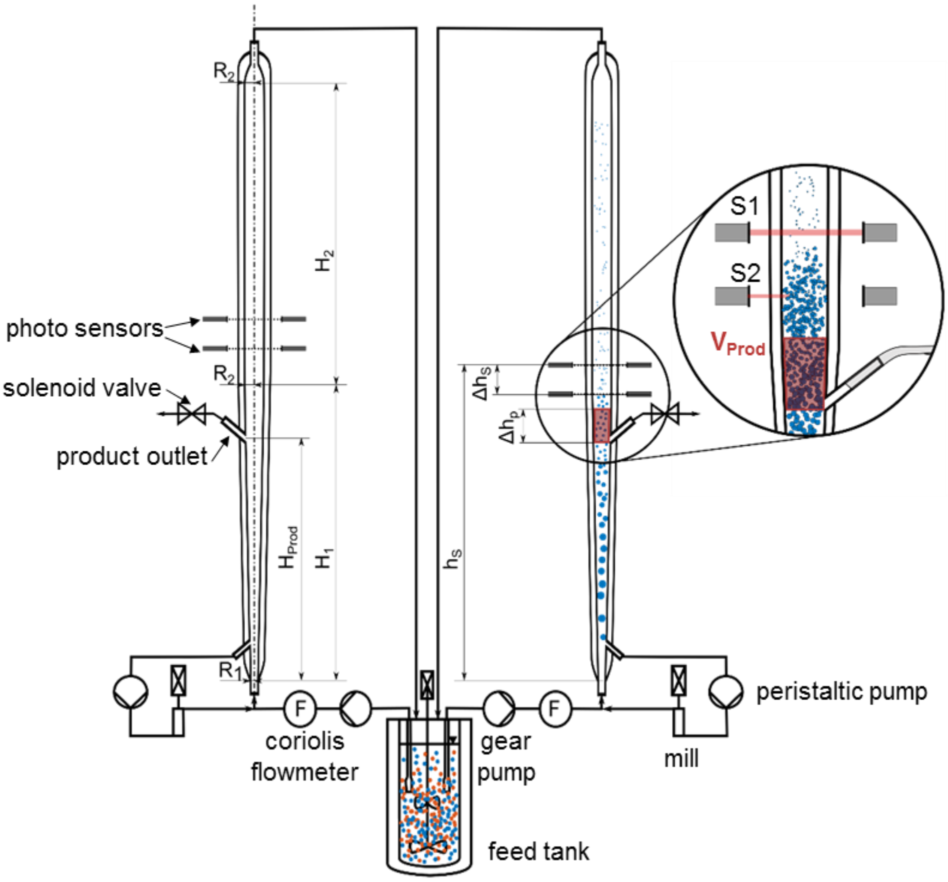

Figure 2.16 Scheme of a setup for performing preferential crystallization in two coupled fluidized bed crystallizers to separate the two enantiomers (desired and counter) of a racemic mixture introduced continuously from a feed tank. Periodic removal is realized at each crystallizer using photo sensors (S_1 and S_2) at the upper part (Binev et al., 2016).

Referring to Figure 2.16, the fluidized bed crystallizer investigated within this work includes:

- a tapered portion, in the form of an inverted frustum of a hollow cone, positioned just below the main cylindrical portion, having an axial length (H_1) and tapering from an internal radius (R_2) at the top, to an internal radius (R_1) at the bottom;
- a main cylindrical portion, in the form of an elongated hollow cylindrical column or tube having an axial length (H_2) a and an internal radius (R_2);
- a product outlet pipe is installed in the conical part of the crystallizer; its location is determined by H_{prod};
- two photosensors (S_1 and S_2) determining the withdrawal segment (Δh_p), and the volume of the withdrawn product (V_{prod}) are placed in the cylindrical Section;
- a height of the layer level is determined by h_s.

When simulating the Reference case, all the parameters of the crystallization setup are described in Chapter 4 of this work.

2.5 Conclusions regarding enantioselective crystallization in fluidized beds

As proven in (Temmel and Lorenz, 2020), applying the fluidized bed concept with the Preferential Crystallization principles provides additional benefits. Intensive mixing under fluidized bed conditions increases the material supply rate by diffusing it to the faces of growing crystals, which accelerates their growth. In this case, the degree of saturation of the solution rapidly decreases. At high solution rates, the rate of nucleation increases, leading to a decrease in the size of crystals. At the same temperature and hydrodynamic conditions, with a reduction in the degree of saturation, the crystal growth rate increases to a greater extent than the nucleation rate. Usually, crystallization of relatively low supersaturated solutions near the lower boundary of the metastable region is carried out in this way by adjusting the temperature and residence time of crystals in the apparatus. Large crystals settle to the bottom, while smaller ones continue to grow in a fluidized layer. Some of the tiny crystals and nuclei are washed out from the crystallizer, which increases the average crystal size, but more importantly, helps to reduce the risks of product contamination. The second advantage of the fluidized bed concept is a product classification that can be achieved by a conical shape of the crystallizer. Under such geometrical conditions, the liquid velocity varies over the crystallizer height, and crystals of a specific size can be withdrawn from the product outlet. Operating the crystallizer under such conditions allows one to predict the mean crystal size and adjust the required size distribution of the withdrawn population.

3. General model development

3.1 Motivation

Over the last decades, the mathematical modeling of crystallization processes has attracted the attention of researchers (Zhao et al., 2007; Hu et al., 2005; Qamar et al., 2013). The pharmaceutical and chemical industries are one driving force in this area (Yu et al., 2007). To meet the high requirements for developing medicines, it is necessary to understand the complex physical and chemical processes underlying production. Phase transitions and heat and mass transfer processes play a crucial role in forming material properties. Typically, it is expensive, time-consuming, and often characterized by long execution times when laboratory experiments are conducted. Consequently, using mathematical modeling methods to study and optimize chemical processes is a vital step towards creating approaches for obtaining materials with the desired properties.

In the pharmaceutical and fine chemical industries, where the product properties are highly dependent on the operating conditions, the importance of a well-controlled crystallization process cannot be overstated. There are several challenges related to the control of crystallization processes discussed in previous chapters. Sometimes, they pertain to the study of macroscopic conditions and characteristics of crystallization; in other cases, they relate to the understanding of phenomena that occur during the formation of crystalline material. Therefore, there are many potential directions for improving the crystallization process by applying appropriate control mechanisms. The operation of an industrial crystallizer, whether batch or continuous, must satisfy the customer's requirements for product purity and crystal size distribution (CSD) and the manufacturer's requirements for economic and trouble-free production (Nagy et al., 2019).

Considering the thermodynamic properties of compounds, the kinetics of the process, and the apparatus characteristics, a model-based environment to simulate preferential crystallization from solution is introduced at the beginning of Chapter 3. The fundamental concepts of modeling the evolution of solids and liquids are discussed before addressing various sub-processes such as growth, particle breakage, and periodic withdrawal of crystals. The developed population balance model for the continuous crystallizer is later supplemented with a mathematical method that can be used to obtain numerical solutions.

3.2 Development of modeling framework

The chosen approach with a model-based framework has been suggested by (Singh et al., 2010); an example of use can be found in (Meisler, 2014). The proposed framework provides the workflow to construct the desired model and solve a developed set of equations for the specific crystallization operation. Various phenomena found in crystallization operations have been modeled applying the set of model assumptions. Similar to (Meisler, 2014), the framework constituents and their dependencies are presented in diagrams. Figure 3.1 represents a scheme of the interactions between the modeled process phenomena; a set of constitutive equations and control and balance equations are considered.

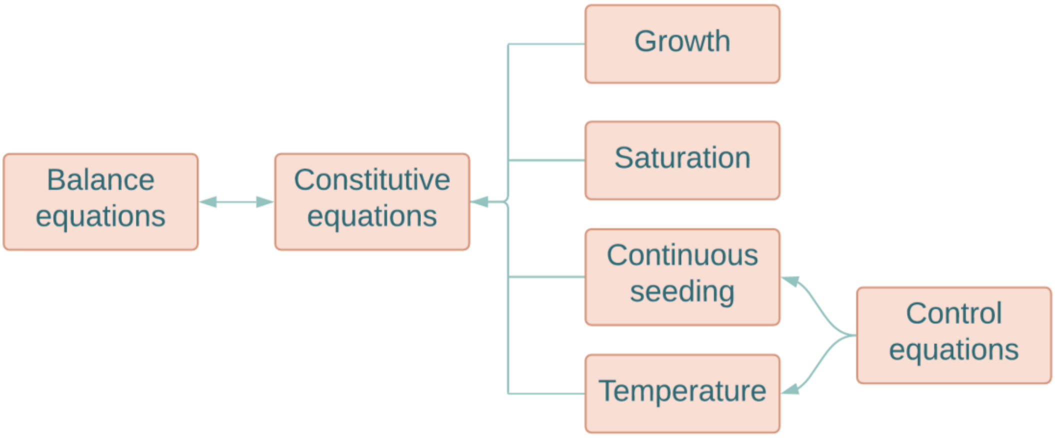

Figure 3.1. Diagram of the relation of the equations to the observed crystallization phenomena. The block of Balance equations involves energy, mass, and population balances relation.

Figure 3.2 demonstrates how the model components interact when the crystallization operation is simulated. At the initial stage, there is a chemical system and a technical approach for solving the posed problem. Selecting a model dimension is based on the need to include in the simulation process crystal shape evolution. Within the framework of this work, a one-dimensional model was developed without considering the change of the crystal shape. The proposed model is based on three main constituents: population balance for the number size density evolution, total mass balance for the liquid phase, and energy balance for the system assuming no temperature difference between the solid phase and the liquid phase. Later in this Chapter, the model components will be discussed in more detail. Mechanisms of crystal growth and nucleation are included as crucial phenomena of crystallization. The list of phenomena may be extended by adding agglomeration and breakage terms; the corresponding sub-model describes each feature. Additionally, two control elements are simulated for the temperature adjustment and for providing a desired particle size distribution.

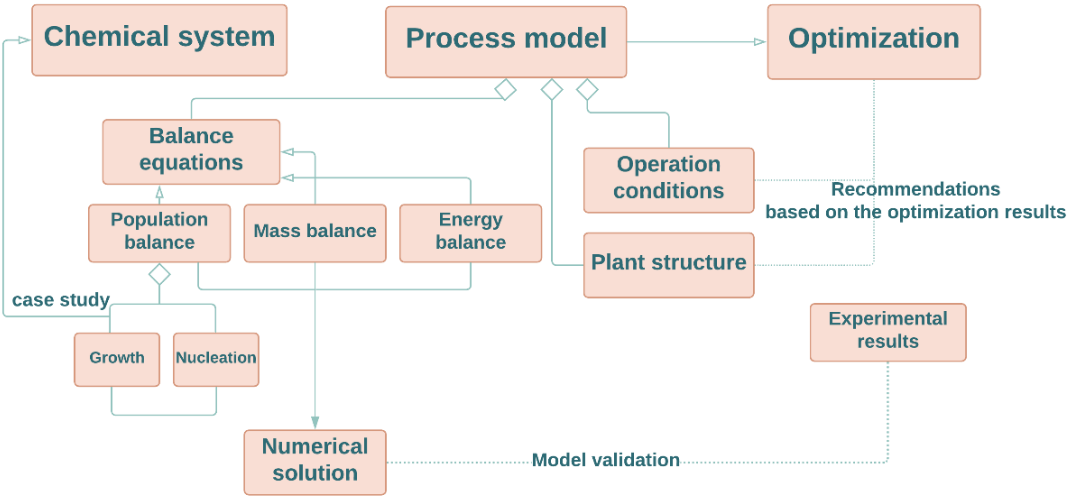

Figure 3.2. Diagram of the model-based framework for the process modeling

The chosen approach allows us to adapt the model depending on the needs. The overall modeling approach demonstrates the scenario for operations and the corresponding data flow with supporting tools within the framework. The general modeling procedure starts with the formulation of the objective. The purpose of this is to simulate a crystallization process and make predictions in terms of process characteristics. Having established the scenario ontology and given the definitions, the crystallization model can be constructed.

3.3 Modeling crystallization process in fluidized beds

The modeling approaches used in chemical engineering are distinguished by the physical substantiation of the phenomena occurring in chemical-technological systems, methodology, and mathematical description. Of the existing methods that most accurately reflect knowledge about the processes of chemical technology and sufficiently fully satisfy the technical requirements is the way of mathematical modeling based on the joint consideration of material balances, equilibrium, and kinetic laws, as well as the features of the heat and mass transfer. The first-principles approach to crystallization modeling is the most widely studied. Examples of such works could be found in (Fujiwara et al., 2005; Jha et al., 2017; Mazzotti et al., 2018).

3.3.1 Model assumptions

Before formulating equations, several assumptions about the process studied in this work must be made. Some of them related to the use of the fluidized bed are described in detail in the previous Chapter. A schematic representation of the preferential crystallization in a fluidized bed is shown in Figure 3.3.

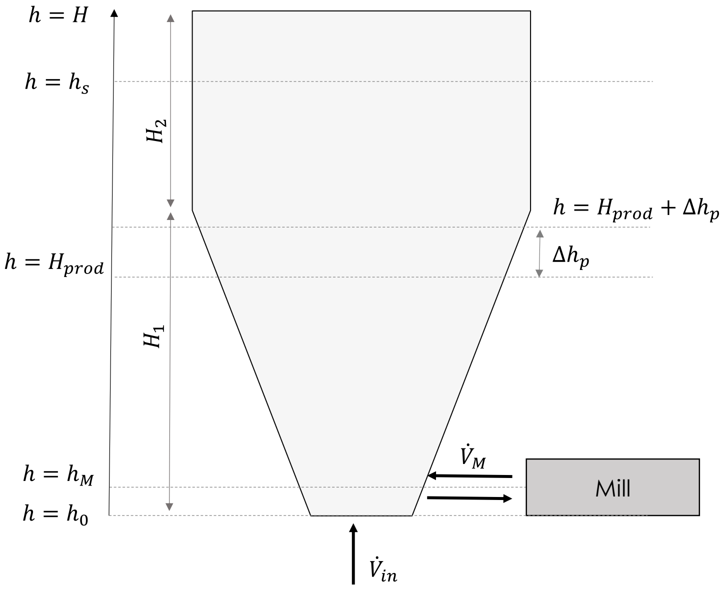

Figure 3.3 Schematic representation of a conical crystallizer for preferential crystallization

The studied crystallizer consists of the cylindrical top and the conical bottom parts. Liquid solvent without crystals enters the crystallizer at the bottom, a mixture of solvent and crystals quits from the crystallizer at the top. The volumetric flow rate ($\dot{V}_{in}$) characterizes the incoming stream; when the removal of crystals is carried out continuously, the outflow rate is determined by $\dot{V}_{prod}$.

Special attention within this work is paid to modeling the crystal's withdrawal in a pulse-wise manner. For this, as described in section 2.4.1, the parameters $H_{prod}, \Delta h_p$, and h_s are used, which define the product outlet position, length of the withdrawal segment, and the sensor position, respectively.

Due to the gravity, buoyancy, and drag forces, small crystals move upwards, while larger crystals sink to the bottom. The developed model describes the process of grinding crystals by an ultrasonic attenuator at the bottom of the crystallizer setup, where $h = h_M$. Additional fluid flow transports crystals to the mill, where they are broken into smaller fragments and sent back to the crystallizer is characterized by $\dot{V}_M$. It should be noted that the reference models for the process under study are described in (Palis et al., 2013; Mangold et al., 2016). Following the above description, the following list of main model assumptions can be formed:

1. The crystallizer having a height (H) consists of a conical lower part (H_1) and a cylindrical upper part (H_2).
2. The position of the product outlet is $h = H_{prod}$. The product is removed in a pulse-wise manner almost instantly. The replacement movement of crystals is provided by taking into account the volume difference.
3. Spatial gradients perpendicular to the external coordinate (h) in the direction of the fluid flow are negligible.
4. The liquid entering the crystallizer at the position $h = h_0$ contains no crystals. The inlet volume flow rate is defined by $\dot{V_{in}}$.
5. Crystal growth and nucleation processes are simulated by using kinetic sub-models.
6. Close to the crystallizer bottom at the connection position ($h = h_M$), particles are withdrawn and sent for grinding to the attenuator.
7. The mill generates particles corresponding to the chosen amount of daughter crystals.
8. The conditions in the crystallizer are non-isothermal. Temperature adjusted using a feedback controller.
9. Plug flow conditions are assumed in the crystallizer. Dispersion terms account for back-mixing.

The presented model distinguishes between the target and the counter-enantiomer, which makes it possible to assess the productivity of the process and the purity of the product. When introducing equations, indices that determine the L- and D- forms are neglected. Only when the quantities of both enantiomers must be considered, a corresponding index i/j is used to identify the modeled component.

3.3.2 Model equations

Population balance modeling of particles evolution

A set of properties can characterize a particle (crystal), and each of those properties can change based on stochastic or deterministic effects during a process. Modeling crystallization processes in a simple way, such as calculating yield using thermodynamics alone, does not provide necessary information about properties associated with crystal size and shape distributions (Mazzotti et al., 2018). Various approaches could be applied to simulate particle evolution, among which are discrete particle methods (Cundall and Strack, 1979), ordinary and stochastic differential equations (Gillespie, 2007). A significant number of simulations of single-particle dynamics use ensemble simulations (Schliemann et al., 2011) and Monte Carlo methods (Zhao et al., 2007). Consequently, a tremendous computational effort is needed as the number of single-particle realizations has to be sufficiently high to guarantee reliable statements on the overall particle ensemble. Alternatively, one can combine particles with the same properties into one class rather than simulating every particle separately. Observed dynamics can be described conveniently in the population balance modeling (PBM) framework. The population balance equation (PBE) proposed by (Hulburt and Katz, 1964) could be combined with the nucleation and crystal growth kinetics to construct the prediction model and predict the crystal size distribution.

The history of population balances began in the 1960s when Hulburt and Katz (1964) introduced this approach in chemical engineering. Later in the 1970s, the concept was formulated in full detail, applying it to the crystallization process by Randolph and Larson (Randolph and Larson, 1988). Ramkrishna (Ramkrishna, 2000) made a significant contribution to understanding the population balance equations and their application in chemical engineering.

To describe the state of a particle in a process following a number of coordinates $\xi_1,\ \xi_1, \ldots$, is presented in a vector form

$$\xi = [\xi_1, \xi_2, \ldots] \tag{3.1}$$

[3.1]

These coordinates are used to determine the position of the particles as well as their size. Other characteristics can be specified – the particle's velocity, the residence time inside the crystallizer, or different relative quantities. It is only important that the chosen coordinate ξ thoroughly enough describes the state of the particle and gives permission to introduce a set of first-order differential equations

$$\frac{d\xi_i}{dt_i} = u_i(\xi, t), \qquad i = 1,2, \ldots$$

[3.2]

Equation [3.2] shows that ξ evolves in time (t). Introduced coordinate vector ξ specify the location of a particle and its quantity; the equations [3.2] are enough to demonstrate the effect of varying in position and time. In this application, the same as in (Mangold et al., 2016), the coordinate set is divided into an external coordinate (h) and an internal coordinate (L). The position of a particle along the crystallizer is described by reactor height (h). The size of the crystals is defined by a characteristic particle length (L) which indicates the diameter of spheres with the same volume as the simulated crystals.

$$\xi = [h, L],$$

with

$$h = [h_1, h_2, \ldots]$$

$$L = [L_1, L_2, \ldots]$$

[3.3]

In a case when the particle is moving passively along the crystallizer, its velocity (v_p) depends on the particle location and its size. The internal coordinate describes the particle evolution along characteristics axes, considering the growth rate dependencies on concentration (c) and temperature (T). Applying these circumstances, equation [3.2] reads

$$\frac{dh}{dt} = v_p(h, L)$$

$$\frac{dL}{dt} = G[c(h,t), T(h,t), L]$$

[3.4]

Since the Introduction of the population balance equations requires an understanding of the fundamental equations [3.4], the evolution of the particle velocity with time will be described later in this Section in terms of the classical model by Richardson and Zaki (Richardson and Zaki, 1954).

The coordinate subsystems (h, L) represent the instantaneous state of a particle. Solving equation [3.2] for every subsystem makes it possible to get a trajectory showing how particles' state evolves in time. By taking all the particles in the system and plotting their states instantly, it is possible to obtain a quantity of points in space, and by solving [3.4], the corresponding quantity of trajectories and velocities. The number of particles in the system at time t may be expressed as $n(\xi, t)$.

In light of the task complexity, it is unrealistic to provide an explicit formula for n in terms of u_i. Instead, the function $\hat{n}(\xi, t)$ is presented to define the net rate of new particles introduced to the system. This function consists of all the means by which particles appear and disappear within a given region.

The elementary consideration of all the particles in the phase space leads to a partial differential equation in the number density function $n(\xi, t)$.

$$\frac{\partial n}{\partial t} + \sum_i \frac{\partial(u_i(\xi,t)n}{\partial \xi_i} = \hat{n}(\xi, t)$$

[3.5]

By separating the phase coordinate ξ into external coordinates (h) and internal coordinates (L), the explicit form of [3.2] reads

$$\frac{\partial n}{\partial t} + \sum_{i=1}^{3} \frac{\partial({v_p}_i(h,t)n)}{\partial h_i} + \sum_j \frac{\partial(G_j[c(h,t), T(h,t), L] \cdot n)}{\partial L_j} = \hat{n}(h, L, t)$$

[3.6]

The function $\hat{n}(h, L, t)$ can, as described earlier, take various forms depending on the application. Within this study, $\hat{n}(h, L, t)$ results from nucleation. Assuming that nuclei have size $L = L_{min}$, $\hat{n}(h, L, t)$ can be described as follows

$$\hat{n}(h,L,t) = \begin{cases} 0, if\ L > L_{min} \\ B_{nuc}, if\ L = L_{min} \end{cases}$$

[3.7]

Then the boundary condition can be introduced in the form

$$G(c) \cdot n(h, L_{min}, t) = B_{nuc}$$

[3.8]

As described in the model assumption, growing crystals sinking to the bottom of the crystallizer are ground in a mill and returned as seeds to the crystallizer. In the general form of the balance equation, the returning crystals are defined as a part of $\hat{n}(h,L,t)$.

$$\hat{n}(h,L,t) = B_{nuc} + n_M(L,t)$$

[3.9]

The general balance equation for the solid phase [3.6] can be rearranged as follows:

$$A(h)\frac{\partial n}{\partial t} = -\frac{\partial}{\partial h}\{A(h) \cdot v_p(h,t) \cdot n(h.L,t)\} - \frac{\partial}{\partial L}\{A(h) \cdot G(c) \cdot n(h.L,t)\} + B_{nuc} + \dot{V}_M \cdot (n_M(L,t) - n(h,L,t)) \cdot \delta(h - h_M)$$

[3.10]

The first term of the right side of the equation [3.10] describes the convective transport of particles with a velocity $v_p(h,L,t)$. The second term defines the crystal growth rate. As for the third term, it refers to the mass exchange with the mill; $\dot{V}_M$ is volume flow rate into and out of the mill, which differs from the inlet flow rate ($\dot{V}_{in}$); h_M denotes the position of the exchange with the mill along the crystallizer axis; $n_M(L,t)$ is the number size density of the particles in the mill independent from particle position. The boundary conditions corresponding to the population balance read

$$v_p(0,L,t) \cdot n(0,L,t) = 0$$

$$\left.\frac{\partial n}{\partial h}\right|_{h,L,t} = 0$$

and initial condition

$$n(h,L,0) = n_0(h,L)$$

[3.11]

To describe the size of crystals, characteristic length (L) is used, representing the size of spheres with the same volume as the crystal. Considering the difference between the assumed spherical particles and actual crystal shapes, a sphericity parameter (φ) can be introduced. This parameter is defined in (Binev, 2015) as the ratio of the surface area of a sphere, which has the same volume as the particle, to the particle's surface area (Wadell, 1935).

$$\varphi = \frac{\sqrt[3]{\pi \cdot \left(6 \cdot V_p\right)^2}}{A_p},$$

[3.12]

where A_p is the particle area, and V_p defines the particle volume.

As mentioned in (Binev, 2015), it is apparent that φ is dimensionless and can have values between 0 and 1, meaning particles with spherical forms will have sphericity parameters closer to 1. In contrast, particles with needlelike shapes will have sphericity parameters closer to 0. In addition, another essential point needs to be mentioned. The assumption made in this work is that the crystals growing from the supersaturated solution do not change their shape but increase in size.

Modeling crystal growth

The proposed mathematical model assumes that primary nucleation (creation of crystallization centers) is negligible, and the growth of crystals occurs on a seeding material. Crystals increase in size while their shape remains unchanged when the racemic mixture is supersaturated. The crystal size at any moment is described by the number size density function $n(h, L, t)$. In this work, the seeding material consisting of spherical crystals is introduced to the system as the initial crystal population characterized by the mass of initial crystalline material (m_{in}), the mean crystal size, (av_{in}) and standard deviation (σ_{in}). The performed simulation set shows that the parameters of initial crystal distribution do not affect the final crystal size. The growth rate (G) for a given supersaturation [1.1], and temperature (T) can be calculated as

$$G = k_g \cdot (S_i\text{-}1)^{n_g} \cdot \exp\left(-\frac{E_g}{R \cdot T}\right),$$

[3.13]

where k_g is a pre-exponential growth factor, n_g is growth exponent, $E_{A,g}$ is the activation energy of the growth rate. Equation [3.14] can be applied when using measured kinetic parameters for a specific chemical system. In view of the presence of appropriate parameters for the nucleation mechanism, the following equation can be proposed

$$B_{nuc} = k_b \cdot (S_i\text{-}1)^{n_b} \cdot \exp\left(-\frac{E_b}{R \cdot T}\right), \tag{3.14}$$

Given the difficulties arising in the simulation of nucleation associated with the measurement of kinetic parameters, an alternative way of the empirical threshold is proposed in Chapter 5 of this work.

Determination of particle velocity

A fluidized bed crystallizer involves two simultaneous processes, fluidization, and crystallization, which produce very complex phenomena requiring comprehensive experimental studies of the process hydrodynamics.

The fluidization behavior depends on its size and relative density of particles to fluid. (Binev et al., 2016). The fluidized bed (solid particles) causes the particles to expand, reducing the pressure drop and increasing the space between them. Each particle moves only within the space between particles at this stage, and solids behave like fluids. The formation of a bubble, fluid space bounded by solid particles, will occur. Upon reaching the top solid border, the bubble will burst and throw particles into a free area, known as a freeboard. Depending on its terminal velocity, the particle thrown on the freeboard can travel along with the fluid flow or fall back into the bed. When the local fluid velocity is smaller than the particle's terminal velocity, the particle will drop. Otherwise, the particles will be transported by the fluid stream.

Determination of terminal velocity depends on force balance consideration. All the forces acting on a single particle in a fluidized bed are shown in Figure 3.4.

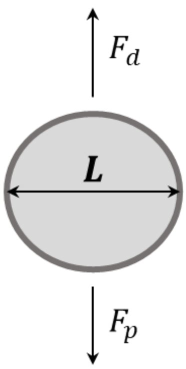

Figure 3.4 Single particle with essential forces acting on it

For a solid bed of particles to be fluidized, where each particle is entirely supported by the liquid, a fluidized particle characterized by its length (L) is affected by the drag force (F_d) and the particle effective weight (F_P). As a steady state, both forces introduced have equal values but characterizes by a different sign. It is assumed that the diameter of the fluidized particle is no longer constant due to the mass transfer of the substance from the up-flowing solution to the crystal surface. An expression for the particle velocity (v_p) follows from the assumption of an equilibrium of forces affecting a single particle:

$$F_d + F_p = 0$$

[3.15]

As it was mentioned before, the particle velocity $v_p(h, L, t)$ is described by the classical model by Richardson and Zaki (Richardson and Zaki, 1954). The applicability of this model to describe the experimentally observed particle behavior with reasonable accuracy is demonstrated in (Binev, 2015) and then in (Mangold et al., 2016).

The equation of particle velocity (v_p) can be represented by the Archimedes number (the ratio between buoyancy force and friction force acting on a particle of length L). This ratio can be calculated as follows

$$Ar(L) = \frac{g \cdot \hat{L}^3 \cdot \rho_f \cdot (\rho_p - \rho_f)}{\mu_f^2}$$

[3.16]

where $\hat{L} = L/\varphi$ is the size of an equivalent spherical particle, φ is calculated from [3.12]. The terminal fluid velocity (v_t), needed to keep a single particle in equilibrium can be obtained from

$$v_t(L) = \frac{Re_t(L) \cdot \mu_f}{\hat{L} \cdot \rho_f}$$

[3.17]

where $Re_t(L)$ is the terminal Reynolds number (Gibilaro, 2001).

$$Re_t(L) = \left(-3.809 + \sqrt{3.809^2 + 1.832 \cdot \sqrt{Ar(L)}}\right)^2$$

[3.18]

For higher particle densities, $v_t(L)$ should be corrected to account for particle-particle interactions applying Richardson Zaki exponent

$$\hat{v}_t(h, L, t) = v_t(L) \cdot \epsilon(h, t)^{n_{RZ}}$$

[3.19]

Corresponding Richardson Zaki exponent (n_{RZ}) is calculated from

$$n_{RZ} = \frac{4.8 + 0.1032 \cdot Ar(L)^{0.57}}{1.0 + 0.043 \cdot Ar(L)^{0.57}}$$

[3.20]

Considering all of the above, particle velocity can be represented as follows

$$v_p(h, L, t) = \frac{\dot{V}}{A(h)} - \hat{v}_t(h, L, t)$$

[3.21]

where $\dot{V}$ is the fluid volume flow, and $A(h)$ is the cross-sectional area.

To define the number of particles contained in particular phase space, the volume of a short crystallizer section of height $(h, \Delta h)$ may be expressed as

$$V_{sec}(h, \Delta h) = \int_{h}^{h+\Delta h} A(\zeta) d\zeta, \text{ where}$$

[3.22]

$V_{sec}(h, \Delta h)$ is the sectional volume, $A(h)$ is the cross-sectional area.

The liquid volume $V_F(h, \Delta h)$ is the difference between the total volume of section $V_{sec}(h, \Delta h)$ and the volume occupied by particles $V_p(h, \Delta h)$:

$$V_F(h, \Delta h) = V_{sec}(h, \Delta h) - V_p(h, \Delta h),$$

[3.23]

The volume occupied by particles can be calculated from:

$$V_p(h, \Delta h) = \int_{h}^{h+\Delta h} A(\zeta) \int_{0}^{\infty} \frac{\pi}{6} \cdot n(h, L, t) \cdot L^3 \cdot dL \cdot d\zeta$$

[3.24]

Particle free cross-sectional area of the crystallizer can be described by:

$$A_F(h,t) = A(h) \cdot (1 - \int_0^\infty \frac{\pi}{6} \cdot n(h,L,t) \cdot L^3 \cdot dL)$$

[3.25]

Considering model assumptions listened above and populations of both enantiomers

$$A_F(h,t) = A(h) \cdot (1 - \int_0^\infty n_i(h,L_i,t) \cdot \frac{\pi}{6} L_i^3 dL_i - \int_0^\infty n_j\big(h,L_j,t\big) \cdot \frac{\pi}{6} L_j^3 dL_j),$$

[3.26]

Where i determines a target compound, and j stays for the counter-enantiomer.

The volume fraction of the fluid $\epsilon(h,t)$ obtained from [3.25] reads

$$\epsilon(h,t) = 1 - \int_0^\infty n_i(h,L_i,t) \cdot \frac{\pi}{6} L_i^3 dL_i - \int_0^\infty n_j(h,L,t) \cdot \frac{\pi}{6} L_j^3 dL_j$$

[3.27]

The main advantage of using **P**opulation **B**alance **E**quations is the relative simplicity of the basic equations and the ability to calculate any process characteristics of interest in practice. Compared with PBE approaches, methods based on integral balances appear to be insufficient since their use does not allow determining the crystal size distribution, which can be crucial in some applications.

Concept of the Mass balance for the liquid phase evolution

In contrast to the evolution of particles, the liquid phase is represented by the mass balance equation. The fundamental law of mass conservation is shown in Figure 3.5.

$$(mass\ at\ time\ \boldsymbol{t} + \Delta\boldsymbol{t}) = (mass\ at\ time\ \boldsymbol{t}) + \begin{cases} +\, mass\ that\ entered\ from\ \boldsymbol{t}\ to\ t + \Delta t \\ -\, mass\ that\ exited\ from\ \boldsymbol{t}\ to\ \boldsymbol{t} + \Delta\boldsymbol{t} \\ +\, mass\ produced \\ by\ chemical\ reaction\ between\ \boldsymbol{t}\ and\ \boldsymbol{t} + \Delta\boldsymbol{t} \end{cases}$$

Figure 3.5 Equation of mass conversation

The mass balances for the enantiomers in the liquid phase of the crystallizer read

$$A(h)\frac{\partial}{\partial t}(\epsilon(h,t)\cdot c(h,t)$$
$$= -\frac{\partial}{\partial h}\left(\dot{V}(h)\cdot c(h,t)\right)+\frac{\rho_{solid}}{\rho_{liquid}}\cdot\int_0^\infty A(h)\cdot G\left.\frac{\partial n}{\partial L}\right|_{h,L,t}\frac{\pi}{6}\cdot L^3\cdot dL$$
$$+\frac{\rho_{solid}}{\rho_{liquid}}\cdot\int_0^\infty A(h)\cdot B_{nuc}\cdot\left.\frac{\partial n}{\partial L}\right|_{h,L,t}\frac{\pi}{6}\cdot L^3\cdot dL$$

[3.28]

where $\epsilon(h,t)$ is the local fluid (void) fraction from [3.27]. The first term in [3.28] considers the changes in the concentration due to convective transfer. The second term evaluates the increases in mass due to particle growth, while the third relates to the mass changing because of nucleation. To quantify the important effect of the inlet flow rate ($\dot{V}_{in}$), we also use the following velocity of the empty tube:

$$u_{empty\ tube}=\frac{\dot{V}_{in}}{A(H_{prod})}$$

[3.29]

Energy balance equation

Modeling of the non-isothermal crystallization behavior is of greatest interest in this Section. A temperature difference in the reactor characterizes the cooling crystallization process. The inlet suspension Temperature (T_{in}) defines the crystallization peak temperature before activating the cooling procedure, the desired crystallization Temperature, measured at the middle of the reactor, T_{cryst} ($h = h_{TP}$), is maintained at the desired level by using a feedback controller. The difference between T_{in} and T_{cryst} inversely related to the general rate of crystallization. Within this study, it is assumed that there is no difference between the temperature of the liquid and the solid phase. The only temperature differences are observed along with the crystallizer height. The energy balance for the system reads

$$\left(A(h)\cdot\epsilon(\rho_{liquid}\cdot c_{p_{liquid}})+A(h)\cdot(1-\epsilon)\cdot\ \rho_{solid}\cdot c_{p_{solid}}\right)\frac{\partial T}{\partial t}=$$
$$-\left(\dot{V}\ \cdot\rho_{liquid}\cdot c_{p_{liquid}}-A(h)\cdot\rho_{solid}\cdot c_{p_{solid}}\right.$$
$$\left.\cdot\left(\int_0^\infty v_{p,i}\cdot n_i\cdot\frac{\pi}{6}\cdot L_i^3\cdot dL_i+\int_0^\infty v_{p,j}\cdot n_j\cdot\frac{\pi}{6}\cdot L_j^3\cdot dL_j\right)\right)\frac{\partial T}{\partial h}$$
$$-\Delta H_{cryst}\cdot\rho_{solid}\cdot\mathrm{A(h)}\cdot\left(\int_0^\infty G\cdot\frac{\partial n_i}{\partial L_i}\cdot\frac{\pi}{6}\cdot L_i^3\cdot dL_i+\int_0^\infty G\cdot\frac{\partial n_j}{\partial L_j}\cdot\frac{\pi}{6}\cdot L_j^3\cdot dL_j\right)$$

$$+ \dot{V}_M \cdot \left((\rho_{liquid} \cdot c_{p_{liquid}}) + \rho_{solid} \cdot c_{p_{solid}} \int_0^\infty n_M \cdot \frac{\pi}{6} \cdot L^3 \cdot dL \right) \cdot (T_M - T) \cdot \delta(h - h_M) + \alpha_{cool} \cdot \pi \cdot d(h) \cdot (T_{cool} - T)$$

[3.30]

The first line of the right-hand side describes temperature changes due to the transport of the liquid and particle in space. The second term of the equation expresses the heat of crystallization due to particle growth. The third term describes the heat exchange between mill and crystallizer, considering the temperature difference between reservoirs. The last term describes heat exchange between crystallizer and a coolant of specified temperature (T_{cool}) using a heat transfer coefficient (α_{cool}). In the simulations, a PI feedback controller was used to provide desired Temperature distribution. An extended version of the temperature equation is presented in Appendix II.

Modeling of processes accompanying crystallization

In addition to the three main components of the crystallization process presented earlier, sub-processes such as particle milling, temperature control, and periodical withdrawal of crystals are also considered within this Chapter.

Application of Milling-Based mechanisms in Continuous crystallization

The experimental study involves breaking the crystals collected at the bottom of the crystallizer into small fragments using a high-speed dispersing instrument. After grinding, the resulting crystals are injected into the reactor as seeding material. The operation of the used disperser is usually described in the following manner. After crystals reach a specific critical size (L_c) the material passes into the mill, containing a rotating impeller. In the mill, particles are reduced by impact attrition. As a simple model of the disperser proposed in (Reynolds, 2010), a standard population balance model is applied. The breakage process can be described using the continuous population balance equation:

$$\left.\frac{\partial n_M}{\partial t}\right|_{L,t} = \int_L^\infty b(L,l) \cdot S_b(l) \cdot n_M(l,t) dl - S_b(L) \cdot n_M(l,t) + \frac{\dot{V}_M}{V_M} \cdot \big(n(L,t) - n_M(L,t)\big),$$

[3.31]

where $n_M(l,t)$ is the number density function, S_b is the selection or breakage rate kernel and $b(L,l)$ is the fragment distribution function (Reynolds, 2010). Selecting a suitable kernel (S_b) and fragment distribution $b(L,l)$ is challenging in this approach. In the same manner, as in (Mangold et al., 2016), the Hill Ng breakage distribution function is used for $b(L,l)$:

$$b(L,l) = K \cdot \frac{1}{l} \cdot \left(\frac{L}{l}\right)^{3(q-1)} \cdot \left(1 - \left(\frac{L}{l}\right)^{3}\right)^{r-1}, r = q \cdot (p-1)$$

[3.32]

Following a breakage event, p identifies the number of daughter fragments, q is a sharpness parameter (Diemer et al., 2005), and K is used as a scaling constant. To simplify the model, it is assumed that once a particle is small enough to pass through the screen, it will leave the mill without further breakage. This classification behavior can be described by a Heaviside function combined with a size-dependent selection rate kernel:

$$S_b(L) = S_0 \cdot H \cdot (L - L_c) = \begin{cases} 0, & if\ L < L_c \\ S_0, & if\ L > L_c \end{cases}$$

[3.33]

As described later in section 4.4, the mechanistic model used to describe the crystal grinding procedure can be used as a control element to determine the final population size.

Periodical crystal withdrawal

When modeling the process, the challenging aspect was finding a simple but precise description for taking a fluid segment periodically out of the crystallizer and simulating this process. In laboratory experiments, the moment of crystal extraction is characterized by the crystal bed height (h_s). After the crystal bed top passes, the light beam initiated by the photosensor S_1, the outlet tube opens, and the suspension containing the crystalline mass is removed from the reactor. Withdrawal is carried out until the level drops to the second light beam initiated by the photosensor S_2.

At first, the triggering of the upper photosensor has to be modeled. It is assumed that the product withdrawal initiated by the volume fraction of the liquid phase [3.27] at the sensor position (h_s) falling below a specified value ($\in_{desired}$). As a consequence, the condition for the withdrawal of crystals reads.

$$\epsilon(h_s) < \epsilon_{desired}$$

[3.34]

The next step is the description of the withdrawal suspension segment. To describe the implementation approach, a simplified diagram of a crystallization setup related to Figure 2.16 is shown in Figure 3.6.

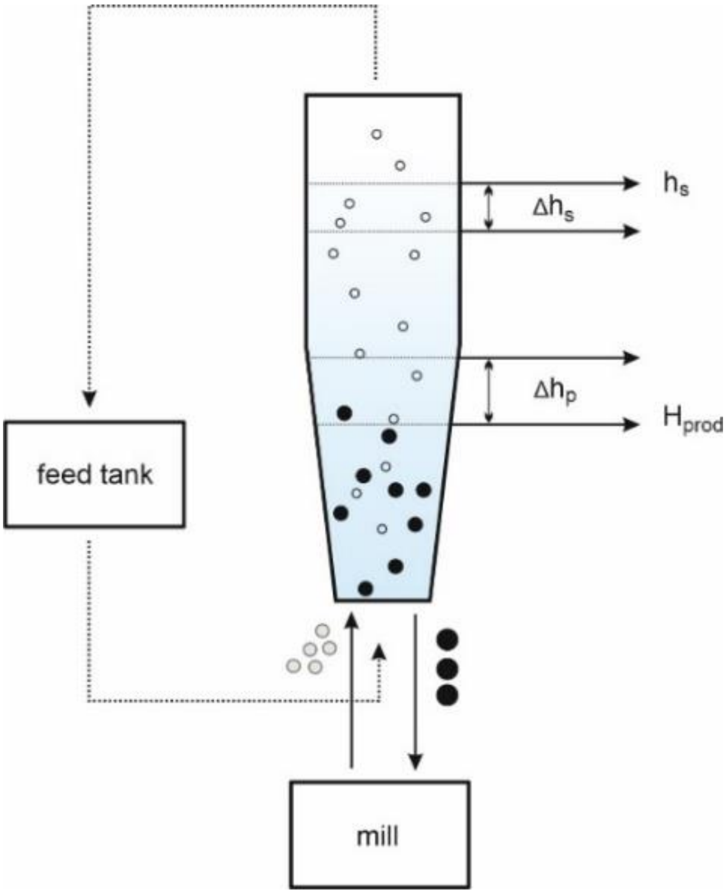

Figure 3.6 Scheme of a single fluidized bed crystallizer for continuous preferential enantioselective crystallization

Modeled as an instantaneous process, this means that product suspension from the height segment (Δh_p) above the outlet position (H_{prod}) is harvested within the one time step. The removed suspension volume is equal to the volume in the cylindrical part, between two sensor positions $V(\Delta h_p) = V(\Delta h_s)$. Due to product collection, the suspension above $H_{prod} + \Delta h_p$ moves downwards over the length Δh_p considering the difference in cross-sectional area $A(h)$. During the final modeling stage, the upper part of the crystallizer, which is "empty" after product removal, has to be replenished. It involves filling up the top segment of the crystallizer with pure liquid containing the racemic inlet composition. The simulation results of this process are given in Chapter 4 of this work.

3.4 Numerical Solution

Discretization of model equations

In chemical engineering, a significant part of process models derived from first principles leads to partial differential equations for distributed parameter systems (Köhler et al., 2001). Because it is often impossible to solve partial differential equations analytically, numerical methods must approximate the solution. Due to limitations of computer resources (especially memory), a finite-dimensional approximation of the infinite-dimensional system (the partial differential equation) is needed. Most modern approximation methods either use integral values (e.g., moments) of the number density function or use discrete values to approximate the number density function itself (Bück, 2012).

To approximate the number density function directly, several methods are available, including finite-difference methods (FDM) (Stynes, 2007), finite-volume methods (FVM) (Eymard et al., 2000), and finite element methods (FEM) (Jagota et al., 2013). These methods approximate the density function at discrete points (grid nodes) within the domain by discretizing the problem domain. After that, dynamic equations are derived for estimating the approximate values at the grid points. Hence, interpolation is used to obtain a solution between two nodes.

The model developed within this work is no exception; introduced equations represent a system of PDEs. For obtaining numerical solutions, the model equations system is reduced to a set of ODEs in the same manner as in (Mangold et al., 2016), using the method of lines (MOL). Discretization is performed by presenting a computational grid consisting of 110 equidistant points in the direction of the spatial coordinate and 100 equidistant points in the direction of the internal coordinate. The main idea of the method of lines is to reduce the problem of solving partial differential equations to find solutions to a system of ordinary differential equations. By reducing partial differential equations to a single continuous dimension, the method allows solutions to be computed using methods and software developed for solving ordinary differential equations (ODEs).

Numerical solution

To integrate differential equations in the Matlab computing environment (MathWorks, 2016), the following functions are provided: ode45, ode23, ode113, ode15s, ode23s, etc. (Reichelt and Shampine, 2017). The steady-state solutions for the described in this

Chapter equations are obtained by a time integration with the ODE23 integrator applying Runge–Kutta method. The stopping criterion is met when the relative mass defect, expressed as a ratio between the sum of all mass flows across the system boundary and the mass flow into the system, falls below a threshold of 10^{-5}.

Part 2. Application of process model to describe preferential crystallization performed in fluidized beds

The second part of this work is devoted to the practical application of the developed model, demonstration of its usefulness, and subsequent sensitivity analysis of the model parameters. Considering the available data from laboratory experiments, the model is demonstrated using the example of the chiral compound called asparagine monohydrate. All experimental results demonstrated in this work are obtained in a in a cooperative project by members of the research group of Prof. Andreas Seidel-Morgenstern. Results data provided mainly by M.Sc. Jonathan Gänsch under supervision of Prof. Heike Lorenz. Information about the chosen chiral system and its thermodynamic properties is given at the beginning of this Chapter. Based on the proposed concept of a fluidized bed and a plant setup for conducting experiments, the parameters related to the geometry and operating mode are also discussed in this Chapter. Particular attention is paid to comparing the simulation and experimental results. The trends obtained in the course of simulations are discussed.

The sensitivity analysis presented in this Chapter investigates how the variation in the output of a numerical model can be attributed to variations of its input factors. Within this broad definition, the approach, level of complexity, and purposes of sensitivity analysis vary significantly depending on the modeling domain and the specific application aims. Later, results of the sensitivity analysis are presented to understand the most influential model parameters and validate some of the model assumptions.

4. Model demonstration

4.1 Introduction of the parameter set

According to the scheme of the modeling environment presented in Chapter 3, there are three different modeling parameters related to: 1. the studied chiral system, 2. the crystallization setup, and 3. the operating mode, respectively. In the course of the work, the choice of parameter values is justified, and some of them influence is studied. All parameters characterizing the studied chemical system are given in Chapter 1 of this work.

As a validation step, all calculations were performed using the geometry from (Gänsch et al., 2021), denoted as Reference case in the following. A detailed diagram of the crystallizer setup is shown in Figure 2.16. Parameters related to the Crystallizer geometry are summarized in Table 4.1.

Table 4.1 Parameters related to the Reference geometry

Parameter		L crystallizer	D crystallizer
Crystallizer height	H, $[m]$	1.052	1.054
Height of the conical part	H_1, $[m]$	0.49	0.456
Height of the cylindrical part	H_2, $[m]$	0.562	0.598
Product outlet height	H_{prod}, $[m]$	0.335	0.319
Diameter of the bottom	R_1, $[m]$	0.0126	0.0113
Diameter of the top	R_2, $[m]$	0.0276	0.00261
Volume of the crystallizer	V_{total}, $[l]$	0.511	0.478

For the described reference geometry, the parameters listed in table 4.3 are constant. The theoretical volume of the withdrawn product, and the position of the upper sensor (S_1) determine the applied product withdrawal strategy. This means that the sensor position S_1 in the cylindrical part affects the withdrawal strategy used. The new withdrawn volume, (V_{prod}) which is removed above the outlet position (H_{prod}) is determined by the bed height (Δh_p).

Table 4.2 Parameters of the reference withdrawal strategy

Upper sensor position	$h_S - H_{prod}$	0.155 $[m]$
Withdrawn segment	Δh_p	0.12 $[m]$
Theoretical withdrawal volume	V_{prod}	60 $[ml]$

Operating parameters

It is well known that supersaturation is the driving force of the crystallization process. Selection of the most appropriate of the operating parameters for ensuring the desired supersaturation is a complex task. Product purity, productivity, and CSD are strongly influenced by nucleation and growth processes, which in turn are affected by temperature, the intensity of mixing, inlet liquid concentration, and other conditions under which crystallization is carried out. Operating parameters for the Reference case simulation used in this work have been selected based on the experimental study (Binev, 2015). The list of the operating parameters is given in Table 4.3.

Table 4.3 Operating parameters of the Reference case

Crystallization temperature	T_{cryst}	30 [°C]
Saturation temperature	T_{sat}	35 [°C]
Liquid phase inlet concentration	c_{in}	0.0454 $[kg_{solute} kg_{solution}^{-1}]$
Inlet volume flow rate	$\dot{V}_{in}$	12 $[lh^{-1}]$

The operating temperature in the studied crystallization process typically varies in the 25 to 35 °C range. The direct effect of temperature changes is discussed at the end of this Chapter. The challenging aspect covered in this study is maintaining the temperature in simulations according to laboratory measurements. As described in section 3.3, a feedback controller is used to adjust the temperature at the three temperature sensor positions: T_{in}, T_{cryst}, T_{out} at the bottom, middle, and top of the crystallizer, respectively. The obtained temperature agreement is shown in Figure 4.1.

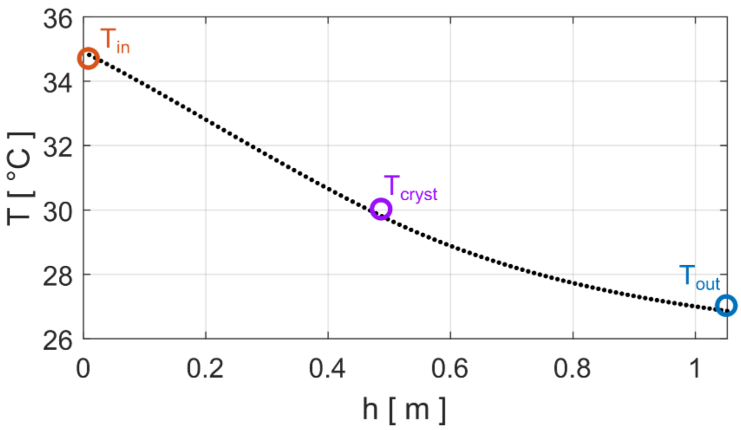

Figure 4.1 Temperature distribution over crystallizer height. The symbols show measured values at the bottom (T_{in}), middle (T_{cryst}) and top (T_{out}) of the crystallizer. The line shows the simulated temperature distribution in the crystallizer.

Temperature adjustment is characterized by using the controller with a heat transfer coefficient α_{cool}= 25 $\frac{W}{m^2K}$, and the corresponding coefficients K_p= 76.44, $K_i = 1.22$.

4.2 Analysis of simulation results

4.2.1 Simulation results of the Reference case

The first set of calculations is performed for the Reference case. The required physical-chemical model parameter values are available from Tables 1.1 and 1.2. In a first attempt, the Reference case is simulated for the two crystallizers – L and D. Detailed information about the crystallizer setup is given in Table 4.1. The slight difference in the crystallizer parameters is also taken into account and demonstrated in Table 4.1. The observed deviations are due to unavoidable minor differences in manufacturing the two glass vessels. Similar to (Gänsch et al., 2021), these two crystallizers are called Cref-D and Cref-L to distinguish the specific enantiomer seeded and produced.

The simulation results, shown in Figure 4.2 demonstrate the Reference case for Cref-L after reaching the periodical steady state. The four snapshots of the particle number size density represent the different stages of one operation cycle after the system reaches a steady state. The upper left diagram (a) shows the crystal distribution immediately before the product withdrawal. One can see that the fluidized bed just reaches up to the sensor (h_S). Above the sensor, the fluid is nearly crystal free. Product withdrawal occurs following the model assumption specified in Chapter 3 of this work. Product is withdrawn when the volume fraction of the liquid at the sensor position falls below the specified value ($\epsilon_{desired}$) which triggers the sensor. The upper right diagram (b) contains the crystal distribution immediately after the product withdrawal. The crystals bed above $H_{Prod} + \Delta h_p$ has dropped at this instant by Δh_p ≈0.012 m. The lower left diagram (c) shows the crystal distribution in the middle of the observed cycle. Gradually, crystals of medium size accumulate again in the vicinity above the product outlet position (Δh_p). Finally, the lower right diagram (d) contains the crystal distribution immediately before the next product withdrawal. The cycle duration (Δt) for this Reference case is equal to 1 hour. Each product withdrawal causes crystals located above the withdrawal point to move instantaneously downward, thus remaining in the crystallizer.

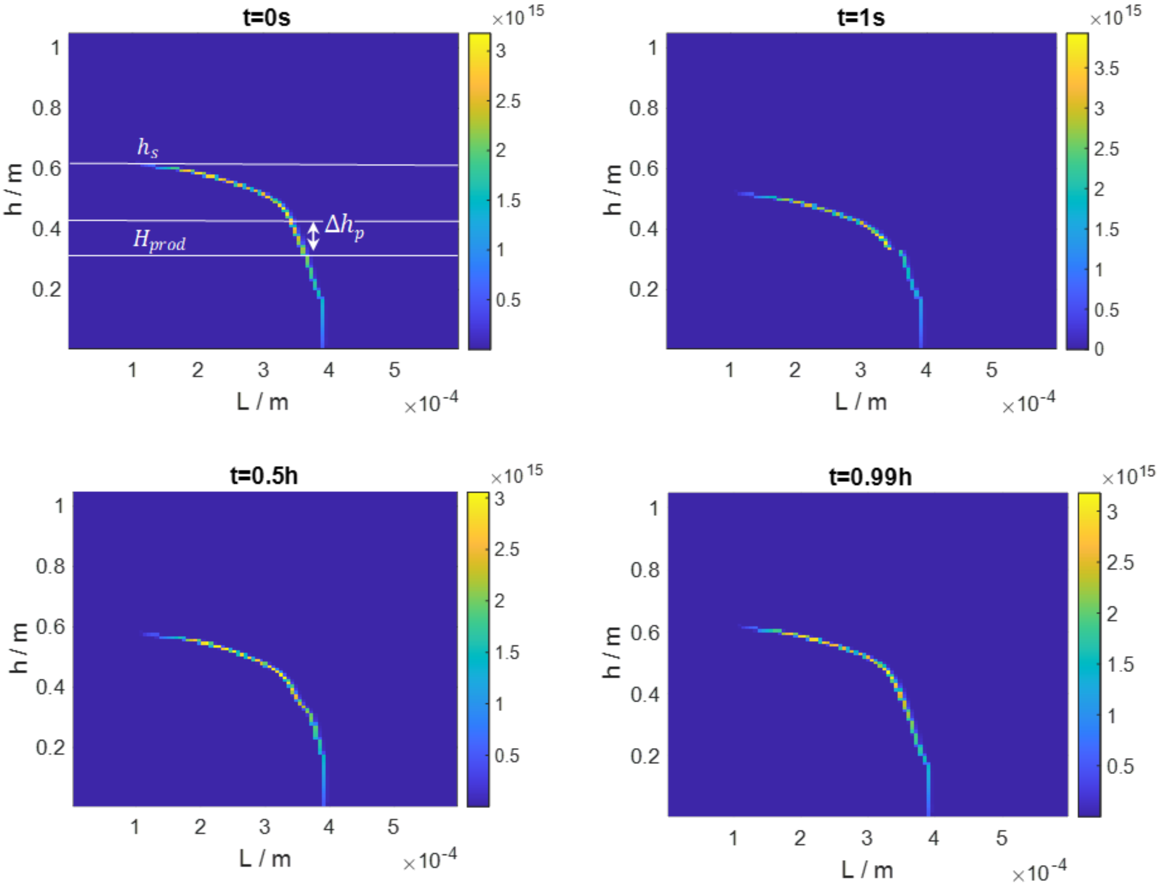

Figure 4.2 Simulated number size densities $n(h, L, t)$ for the parameters corresponding to the Reference case and the crystallizer called Cref-L. The figure shows four snapshots illustrating the location of different sizes of crystals within the crystallizer covering a period of around 1 hour: Immediately before product removal (a), immediately after product removal (b), at an intermediate time point during the cycle (c), and finally at the end of the cycle, right before the next product removal (d). The results of the corresponding simulation for the CRef-D crystallizer are given in the Appendix I.

Combined with the available data, the proposed model can be considered a powerful tool for process study and subsequent control. The following subchapter is devoted to validating the model and comparing the results of the numerical solution with the experimental outcomes.

4.2.2 Extension of the Reference case study

An extended study of the Reference case is directed to assess the influence of the product withdrawal strategy. The withdrawal strategy is defined by two process conditions – the position of the upper photo sensor, which is equal to the maximal height of the fluidized bed, h_s. The second parameter is the distance between the photo sensors in the cylindrical part, and thus, the withdrawn theoretical volume pro operating cycle. Parameters related to the withdrawal strategy of the Reference case are given in Table 4.2. Subsequently, new positions of the two photo sensors were tested, the obtained simulation results were compared with the experimental outcomes. In particular, the height of the upper photo sensor (h_s) was increased to investigate if the height of the fluidized bed will affect the productivity of the process. The parameters defining new withdrawal strategies are listed in Table 4.4.

Table 4.4. Parameters related to the withdrawal strategies

Strategy	1	2	3	4
Sensor position, h_s [m]	0.49	0.6	0.77	0.97
Withdrawn distance, Δh_p [m]	0.125	0.085	0.085	0.085

It should be noted that the parameters related to the crystallizer geometry and operating mode, as well as the properties of the studied chiral system, remained unchanged.

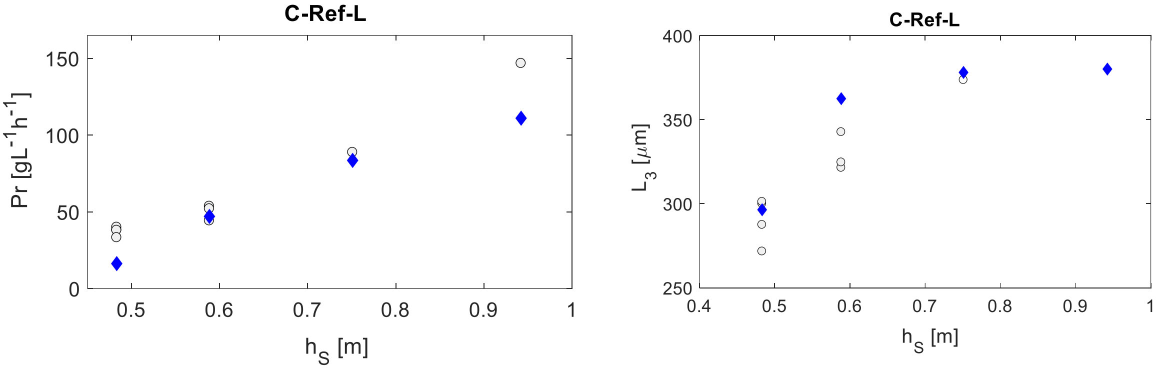

Figure 4.3 Influence of the upper sensor position, h_S, on a) the productivity (Pr); b) mean product crystal size (L_3). Black points demonstrate the observed experimental productivity and mean crystal size for the different withdrawal strategies (see Table 4.4) in different crystallizer runs. Simulated values of the productivity and mean crystal size are marked blue. The height of the withdrawn segment (Δh_p) is equal 0.12 m for the first strategy (when $h_s = 0.49\,m$), and 0.085m for all others applied strategies. Shown simulation results correspond to crystallizer C-ref-L, geometry and operating parameters are given above. The analogous results for the C-ref-D crystallizer are given in the Appendix I.

The simulation results obtained without adjusting the model parameters confirm, on a qualitative and partly quantitative basis, the applicability of the developed model to simulate the studied enantioseparation process.

Model-based study of Crystal Size Distribution

As the product crystal size is essential for many applications, it is worthwhile to look at the crystal size distribution for different sensor positions. Figure 4.4 (left) depicts the simulated product crystal size distributions for four different sensor positions. As can be seen, for higher sensor positions, the product crystal size distribution is favorably sharpened and moves towards larger product crystals, which should be preferable in most applications. The sensor position is, of course, limited by the maximal height of the crystallizer.

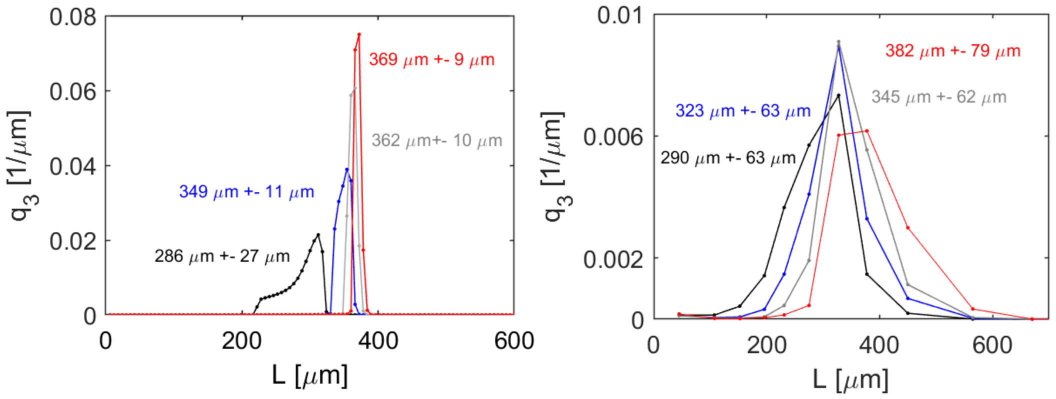

Figure 4.4 Mean steady-state crystal size distributions (q3) with their respective mean values and standard deviations for four different product withdrawal strategies, which mainly differ regarding the position of the upper photo sensor, h_s (black, 0.475; blue, 0.585; grey, 0.755; red, 0.955m). The withdrawal distance (Δh_p) is 0.085 m (except for the first strategy, Δh_p= 0.11 m, black). Given results are for the D crystallizer (Table 4.3). Simulated results corresponding to the process model are given in the left diagram; the right diagram illustrates corresponding experimental results.

Furthermore, it is also of interest to assess the fit of simulated distributions to the laboratory experiments. As shown in 4.4 (right), the product crystal size increases significantly with increasing crystal bed height, from 290 to 382 μm. The residence time of the product crystals increases with the height of the crystal beds. For the first withdrawal strategy (black), almost all crystals above the product outlet are withdrawn. Consequently, the residence time of the product crystals, once they have begun to settle, is approximately one cycle time. This contrasts with the strategy with the highest crystal beds, in which the residence time of the settling product crystals can be five times the cycle time. As a result, the crystals have more time to grow, resulting in larger product crystals.

As predicted by the simulations, the height of the fluidized bed significantly influences the resulting product crystal sizes. Comparing simulated and experimental means, as in the case with the simulation of the L- crystallizer, the agreement is reasonably good. Nevertheless, based on the standard deviation assessment, the model is limited to predicting the width of the crystal size distribution. Crystal size distribution during the crystallization process results from the interaction of simultaneous phenomena, such as nucleation, growth, agglomeration, and attrition. The developed model does not consider the impact of particle agglomeration and attrition, which explains the narrower size distribution compared to experiments. Despite this, the developed model can accurately predict the product's mean particle size during crystallizer runs, verifying its applicability.

4.2.3 Simulation trends

From comparing the obtained results for the introduced four strategies, it can be concluded that the most interesting parameter to study is the one that determines the bed height in the crystallizer, i.e. the position of the upper sensor (h_S). This parameter strongly affects the finally established periodic operation regime. In the course of the simulations, the parameter h_S is changed stepwise. Due to the constant difference between the two sensors in the cylindrical part, the withdrawn volume of the product remained unchanged. The main idea is to predict values for the productivity and mean crystal size of the product, depending on sensor position placement.

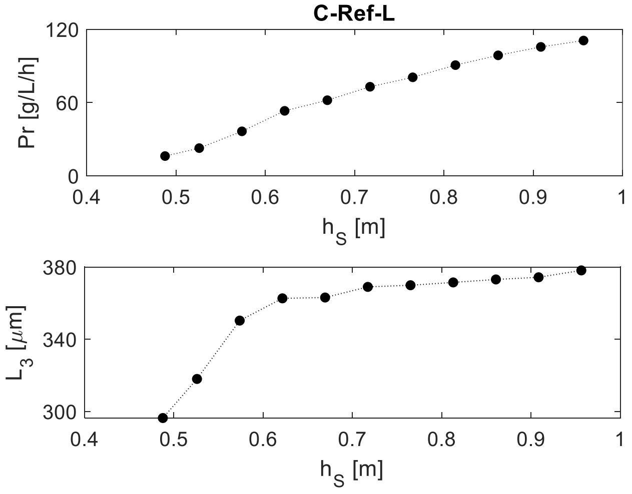

Figure 4.5 Influence of the upper sensor position, h_S, on a) the productivity, *Pr*; b) the mean product crystal size, L_3. Step size is $0.05\ m$ along the height of the cylindrical part.

When moving the sensors to a higher position than in the Reference case, a significant decrease in the time window between two withdrawals is observed. An increase in harvesting frequency results in higher productivity, which is shown in Figure 4.5 (upper diagram). The simulated mean product crystal size is also dependent on the sensor position (Figure 4.5 (bottom diagram)). As can be seen, larger product crystals can be produced from a higher sensor position, but this effect is not as significant as the effect on productivity. The sensor position is limited by the maximal height of the crystallizer and by the risk of potential nucleation, which is discussed later in this work. From the simulation results presented, it can be concluded that the sensor triggering the product withdrawal should be preferably placed at high positions. The performed study of the average particles size removed from the crystallizer allows us to regard the position of the photosensor as a control element over the size of the resulting product population.

4.2.4 Model-based geometry analysis

One of the previous studies focused on studying the influence of crystallizer geometry is described in (Mangold et al., 2016). Using another model of the crystallization process, the main focus was on the assessment of the influence of geometry on process productivity. The geometry introduced above corresponds to the two crystallizers, L and D, of the experimental study designated as "Reference geometry". The geometry proposed in (Mangold et al., 2016), is used for the next round of the simulations as promising for achieving higher productivity.

A modified crystallizer geometry, designated as "Adjusted geometry", was suggested for obtaining higher productivity. The "Adjusted geometry" has a larger opening angle, a larger diameter of the cylindrical section, and a shorter total height. The geometrical parameters of the "Reference" and "Adjusted" geometries are given in Table 4.5.

Table 4.5 Geometrical parameters of the "Reference" and "Adjusted" geometries (L cryst.)

Parameter		Reference $[Ref]$	Adjusted $[Adj]$
Crystallizer height	$H, [m]$	1.052	0.757
Height of the conical part	$H_1, [m]$	0.49	0.51
Product outlet height	$H_{prod}, [m]$	0.335	0.356
Radius of the bottom	$R_1, [m]$	0.0126	0.0205
Radius of the top	$R_2, [m]$	0.0276	0.038
Volume of the crystallizer	$V_{total}, [l]$	0.511	0.665

Besides testing the new "Adjusted geometry", the comparison of the simulation and experimental results is made using a trade-off withdrawal strategy. As the best compromise for the tested geometries, the distance between the outlet and sensor positions was considered as $h_s - H_{prod} = 0.265\ m$, and the withdrawal segment, $\Delta h_p = 0.085\ m$. A comparison of the two geometries based on obtained simulation results using the developed model is shown in Figure 4.6. The volumetric feed flow rate, expressed as the empty tube velocity (u_{empty}) was adjusted to provide the same mean residence time of the solution in the reactor.

Analyzing the obtained results, it can be concluded that a larger empty tube velocity results in larger crystal size and lower process productivity. Within the simulation, it was found that using the "Adjusted" geometry should be capable of improving the performance in terms of productivity. The mean crystal size is reduced compared to the "Reference" geometry. These first theoretical results of the model study and the tools developed are considered to be helpful for further optimizing crystallizer geometry. Chapter 5 of this work consists of the results of geometry optimization, taking into account the assessment of the potential nucleation risk.

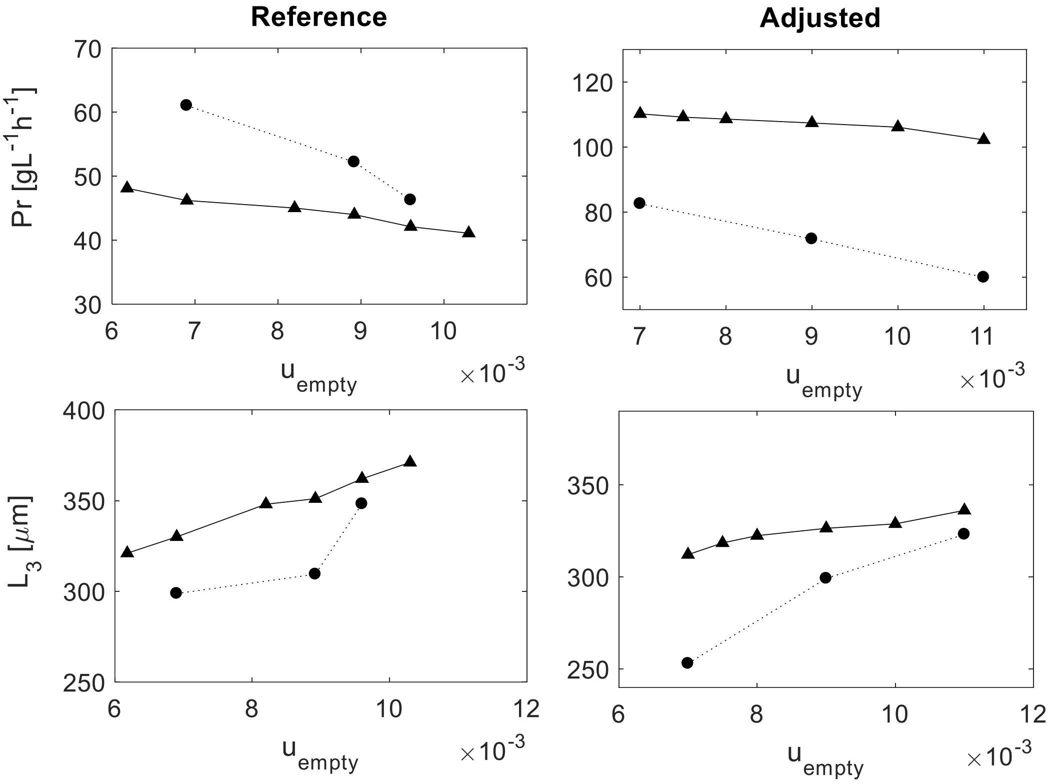

Figure 4.6 Productivity, Pr, and mean crystal size, L_3, over the empty tube velocity. Given are results for Reference and Adjusted geometries for L-crystallizer. The results of the process model are depicted for both geometries as solid lines, results of the experimental study are shown as dotted lines.

4.3. Local sensitivity analysis of the model parameters

In this subchapter, the relevance of the model parameters is studied in a local sensitivity analysis. The objective of the study is two-fold. On the one hand, the analysis will help to determine, which model parameters have to be adjusted carefully to measurements, and for which parameters a rough estimate is good enough in order to obtain a predictive model. On the other hand, the sensitivity study helps to find out which operation and design parameters have a strong leverage effect on the process's key performance parameters. It is essential to understand and relate key thermodynamic, kinetic, and operating parameters affecting product quality, such as productivity and particle size distribution. The idea behind this analysis is not only to assess the sensitivity but also to figure out if there is a dependence between process efficiency and geometry of the crystallizer.

Analysis methodology

To assess the parameter influences, a normalized sensitivity function is used that is defined as the approximate percentage change in an objective function for a fixed change in the studied parameter, p. As a fixed change, an increase of 10% is used. Only one parameter is varied per sensitivity assessment, while all other parameters are kept at their reference values (Büskens and Maurer, 2001). When changing the geometry parameters, the volume of the crystallizer is recalculated, and the feed flow rate is adjusted proportional to the cross-sectional area. The used definition of the sensitivity S_{kj} reads

$$S_{kj} = \left.\frac{\Delta OF_k}{\Delta p_j}\right|_{i \neq j}, where\ \Delta p_{j=} p_j^{nominal} - p_j = 0.1 \cdot |p_j^{nominal}|$$

[4.1]

In the above formula, OF_k is the process property or objective function under consideration. The following objective functions are investigated:

- OF_1= productivity $Pr_i = \frac{\dot{m}_i}{V_{total} \cdot \Delta h}$

[4.2]

- OF_2= mean particle size $L_3 = \frac{\int_{l=0}^{\infty} n(l) \cdot m(l) \cdot l \cdot dl}{\int_{l=0}^{\infty} n(l) \cdot m(l) \cdot dl} = \int_{l=0}^{\infty} l \cdot q_3(l) \cdot dl$

[4.3]

- OF_3= standard deviation from the mean particle size $s_{L,3} = \sqrt{\int_{l=0}^{\infty} (l - \overline{L_3})^2 \cdot q_3(l) \cdot dl}$

[4.4]

For comparison with the nominal case, a normalized sensitivity is calculated.

$$S_{kj}^{norm} = \frac{\Delta OF_k}{\Delta p_j} / \frac{OF_k^{nominal}}{p_j^{nominal}}$$

[4.5]

The choice of parameters studied in (Gänsch et al., 2021) has been extended for detailed analysis within this work. For a better understanding of the process, all the parameters are divided into groups. Each of the groups represents characteristics of the studied crystallization process given in Figure 3.1.

Table 4.6 List of parameters studied

Thermodynamic and kinetic parameters		**Operating parameters and withdrawal strategy**	
Solid density	ρ_{solid}	Inlet liquid concentration	c_{in}
Fluid density	ρ_{liquid}	Crystal temperature*	T_{cryst}
Sphericity	φ	Inlet liquid volume flowrate	$\dot{V}_{in}$
Solid heat capacity	$c_{p_{solid}}$	*Withdrawal strategy*	
Fluid heat capacity	$c_{p_{liquid}}$	Upper sensor position	h_s
Growth rate	G	Withdrawal distance	Δh_p
Nucleation rate	B_{nuc}	Desired void fraction at the sensor position	$\varepsilon_{desired}$
Density difference	ω		
Model assumption parameters		**Geometry parameters/Crystallizer setup**	
Number of daughters coming from mill	p	Crystallizer height	H
		Height of the conical part	H_1
Critical particle length	L_c	Diameter of the bottom	R_1
Sharpness parameter	q	Diameter of the top	R_2
Breakage rate kernel	S_0	Heat exchange coefficient	α_{cool}

Thermodynamic and kinetic parameters

The presented group consists of thermodynamic and kinetic parameters related to the particular chiral system. The studied parameters have validated values from the literature and laboratory experiments. However, changing them is of interest in view of the subsequent use of other components. Fluid and solid densities affect crystal productivity and size quite strongly because they determine the movement of the crystals relative to the liquid flow. Changing the growth rate of crystals speeds up the process by changing the duration of the time window between crystal harvestings (Δt). In turn, this changes the rate of the process and can be dangerous due to the increased risk of potential nucleation. In contrast, a change in the nucleation rate has no effect. The same absence of influence is confirmed for the solid heat capacity (cp_{solid}).

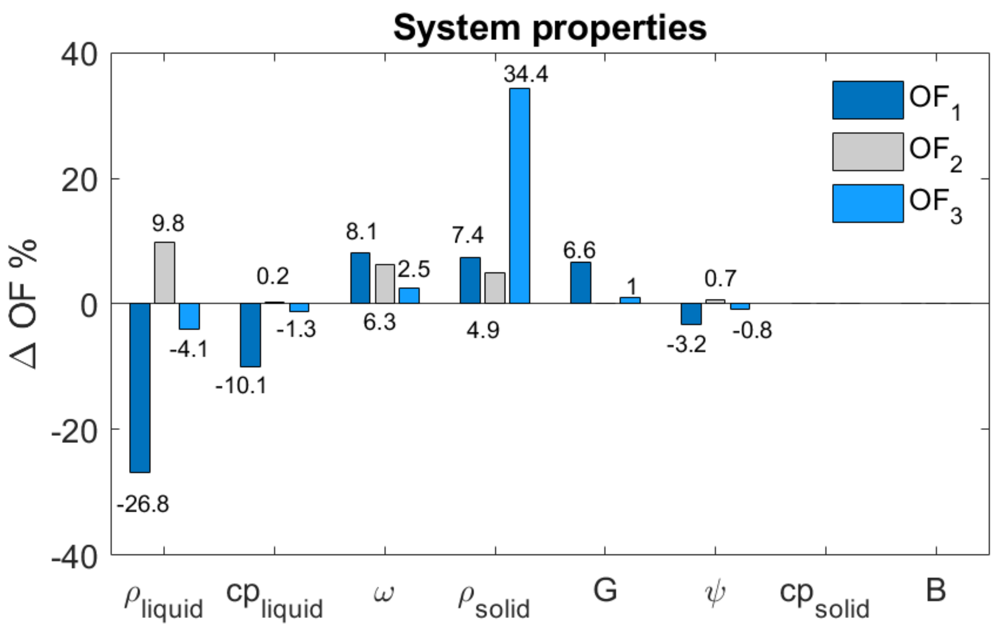

Figure 4.7 Influence of the thermodynamic and kinetic parameters

An increase in the solid phase density leads to a significant expansion in crystal size distribution. A fluidized bed concept is based on the density difference between liquid and solid phases. This difference is determined by the parameter $\omega = \rho_{solid} - \rho_{fluid}$. Several chiral systems have been tested to determine the concept's applicability. In the work of (Cascella, 2021), it is concluded that in the case when the density difference decreases to a certain level, as when studying the guaifenesin-water system, when $\omega = 470\ kgm^{-3}$, the operating conditions should be significantly adjusted to observe crystal growth. It can therefore be concluded that there is a range of permissible ω values, and the difference in densities of the asparagine-water system is within the acceptable range.

Operating parameters and withdrawal strategy

The following group, "Operating parameters," has reference values obtained from the experimental conditions in the laboratory. Among the selected parameters, the inlet liquid concentration (c_{in}) is found to have the strongest effect on the chosen objective functions, see Figure 4.11. The observed effect is not surprising because it immediately changes the supersaturation of the solution. The inlet volume flow rate ($\dot{V}_{in}$) also has a strong effect on productivity. Earlier in this work, when analyzing the geometry, this effect was already demonstrated in Figure 4.9. The applied withdrawal strategy is characterized by a set of several of the following parameters, whose influence has also been studied. Evaluation of parameters such as sensor position (h_s), withdrawal segment (Δh_p), and desired fraction of the liquid at the sensor position ($\varepsilon_{desired}$) allows us to make a prediction in terms of the productivity and crystal distribution.

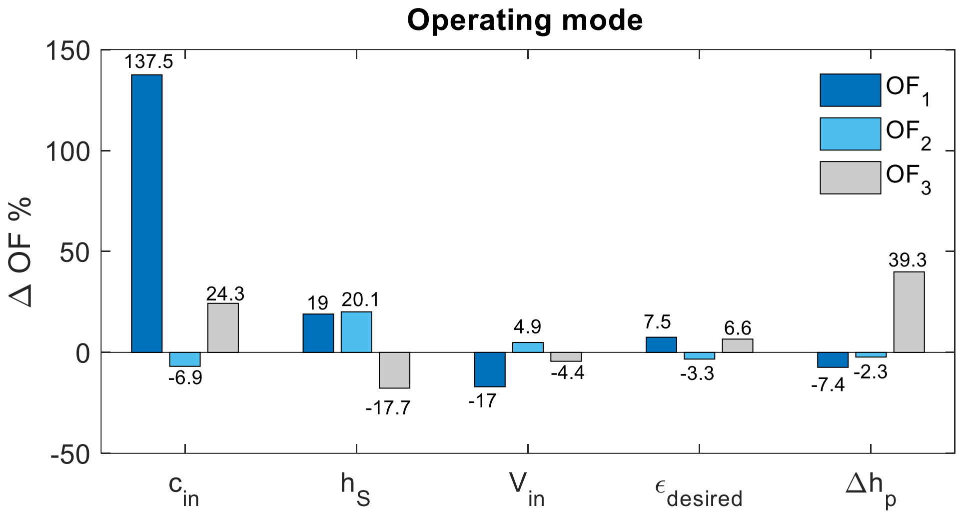

Figure 4.8 Influence of the operating parameters

As it was confirmed earlier in Figure 4.6 and Figure 4.8, parameters related to the withdrawal strategy play a significant role in process productivity. Moving the sensor position up will increase productivity and mean crystal size. In view of the extension of the seizure fragment (Δh_p) the crystal size distribution of the product is also changing. Nevertheless, a change in the withdrawn volume hardly affects productivity. Observable increase in the scatter of the population, bringing it closer to the characteristics achieved in the course of laboratory experiments (Gänsch et al., 2021).

Model parameters

The parameters listed in this group are those that either are hard to measure, or that result from model simplifications, when several physical effects are lumped in one heuristic parameter. One example is the critical size of crystals (L_c) in the mill model, which may roughly be interpreted as the gap between the rotating blade and stationary parts of the disperser. Such model inputs can be therefore only indirectly estimated by means of inverse analysis or taken from literature. Within the framework of this work, there are only a few parameters with this property. All parameters related to the grinding of crystals in the mill belong to this group. The heritage parameter (p) may be interpreted as the number of daughter fragments coming back to the process after a breakage event. The parameter q, is a sharpness parameter (Diemer et al., 2005). The parameters related to the mill model were identified in experiments, the estimation procedure is described in (Mangold et al., 2016).

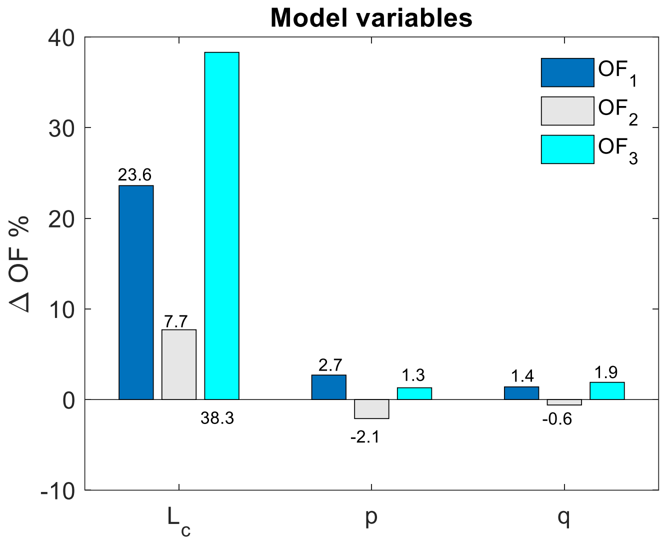

Figure 4.9 Influence of the parameters related to the model assumptions

From all the analyzed parameters in this group, the critical length of the crystal has the most significant influence. The change in crystal size distribution is accompanied by a considerable increase in productivity by 20%. However, a significant change is observed when analyzing the narrowness of distribution. Due to the lack of influence when changing the sharpness parameter can be excluded from the final parameter fitting procedure. The value determining the number of fragments after grinding should be taken into account when controlling the crystal size.

Crystallizer setup

Continuing the assessment of the geometry influence shown in Figure 4.9, the sensitivity analysis is performed by changing one of the parameters and then adjusting the input flow rate in order to provide the same mean residence time of the fluid in the reactor.

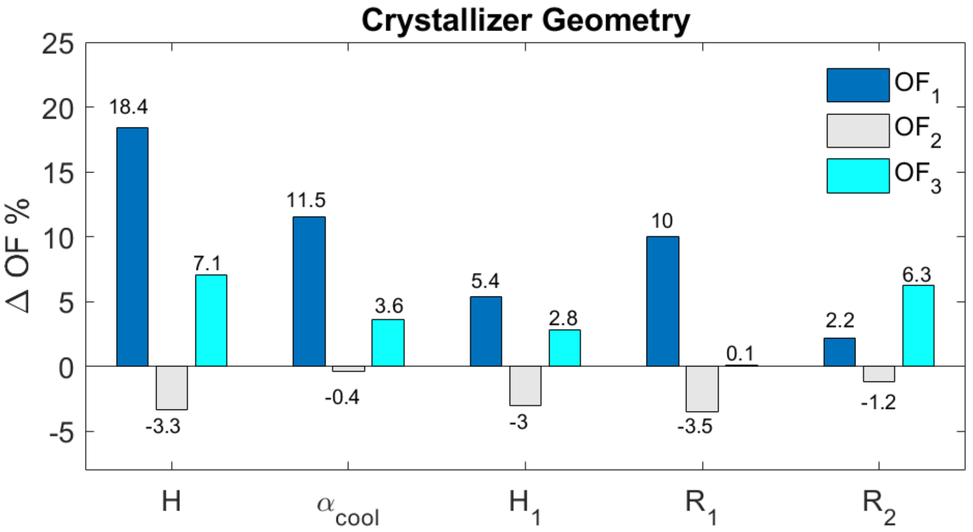

Figure 4.10 Influence of the production plant setup

As shown in Figure 4.10, all the geometry parameters influence the productivity of the process. Of greatest interest is the vertical expansion of the crystallizer, particularly the height of the cylindrical column, which determines the sensor position (h_s). Despite the increase in productivity, which is achieved by the extension of the height, there is a certain limit caused by the simultaneous increase in the total volume of and a significant increase in the risk of potential nucleation. The influence of the heat transfer coefficient causes a change in saturation and, as a consequence, the achievement of higher productivity.

It is obvious that the chosen approach, varying a single parameter while keeping all other parameter values constant, has its limitations. Nevertheless, the results may help to pre-select model parameters as optimization variables in numerical process optimization. The geometry optimization procedure described in the next Chapter gives an idea of the combination of geometry and operating parameters that can be suggested to increase productivity and ensure process stability.

Temperature and Supersaturation

In Figure 4.11, it has already been demonstrated that changing the initial concentration of the liquid (c_{in}) has a significant influence on supersaturation. The saturation temperature (T_{sat}) and the crystallization temperature (T_{cryst}) are no less important parameters. An experimental study on the influence of temperature and supersaturation on asparagine monohydrate/water system was published earlier in (Temmel et al., 2018).

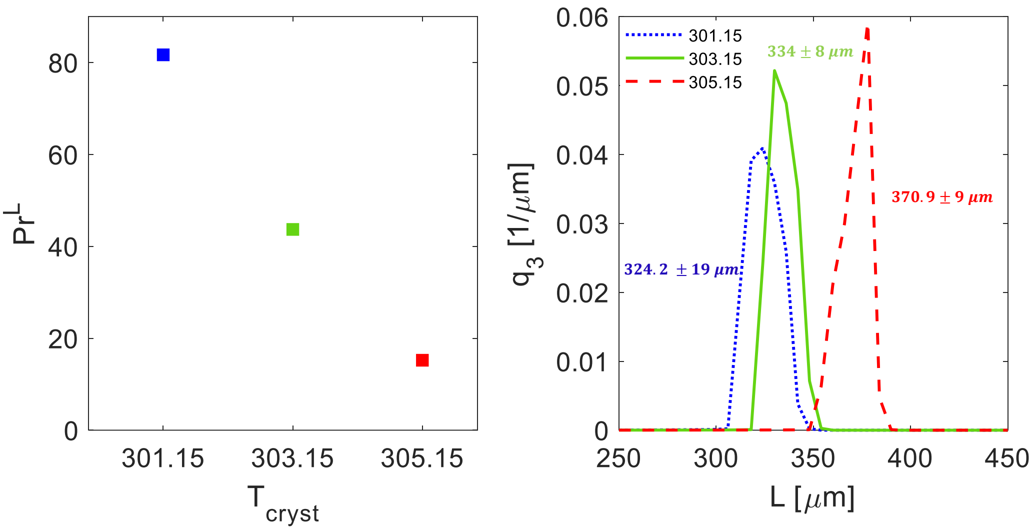

Figure 4.11 Influence of the Crystallization Temperature (T_{cryst}) on the productivity (Pr), and CSD, with their respective mean values and standard deviations. Crystallization Temperature (T_{cryst}) is measured in the middle of the reactor.

Within three simulation rounds a suitable operation window and, hence, three different supersaturation values are tested. A constant volumetric flowrate (12 lh^{-1}) and saturation temperature (T_{sat} = 308.15 K) are ensured during all three experiments. The process of preferential crystallization in a fluidized bed is simulated in the same manner at $T_{cryst} = 301.15\ K$, $T_{cryst} = 303.15\ K$, and $T_{cryst} = 305.15\ K$, which corresponds to supersaturations of S = 1.49, 1.324, and 1.18, respectively. Figure 4.14 (left) shows that the supersaturation clearly enhances productivity which correlates with the growth kinetics of the given substance system.

Summary of the model demonstration

Based on the obtained results, the developed model introduced in Chapter 3 is considered a solid and promising instrument for the crystallization process understanding and subsequent operating control. The proposed modeling framework demonstrated itself as a well-capable tool to describe essential process features on a qualitative and quantitative basis, as well as it helped to identify suitable operating conditions for achieving higher productivity or providing control on crystal size distribution. Implementation of all the framework constituents, such as the selected process variance, conditions for the operating regime, periodical product withdrawal, and properties of the chemical system, made it possible to compare simulation results with the experimental study. Based on both our experimental and theoretical results, provided study offers the following conclusions:

- When the developed model is used in association with data on a specific crystallizer and chiral system, it confirms the experimental outcomes with high accuracy;
- The concept of a fluidized bed proposed in (Binev et al., 2016) to increase productivity is validated within this work. The results obtained indicate a significant increase in productivity when the sensor position is placed at higher positions;
- The "Adjusted geometry" proposed in (Mangold et al., 2016) is studied using the available system properties. The obtained numerical solutions indicate its applicability and superiority over "Reference" geometry;
- Developed recommendations for changing the crystallizer height and width are taken as a basis for the subsequent search for the optimal geometry setup;
- Sensitivity analysis presented as a conclusion of the model demonstration is considered to be helpful for selecting powerful variables for numerical process optimization, which is the subject of the following Chapter.

Despite a good agreement between simulation and laboratory studies, the developed model also shows some deficiencies. As shown in Figure 4.7, the model is limited in predicting standard deviations of crystal size distributions. CSD prediction could be improved by expanding the range of simulated phenomena such as particle agglomeration. Nevertheless, since the key characteristic is the mean size of crystals within the withdrawn population, this model is accurate enough.

Changing parameters affects the resulting productivity and other process performance reflected in the studied objective functions. It is expected that the result of such kind of optimization will be a combination of operating parameters at which a compromise can be found between two conflicting criteria – process productivity and product purity. Of particular interest is the application of the developed model to determine the operating regime and crystallizer geometry for the separation process of the chosen chiral system. The objective here is to generate the optimal temperature at the desired position, reasonable empty tube velocity, and to find a set of geometry parameters, which maximize the process productivity taking into account the risk of the potential nucleation. The posed optimization problems are discussed in detail in Chapter 5.

5. Process optimization

At the beginning of this chapter, the literature review briefly introduces the current stage in the field of model-based control of crystallization. Applied to the enantioseparation problem posed in Chapter 2, objective functions and optimality criteria are taught to assess the resulting solution's applicability. The methodology for obtaining numerical solutions is discussed regarding how applicable each algorithm is to the problem posed. Due to the complexity of the developed model and the high cost of computational time and resources, special attention is paid to parallel computations. The final part of this chapter discusses the results of solving specific optimization problems.

5.1 Advanced control of crystallization processes

Year by year, the challenges in controlling crystallization do not cease to increase. When it comes to the production of drugs, the pharmaceutical sector especially needs to overcome the existing difficulties. Regulatory requirements, customer needs, and growing market competition are becoming more challenging. This, in turn, leads the industry to seek alternatives for ensuring economic efficiency and science to propose new studying approaches for better process understanding. To a certain extent, the pharmaceutical business model has been based on discovering new molecules and the protection of existing patents.

Nevertheless, new drug development costs increase over time when the expiry time for patents remains unchanged. The way out of this situation is to shorten the time for bringing medicines to the market to extend the duration before the patent expires. Consequently, the current procedures of producing new drugs and satisfying market requirements need to be optimized. Various initiatives have been introduced in the industry over the last decades. Some of the proposed approaches are based on the use of process analytical technology (PAT), the concept of quality by design (QbD), and the development of continuous pharmaceutical manufacturing (CPM) (Brown et al., 2020).

Most pharmaceutical manufacturing processes include a series of crystallization processes to achieve high product purity and to produce the desired final crystal form. These characteristics are directly related to the operating conditions in which crystallization is carried out. The crystallization process's operating regime determines the products' physical properties, such as the crystal purity, size, and shape distribution.

In this section, a brief introduction to the control of crystallization processes is given. Even though there are some model-free approaches to ensure process robustness (Griffin et al., 2015), the main focus of this study is on model based techniques due to their ability to predict and efficiently provide information. A more comprehensive review of the current stage of advanced process control techniques can be found in (Nagy et al., 2019) and (Lakerveld and Benyahia, 2020). Schematically, model-based optimization of a (crystallization) process concerning some generic objective function (f) can be viewed as the following mathematical problem:

$$
\begin{aligned}
& f(x) \rightarrow \text{min} \,/\, \text{max} \ \text{ subject to} \\
& \quad \bullet \ \ model\ equations\ (manipulated\ variables) \\
& \quad \bullet \ \ constraints \begin{cases} technical \\ economic \\ experimental \end{cases},
\end{aligned}
\qquad [5.1]
$$

The objective function generally depends on the time, the system's state (density function and its moments or nucleation/growth rates), and the inputs (inlet temperature, applying coolant strategy, initial seeding procedure). Constraints usually define the physical feasibility of the experiment and make sure that process is economically sufficient.

The challenges in controlling crystallization are significant. First, there are a large number of uncertainties due to process kinetics. The observed changes in supersaturation can cause nucleation bursts or depletion of nuclei, severely affecting the process dynamic. On the other hand, model-based crystallization control poses a mathematical problem that is extremely difficult due to its nonlinearity and nonconvexity. The transition to a multi-criteria optimization problem brings uncertainties associated with different impacts on the process components and their nature.

The production of a solid-phase material gives excellent opportunities to influence the amount and purity of the produced crystals, their size, and shape characteristics.

Consequently, optimization problems can be targeted across a larger area. This, in turn, provides the possibility of multilevel control over the process - starting with the growth mechanism of crystals and gradually scaling the posed problem to the size of industrial production (Desikan et al., 2000). The solution pathway discussed later in this chapter is also difficult to generalize: different authors have used numerical methods to find optimal solutions because no single strategy shows a clear superiority over others.

5.2 Model-based optimization of continuous preferential crystallization

The first-principles approach to crystallization control is the most widely studied (Nagy and Braatz, 2012). This method is based on a model constructed from material and energy balances, used to optimize some objective function. Depending on needs and constraints, as shown in Figure 5.1, the objective can be mean crystal size, particle size distribution, or other product characteristics. For a detailed review of model development for solution crystallization, the readers are referred to Chapter 3 of this work, where existing approaches to process modeling are discussed. To simplify the model, most of the studies in the literature consider nucleation and growth mechanisms, neglecting agglomeration phenomena or crystal shape changes.

The process of crystallization control can be schematically represented, as shown in Figure 5.1. The procedure of finding optimal operating conditions requires available compound characteristics, results of experiments, parameter estimation, and correct model selection.

The main challenge associated with the first-principles approach is the requirement of accurate crystallization kinetics measurements. The analysis of data related to the use of sensors has become easier over the past decades due to the improvement of the equipment used. Despite some advances in technology, the main phenomena as polymorphism, particle agglomeration, and unwanted nucleation bring uncertainties in determining crystallization kinetics (Wunderlich, 1993). The variability of the parameters due to the presence of impurities in the feed is still of the greatest importance.

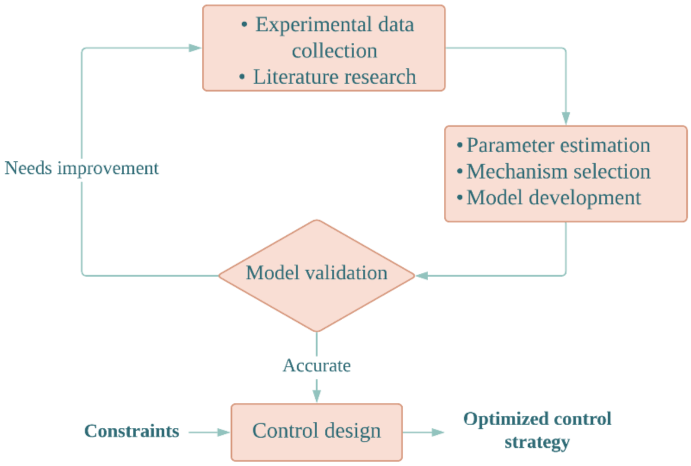

Figure 5.1 The procedure of optimal control design is based on the first-principles approach. The results of the conducted experiments and data available from literature research are used as input parameters. The estimated parameters and the selected mechanisms to be modeled reflect the process dynamics. In the case of successful model validation, an optimal solution is sought for the posed optimization problem.

One of the most advanced model-based methods for controlling Temperature is the model predictive control (MPC). The main goal of the MPC is to determine the sequence of control moves required to obtain predicted model output at the desired level. García (García et al., 1989) have formed the first significant review of the linear control strategy and its applicability to the oil and gas industry. Later on, a good overview of the nonlinear methods applicability crystallization process was given in (Nagy and Agachi, 1997). The main focus of the study is on controlling crystallization temperature to ensure a stable profile overreaction. With the proposed control algorithm, the operation of the crystallization process, even with frequent changes in temperature profile, is considered possible and efficient. Recent publications can also find other examples of temperature manipulation and design of optimal cooling strategies (Nagy and Agachi, 1997; Nagy & Braatz 2003; Nagy and Braatz, 2012; Kim et al., 2009). Application of the model predictive control for temperature profile optimization for cooling and antisolvent crystallization techniques can be found in (Yang and Nagy, 2014).

Since crystallization usually targets particle size distribution (PSD) or related particle properties, some strategies to control mean crystal size or particle distribution are also of great interest. In the research work of Worlitschek and Mazzotti (Worlitschek and Mazzotti, 2004), the constrained nonlinear model-based optimization strategy is applied to design specific particle size distribution in batch-cooling crystallization of Paracetamol. Typically, when optimizing CSD, the desired mean size (Anderson, 2001) or the whole final CSD are targeted (Trampuž et al., 2021; Worlitschek and Mazzotti, 2004; Aamir et al., 2010; Nagy et al., 2011; Majumder and Nagy, 2013; Ridder et al., 2016).

Another important aspect, which is even less understood than size distribution, is the crystal shape morphology. The main reasons for this are the complexity of the interaction between the solid and the liquid phases, complicated mechanisms of crystal growth, and the influence of particle interactions. Research of particle evolution control taking into account purity tracking can be found in (Boros et al., 2016). Hütter (Hütter et al., 2005) provided the morphological analysis for polymer crystallization to investigate processing conditions influence. Dynamic crystallization model was used to predict changes in crystal morphology depending on the thermodynamic driving force behind the growth rate. The relation between crystal shape and thermodynamic driving forces, operating conditions, and target particle shape were established using a morphological description of shape-changing and available experimental results.

In recent years the number of studies devoted to continuous solution crystallization for reproducible manufacturing has been significantly increased. Continuous crystallization contributes to high product reproducibility, economic efficiency, and low production costs corresponding to other production technologies. As discussed earlier, in Chapter 2 of this work, the successful design of the continuous crystallization process is usually based on a deep understanding of batch processes. A review article authored by Jiang and Braatz (Jiang and Braatz, 2019) gives a broad understanding of the relationship between batch and continuous crystallization processes. To ensure a robust continuous process, some specific conditions must be met. The 5-Step design procedure of efficient continuous crystallization consists of:

- understanding product specifications to be satisfied (solid form, crystal shape, purity, etc.);
- collecting thermodynamic data;
- selecting operating regime based on batch operations results;
- determining of suitable continuous crystallizer configuration;
- design flow and temperature conditions.

The proposed approach combined with a powerful predictive model of crystallization phenomena may benefit in a continuous, highly productive crystallization process.

Following an overview of the theoretical background and existing approaches to model-based optimization, the following section explores the application methodology and evaluation of the optimal solutions found.

After the sensitivity analysis has been conducted and the model's reliability has been assessed, as described in Chapter 4, the preferential crystallization process optimization can be performed. This work presents new model-based optimization approaches, targeting increasing process productivity and ensuring the absence of product contaminations. Continuous preferential crystallization of asparagine monohydrate in fluidized beds is chosen as the model system. Thermodynamic and kinetic phenomena of the process have been examined in previous studies (Temmel et al., 2018). The mathematical model used for the process description is presented in detail in Chapter 3. The preliminary model study results are published in (Gänsch et al., 2021). Optimization results based on the developed model have been published previously in (Huskova et al., 2021) and presented at [Huskova et al., 2021, ProcessNet]; [Huskova et al., 2021, ISIC].

First, a numerical solution of the cooling crystallization model using previously estimated kinetic parameters is simulated to investigate the impact of operating parameters on product contamination. A simple and efficient approach is used to simultaneously optimize the importance of some of the essential batch crystallization running conditions to achieve a trade-off between the harvested mass of the crystals and solution purity. The second block of optimization calculations is devoted to the problem of potential contamination in the resulting solution. Analyzing data on the height of the fluidized bed and the presence of the counter enantiomer, recommendations regarding operating mode and geometry of the crystallizer are formulated along with a new approach to determining purity.

Optimization problem

The developed mathematical model describes particle and fluid dynamics, process kinetic in the non-isothermal case, mass and heat transferring. Obtaining an exact solution requires very dense grids over the computational domain. To ensure high accuracy of the numerical solution, the number of differential equations resulting from a discretization of the space and property coordinate exceeds 20 000. The model describes the position of the solid phase in space and the corresponding particle size, the concentration of the liquid phase, and the change in temperature conditions. Based on this, many resources are spent at each moment, making obtaining a numerical solution resource and time-intensive. The elapsed time exceeds several hours to calculate the transient to a cyclic steady state for one set of parameters. The size of the developed model and time constraints lead to the inability to use a single processor to obtain optimal parameters and improve the process. In this regard, within this work, an attempt is made to directly solve the problem of reducing the computational requirements without compromising the accuracy of the developed mathematical model through parallelization methods.

Optimality criterion

The criterion of optimality is a quantitative assessment of the optimized process design. The optimality criterion is the main criterion, judging how well the technological process works and how the posed optimization problem is solved. The optimality criterion is one of the outputs of the simulation, and the following requirements are imposed on it:

1. The measure of optimality should be expressed quantitatively.
2. The criterion of optimality should reflect the most significant characterizations of the process.
3. It is desirable that the optimality criterion has a clear physical meaning and is easy to calculate.

Based on the chosen optimality criterion, an objective function depends on the selected inputs that affect its value. A specific optimization problem determines the type of optimality criterion or objective function. The most general formulation of the optimal situation is the expression of the optimality criterion in the form of an economic assessment (productivity, production cost, profitability). However, in particular optimization problems, when an object is a part of a technological process, it is not always possible or always advisable to single out a direct economic indicator that would fully characterize the efficiency of the process. In such cases, the criterion of optimality can be a technological characteristic that indirectly evaluates the efficiency of the unit operation (duration of the production cycle, purity of the resulting product, degree of conversion).
The difference between simple and complex criteria is based on applied constraints. An optimality criterion is called simple if it is required to determine the extremum of the objective function without setting conditions on any other variables (Hwang et al., 1979).

Such measures are usually used to solve particular optimization problems. In contrast, the optimality criterion is called complex if it is necessary to establish the objective function's extremum under certain conditions imposed on some other values and constraints. The procedure for solving the optimization problem must therefore include, in addition to the choice of control parameters, also the restriction of these parameters. Rules can be imposed for both technological and economic reasons. As applied to the crystallization process under study, the main task of mathematical optimization is to maximize productivity, taking into account the risks of possible product contamination.

5.3 Methodology

When solving a specific optimization problem, it is desirable to choose the method with the smallest computational effort. The choice of such methods is determined mainly by the formulation of the optimization problem and the complexity of the used mathematical model. Choosing one or another optimization method requires a deep understanding of the modeled process. Some methods at certain stages of solving the optimization problem can be used in combination with others. At the same time, some optimization methods are specially designed and in the best possible way suitable for solving specific problems.

5.3.1 Gradient-based optimization strategies

Gradient-based algorithms are developed to find the nearest local optimum (Kantorovich and Akilov, 1982). These algorithms work with calculating the gradient of the objective function at a point in question. The slope can be calculated analytically from the gradient vector function; otherwise, a pseudo-gradient is needed (Wolfe, 1969). The pseudo-gradient can be estimated experimentally by producing the derivative of the objective function with minimal steps. The mathematical optimization problem can be formulated in equation [5.2].

$$\min_{x \in R} f(x) \qquad [5.2]$$

In the multidimensional case, similarly from the linear approximation $f(x) \approx f(x^*) + \nabla f(x^*)^T(x - x^*)$, where $x^T y = \sum_{i=1}^{n} x_i y_i$ is a standard inner product. The quantity $\nabla f(x^*)$ is the gradient of the function f at the point x^*.

$$\nabla f(x^*) = 0$$

[5.3]

The equality of the gradient to zero means the equality of all partial derivatives to zero. Therefore, in the multidimensional case, this criterion can be obtained simply by successively applying the one-dimensional criterion for each variable separately. The gradient should be zero at the minimum point when the investigated function is differentiable (it has derivatives concerning all variables). However, a nonzero gradient also provides valuable information.

If there is a given point, x, finding $\bar{x}$, that $f(\bar{x}) < f(x)$ is possible using linear approximation:

$$f(\bar{x}) \approx f(x) + \nabla f(x)^T(\bar{x} - x).$$

[5.4]

In a case, when $\bar{x} = x - \alpha \nabla f(x), \alpha > 0$, the function reads

$f(\bar{x}) \approx f(x) - \alpha \|\nabla f(x)\|^2 < f(x)$,

[5.5]

where $\left\|x\right\| = \sqrt{x_1^2 + x_2^2 + \cdots + x_n^2}$.

Analogically, if $\alpha < 0$, the result is $f(\bar{x}) > f(x)$. To summarize, it is possible to conclude that if $\nabla f(x) \neq 0$, the gradient indicates the direction of the strongest local increase in the function. Knowing how having a point x to obtain point $\bar{x}$ with a lower function value, the sequence of actions can be repeated. The resulting sequence reads

$$x_{k+1} = x_k - \alpha_k \nabla f(x_k),$$

[5.6]

where α_k is a step size (sometimes called a learning rate), which should be chosen optimally to prevent slow algorithm operation on the one hand, and its break on the other.

Gradient-based challenges

As noted earlier, a specific optimization problem requires a suitable solution methodology that will allow one to obtain information about the optimal points in the shortest computational time. The described gradient-based optimization strategy has some disadvantages:

- Choosing a proper learning rate can be difficult. A step size that is too small leads to painfully slow convergence, while a learning rate that is too large can hinder convergence and cause the loss function to fluctuate around the minimum or even to diverge.
- Another key challenge of using gradient-based strategy is avoiding getting trapped in their numerous suboptimal local minima. Such difficulty arises not from local minima but saddle points, i.e., points where one dimension slopes up and the other slopes down. These saddle points are usually surrounded by a plateau of the same error, making it notoriously hard for the algorithm to escape, as the gradient is close to zero in all dimensions (Dauphin et al., 2014).
- Gradient algorithms are characterized by the dependence of the solution at a point x_{k+1} on the solution at the previous point x_k. This greatly complicates the speed-up of computations by parallelization, although there are approaches to ensure parallel computations in the case of using derivative required approaches (Missirlis and Tjaferis, 1995).
- The most significant drawback when using gradient-based optimization is that the methods get stuck at local minima and are therefore only applicable to convex problems (Kantorovich and Akilov, 1982).

Since the nature of the studied problem to find the optimal crystallization conditions is very nonlinear, time-consuming, and possesses many local optima, ordinary optimization methods such as sequential gradient-based algorithms cannot provide the solution. Thus, optimization requires a technique that can find the global optimum in a solution space.

5.3.2 Evolutionary strategies

Evolution strategies are classical variants of evolutionary algorithms, which are widely applied to solve different optimization problems (Vikhar, 2016). This chapter will describe the chosen strategy and its advantages compared to other methods for solving optimization problems.

Returning a little to history, the idea of using principles of biological evolution to optimize technical systems arose in Germany (Vent, 1975). The algorithms developed at the end of the '60s were successfully used to solve engineering problems. In the mid-1990s, these strategies were combined in a particular class called evolutionary algorithms. Nowadays, evolution algorithms are mainly used for simulation-based optimization. The high demand is due to the use of mathematical models that require parameter optimization. Described algorithms are suitable for such optimization problems because they are independent of derivatives. In the specific application field of evolution strategies, the optimization problem is given the same way as in [5.2].

The objective function (f) can be a black-box function; usually, it is assumed to be nonlinear and has a minimum value. On the opposite, maximization problems can be posted by changing the sign of f. Basic implementations also allow choosing intervals, introducing constraints, and restricting the domain of decision variables. When an evolution algorithm is launched, a "virtual" population of individuals is created. Each of the individuals represents an element of the solution space. The adaptability of individuals to environmental conditions is expressed by a specific monotonic fitness function, which is equivalent to the objective function of an optimization problem. The better the solution, the higher the value of the fitness function of individuals with the corresponding genotype. The population develops due to selecting more suitable individuals and applying random operators to them, imitating gene mutation and recombination of parental genotypes (crossover). There are many different approaches to carry out the selection of individuals. The basic structure of the algorithm is outlined below.

```
//Algorithm 1:Evolution Strategy
input: initial population $P_{initial}$ with $\mu$ individuals
$t \leftarrow 0$                                                  {Generation counter}
$(x_1^{best}, f_1^{best})$ = Update $P_{initial}$                 {Initialize best solution}
while termination criterion not met do
    $t \leftarrow t + 1$
    $R_t \leftarrow$ Recombine $P_{t-1}$          {Create $\lambda$ offspring from $P_t$ using Recombination operator}
    $M_t \leftarrow$ Mutate $(R_t)$                       {Create mutant applying Mutation operator}
    $C_t \leftarrow$ Evaluate $(M_t)$                     {Evaluate fitness function}
    $(x_{t+1}^{best}, f_{t+1}^{best})$ = Update $(C_t, x_t^{best}, f_t^{best})$    {Update best found solution}
    $P_t \leftarrow$ Select $(C_t, P_{t-1})$              {Select the $\mu$ best individuals}
end while
return $x_t^{best}, f_t^{best}$
```

Figure 5.2 The basic algorithm of a (μ, λ) – Evolution Strategy

The algorithm starts with the creation of a population $P_{initial}$. The population consists of μ parent individuals. The search for a solution is conducted in feasible intervals for the optimization variables x, applying random sampling. After finding the fitness values of $P_{initial}$, the best solution found in the population is stored in the variables $x_{initial}^{best}$ and $f_{initial}^{best}$. The following generational loop is executed until the termination criterion is met. The most widely used stop criteria are the lack of improvement in the resulting solution and the maximum allowable search duration (number of iterations). Described here, the search process is determined by two stochastic operators – **recombination** and **mutation**, and one deterministic **selection** operator. The first, recombination operator, creates from the μ individuals in $P_{initial}$ a new young population (P_t) that consists of λ individuals. Those individuals can mutate using a mutation operator. The mutation process leads to the updating of the evaluated before $x_{initial}^{best}$ and $f_{initial}^{best}$ values in a case when better candidates are found. The next generation parent population of μ best solutions is selected from the young λ individuals.

The main components of such a strategy are recombination, mutation, and selection. In each iteration, like in a biological population, new individuals are generated in a stochastic way, using previous parental individuals. Based on fitness and objective function values, some individuals from the current population are selected to become the parents of the subsequent population. Individuals inside subsequent populations will have better fitness and objective values over the generation sequence. The inheritance of this principle leads to the improvement of the following populations.

5.3.3 Derandomized evolutional strategies

Considering information about the main stages of the evolutionary algorithms, we can conclude the importance of the mutation parameter for subsequent populations. There are different strategies for controlling or improving the mutation parameters:

- Step-size control;
- Mutative step-size control;
- Derandomized step-size control.

The covariance matrix adaptation evolutionary strategy (CMA-ES) is a derivative-free method (Hansen, 2006) to solve continuous optimization problems. This kind of optimization framework, which is considered general, has many appealing characteristics and is particularly useful for solving problems that are deemed non-convex. Since CMA-ES belongs to Evolution Strategy (ES), it operates in the same significant steps: recombination, mutation, and selection. Applying CMA-ES requires explicitly defining a finite-dimensional search space in which solution candidates exist. Optimization objectives are typically defined as cost functions of parametric solution functions.

In CMAES, a parametric distribution is formed over the solution space, such as the space of the policy parameter in policy search or the area of the parameters of the loss function in inverse optimal control. Using a parameterized distribution, it samples solution candidates iteratively. A black-box process is then used to evaluate the candidates. As a result of candidate evaluation, CMA-ES can update its search distribution, means, and covariance matrix.

Specifically, a cost function (f) is parametrized by a parameter space $x \in R, f(x)$. The target is to find an optimum parameter x^* such that $f(x^*)$ is minimum. It is common that a CMA-ES algorithm maintains a multivariate Gaussian distribution over the solution space as $x \sim N(x; m, C)$, where m is an n-dimensional mean vector and C is a $n \times n$ covariance matrix. At each iteration k, the k^{th} the population of λ offsprings is generated from the k^{th} distribution by random sampling as $x_i \sim N(x; m_k, C_k),\ i =$

$1, \ldots, \lambda$, where m_k and C_k denote vector with mean values and the covariance matrix at iteration k (when m and C are updated k times). Then, the offspring are sorted according to the obtained value $f(x_i)$. Only best candidates μ (following $\mu < \lambda$) are selected for updating of m_k and C_k at the next step. Another crucial parameter is the global step-size $\sigma \in R$ that controls the convergence step of the covariance matrix update. The parameter σ is described as a global standard deviation for each of x parameters. A complete set of parameters in CMA-ES is $\{m, C, \sigma\}$.

```
// The CMA-ES algorithm

1:     Initialize $m \epsilon R^n, x \epsilon R^n, \lambda, \mu$
2:     Initialize $C = I, p_c = 0, p_q = 0$
3:     while not terminate do

4:         Sampling:$x_i = m + \sigma y_i, y_i \sim N(0, C), i = 1, \ldots, \lambda$
5:         Evaluating $f(x_i), i = 1, \ldots, \lambda$
6:     // mean update
7:         $m \leftarrow m + \sigma \bar{y}, where\ \bar{y} = \sum_1^\mu w_i y_{i:\lambda}$
8:     // step size control update
9:         $p_\sigma \leftarrow (1 - c_\sigma) p_\sigma + \sqrt{c_\sigma (2 - c_\sigma) \mu_w} c^{-1/2} \bar{y}$
10:        $\sigma \leftarrow \sigma \exp\left(\frac{c_\sigma}{d_\sigma}\left(\frac{\|p_\sigma\|}{E\|N(0,I)\|} - 1\right)\right)$
11:    // covariance matrix update
12:        $p_c \leftarrow (1 - c_c) p_c + \sqrt{c_c (2 - c_c) \mu_w} \bar{y}$
13:        $C \leftarrow \left(1 - c_1 - c_\mu\right) C + c_1 p_c p_c + c_\mu \sum_1^\mu w_i y_{i:\lambda}\, y_{i:\lambda}$
14:    end while
```

Figure 5.3 The basic CMA-ES algorithm

In Figure 5.3, a summary of the CMA-ES algorithm is given. The described algorithm starts with an initialization of the parameters in steps 1 and 2. Consistently, the parameters $\{m, C, \sigma\}$ are updated as demonstrated in steps 4 to 13. Step Four is a sample selection from a normal distribution with mean m and covariance C. Step 5 represents a process of function evaluation when $f(x_i)$ for each of $\lambda -$ individuals are found. The updated mean is a weighted sum of the best μ candidates as in step 7, where the weights w_i are set to $1 / \mu$ or an alternative $w_i = log(\mu / 2) - log(i)$; $yi : \lambda$ means the best-found candidate out of $yi, \ldots, y\lambda$.

The covariance matrix update demonstrated in step 13 is composed of three procedures: (1) collecting of old information, (2) rank-1 updating, which computes the change of the mean over time in the evolution path, p_c, and (3) rank-μ updating, which considers variations within the last population. Step 10 devotes to the step-size control update that constrains the expected changes of the distribution. As a result, this step is built on the conjugate evolution path $\mathbf{p}\sigma$. It aims to accelerate convergence towards an optimum while preventing premature convergence.

Other parameters such as μW are the variance effective selection mass, c_1, c_c, c_σ are used learning rates, and d_σ is a damping factor for σ. A detailed discussion of the parameters set is given in (Hansen, 2006). Termination criterion can be determined in various ways depending on the contracting covariance or fitness functions (e.g., if fitness functions do not change for some iterations).

Benefits of using the CMA-ES algorithm. Parallelization

Among many advantages of the CMA-ES, its derivative-free methodology is in a field of interest compared to other optimization algorithms. At the initialization stage, an initial solution point , $x_{0,}$ and initial step-size, σ_0, have to be chosen. Another parameter that can also be modified is the number of candidate samples λ, so-called population size. Termination conditions are an absence of improvement or reaching the maximum allowable execution time of the algorithm but can also be adjusted. In addition, a significant benefit of using the CMA-ES algorithm for modern optimization problems is the opportunity of applying parallel computations for obtaining numerical solutions.

5.4 Applicability of parallel computing for obtaining numerical solutions

The organization of parallel computations, when several data processing operations are performed simultaneously at the same time, is carried out mainly by the introduction of redundancy of functional devices (multiprocessing). In this case, it is possible to accelerate the solution of a computational problem by dividing the applied algorithm into information-independent parts, executing each part of the computations on a different processor. This approach allows one to perform the necessary calculations in less real time. Amdahl's law is often used in parallel computing to predict the theoretical speedup when using multiple processors (Hill and Marty, 2008). Nevertheless, the use of parallelism has not yet become as widespread. Until recently, one of the possible reasons for this situation was the high cost of implementing high-performance systems. Nowadays, the main reason is the inability to split the original block of instructions into subtasks executed independently of each other (Hager and Wellein, 2011). Figure 5.4 shows two opposite approaches to solve a computational task.

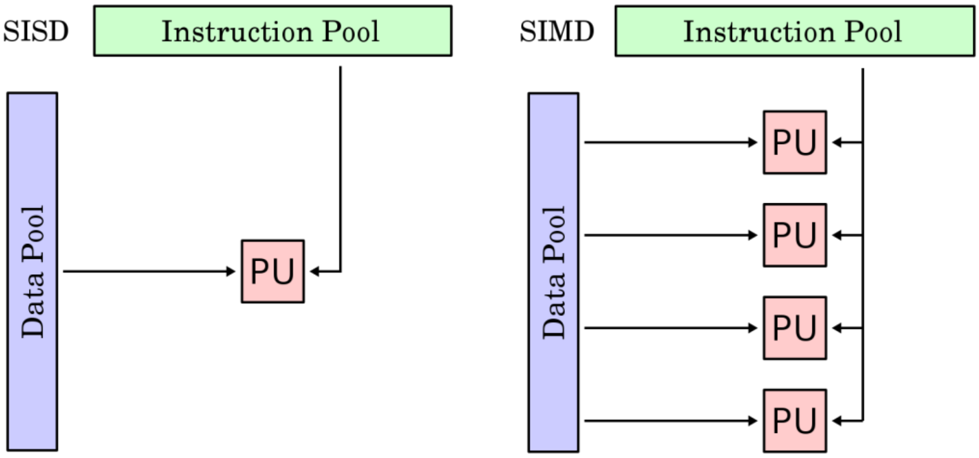

Figure 5.4 SISD approach (Single Instruction: Only one instruction stream is being acted on CPU /Single Data: Only one data stream is being used) versus SIMD (Single Instruction: All processing units execute the same instruction/Multiple Data: Each processing unit can operate on a different data element).

In the context of the optimization problem introduced earlier in this section, Instruction Pool may be expressed as the process of obtaining a numerical solution for a set of differential equations formed by a specific set of input parameters (Process Unit). In addition to approaches shown in Figure 5.4, MISD and MIMD architectures can be applied. However, in the context of this work, only the SIMD approach is under consideration.

Principles of parallelization

For the effective implementation of the task, the amount of computation for each processor used should be approximately the same - this will ensure uniform computational load (balancing) of processors. Besides, the distribution of subtasks between processors should be done to minimal communication interactions between subtasks (Sudholt, 2015). Guided by these principles, the applied parallelization scheme is presented in Figure 5.5.

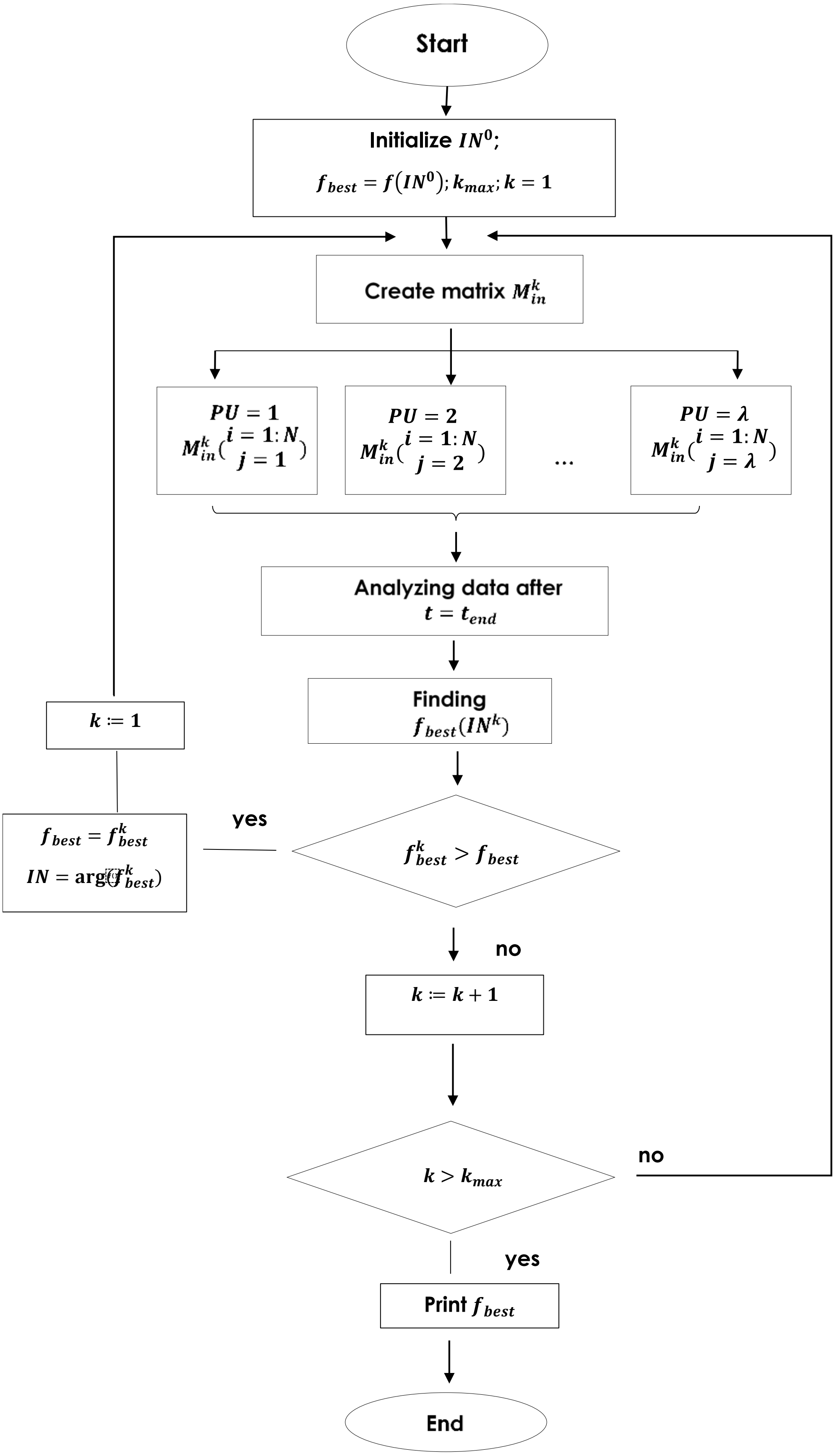

Figure 5.5 Block diagram for finding the optimal solution using parallel computations.

The process of obtaining an optimal solution consists of the following stages:

- Beginning of iteration k, using $IN^k = \begin{pmatrix} x^1 \\ \vdots \\ x^N \end{pmatrix}$, where $x^{1..N}$ is the vector of optimization variables $x^{1..N}$, IN^k – vector of initial conditions consists of the mean value for each optimization variable.
- Based on the permissible standard deviation $\begin{pmatrix} \sigma^1 \\ \vdots \\ \sigma^N \end{pmatrix}$, a matrix of input variables reads

$$M_{in}^k = \begin{bmatrix} x_{j=1}^{i=1} & \cdots & x_{j=\lambda}^{i=1} \\ \vdots & \vdots & \vdots \\ x_{j=1}^{i=N} & \cdots & x_{j=\lambda}^{i=N} \end{bmatrix},$$

[5.9]

  Where λ is the size of the population formed on iteration k, $x_j^i -$ manipulated variable value generated by the CMA-ES algorithm.
- Intra-cluster informational agreement of using each column of M_{in}^k as input parameter set for the processor unit PU computationally, obtaining a numerical solution applying the same instruction for each Process Unit.
- Sending vectors of resulted solutions after t_{end} from computed processors to the central processor.
- Intra-cluster search of f_{best} among solution space $f_{j=1..\lambda}$.
- A decision about starting conditions for $k+1$ iteration. The stopping criterion for the algorithm is the absence of improvement in f_{best} after k_{max} iterations.

The list of parameters necessary for solving the set optimization problems is given in Table 5.1.

Table 5.1 Parameters characterizing parallel computing

Number of the optimization variables	N
Size of the formed population	λ
Stopping criteria iteration number	k_{max}
Number of processors used	PU

In this work, efficient mechanisms of parallel computing are proposed to obtain numerical solutions while balancing the load between the nodes. Table 5.2 summarizes the computer server parameters used for parallel computations. In each core, evaluation took place independently without the need for information exchange to occur. Once the calculations on each of the physical cores were complete, the final assessment of the numerical solutions was conducted on the central processor. Parallel computing was done using Dell Inc. PowerEdge R930 server; related parameters are given in Table 5.2.

Table 5.2 Computer server parameters

Model	Intel(R) Xeon(R) CPU E7-8880 v4 @ 2.20GHz
Thread(s) per core:	2
Core(s) per socket	22
Socket(s):	4
Number of physical cores	88
Number of logical cores	176

5.5 Optimization results

5.5.1 Preliminary optimization of the operating parameters

After finding the reference solution and achieving the quantitative agreement between the simulation and experiment results, we return to sensitivity analysis to determine potential parameters for further optimization. It was confirmed earlier in (Gänsch et al., 2021) and in the extended sensitivity analysis (Chapter 4) that operating parameters such as inlet liquid concentration c_{in}^{i}, and inlet volume flow rate (V_{in}) play a significant role in the crystallization process. Since the fundamental driving force for crystallization is supersaturation, changes in the inlet liquid concentration (c_{in}) directly affect productivity. At the same time, the nucleation of the counter-enantiomer can never be fully prevented, and crystals of both enantiomers are formed. Product contamination can be avoided by applying the self-cleaning effect by providing an inlet flow rate at which fines will be washed out of the crystallizer. A high flow rate supports the removal of nuclei and increases purity, but on the other hand, it also washes out desired enantiomer crystals, thereby reducing yield (Mangold et al., 2021). In fact, there is a limit of the volumetric flow rate at which a sufficient number of crystals remain in the crystallizer, and their growth is ensured. In experiments, the liquid flow rate is usually kept below this limit to ensure process efficiency. Considering the importance of these phenomena, this section focuses on finding the conditions under which it will be possible to achieve a compromise between the high yield and desired solution purity.

Simulation conditions

Referring to the model-based process study, the photo-sensor must be placed in the maximum permissible position for achieving the highest productivity (Figure 4.5). The following process parameters characterizing the Reference case are used for simulation: thermodynamic compound properties (Table 1.2), crystallizer geometry parameters (Table 4.1, L-crystallizer), taking into account changes in the upper sensor position, h_s, parameters related to withdrawal strategy are listed in Table 5.3. The variables to be optimized are inlet liquid concentration (c_{in}^{i}) and inlet volume flow rate (V_{in}).

Table 5.3 Applied withdrawal strategy

Upper sensor position	h_S	0.95 $[m]$
Withdrawn segment	Δh_p	0.085 $[m]$

The bi-criterial optimization problem is converted to a single objective problem by introducing a Pareto coefficient (w) varying from 0 to 1. Process purity may be expressed as

$$\gamma_i = \frac{m_i}{m_i + m_j},$$

where $i = L - Asn \cdot H_2O, and\ j = D - Asn \cdot H_2O.$

[5.10]

The resulting combining objective function, OF_4, complements the list of objective functions investigated in Chapter 4 and reads

$$OF_4 \ = \ (1 - w) \cdot \gamma_i + w \cdot m_i$$

[5.11]

When using the coefficient w= 0, the purity of the desired enantiomer is maximized; when using the coefficient w =1, emphasis is on the yield. As an initial estimate for new points on the Pareto front, the maximum value of the objective function calculated in the previous step is used. To provide an initial sample, several iterations of the CMA-ES algorithm were performed.

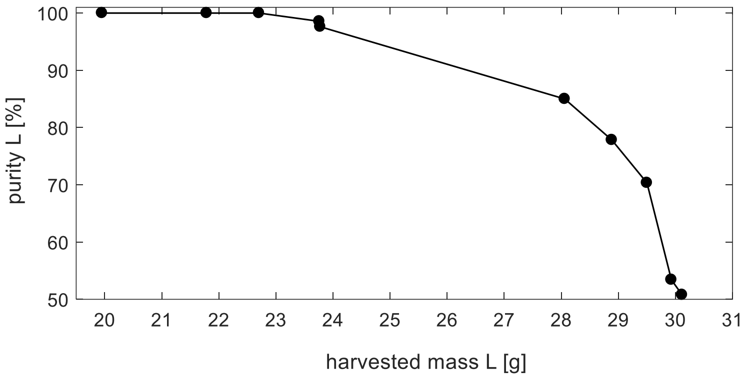

Figure 5.6 Pareto Front, obtained by using the CMA-ES algorithm. The number of individuals inside population λ=88 for the first iteration, λ=50 for subsequent iterations. Initial guesses for the inlet volume flow rate and the inlet liquid concentration were used from the Reference case (Table 4.3).

The provided study has demonstrated the potential to achieve high purity and harvested mass over the crystallization process. As a result of preliminary optimization of the operating parameters, suitable values for the inlet liquid concentration and the inlet volume flow rate were determined depending on the chosen Pareto coefficient. However, this study fully predicts product purity only when estimated nucleation kinetics is available, which is complicated in practice. To ensure high accuracy of model-based process optimization, the next section of this chapter is devoted to an alternative way of assessing product purity.

5.5.2 Model-based crystallization design

It is well known that chemicals are generally contaminated by different amounts of impurities from various sources. In the case of chiral compounds, contamination occurs when the target enantiomer cannot be isolated in its pure form. This means that the final crystallized product contains nuclei of the counter-enantiomer. Regardless of the chosen method for the separation, no technology can guarantee the absence of impurities. The process of purity reduction depends on many factors, and, more importantly, it is challenging to control during the reaction. It is most likely that a decrease in purity is detected when crystals are dried and separated from the suspension. Once the crystal is formed, washing procedures may be carried out to increase crystal purity by removing some of the surface impurities (Belviso, 2015). However, this technique is quite risky because the washing solvent should remove the contaminants without dissolving the desired crystals that are rather difficult due to the chirality of the components. This section presents an alternative approach to assess the purity of the product, considering experimental results in which contamination of the solution was detected. The optimization procedure focuses on finding the best operating and geometry parameters to achieve high productivity and avoid potential nucleation in the reactor.

The results of a crystallization experiment depend not only on the initial and final chemical and physical states of the mother liquor but also on the pathway by which the former is transformed into the latter. This, in turn, depends on the chosen technique, used apparatus, and, of course, the production plant's parameters. The provided sensitivity analysis of product characteristics to changes in geometry parameters was presented earlier in chapter 4 (Figure 4.10). The same objective function as described in chapter 4 is used for current optimization. However, to ensure the robustness of the process, specific constraints are discussed in this section. The main goal of optimizing production processes is to improve productivity of the target compound, which in general can be expressed as follows:

$$OF_1 = Pr^L \rightarrow max,$$

where L stays for $L - Asn$.

[5.12]

Design constraints

When designing a new crystallization tube, there are some limitations imposed by the manufacturing process that have to be taken into account:

$$H \leq 1.3\, m$$
$$H_1 \geq H_{prod}$$
$$H_{prod} + \Delta h_p < h_s$$

In addition, the values of $c_{in}^L = c_{in}^D = 0.0454\ kg_{solute} kg_{solution}^{-1}$ and $T_{saturation} = 35\ ℃$ must remain constant for the chosen chiral system. Based on this, the desired Temperature T_{des} at the middle of the crystallizer must satisfy the following condition:

$$300\ K \leq T_{des} \leq 305\ K$$

The subsection presents a novel approach for the crystallization process design by constructing efficient geometry and ensuring that its full potential is used. A single-objective constrained optimization technique is applied to find optimal conditions for crystallizer geometry, which is used as a set point for obtaining high productivity. Two well-studied crystallizer geometries have been simulated and used as case studies to validate the methodology proposed in this subsection. The process of cooling crystallization of asparagine monohydrate in different crystallizers is considered. The preliminary investigations of geometry influence are described in Chapter 4.

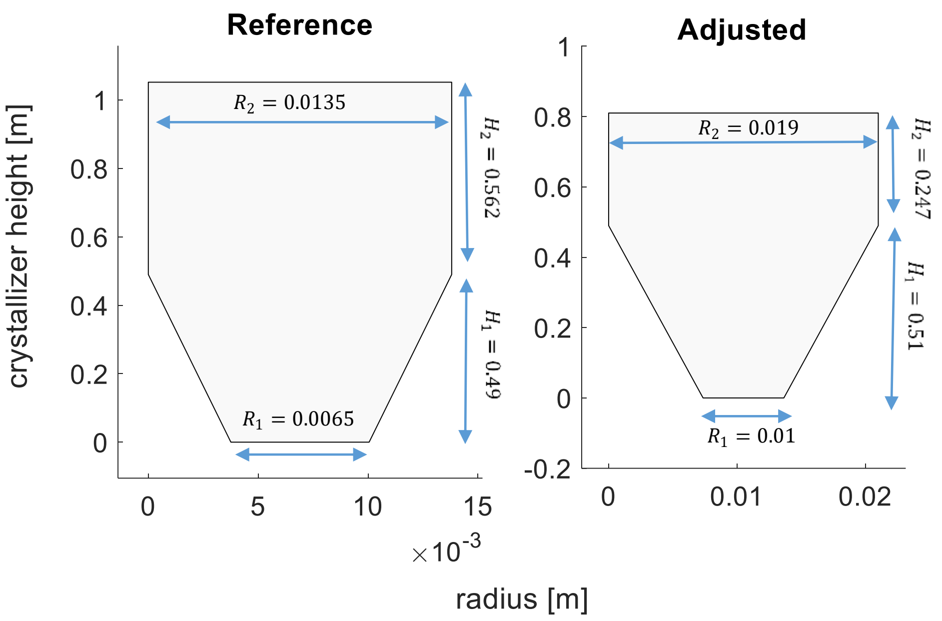

Figure 5.7 Schematic representations of the studied crystallizer geometries. To ensure the same residence time of crystals inside a reactor runs corresponding to different geometries are performed under different volumetric flow rates conditions. Runs corresponding to the Reference geometry are carried out at $\dot{V}_{in}$=12 lh^{-1}; for the Adjusted geometry, they are carried out at $\dot{V}_{in} = 25.6\ lh^{-1}$.

Empirical threshold to nucleation assessment

Numerical solutions obtained by simulating various withdrawal strategies for both geometries indicate the potential for increasing productivity by extending the bed height. As shown in Figure 5.7 and already outlined in Chapter 4, the use of shorter and broader geometry results in improved performance. However, while analyzing productivity, it should be noted that when the sensor is located in a high position, the risk of product contamination significantly increases, as it was experimentally proven and mentioned in previously published work (Gänsch et al., 2021). The decrease in product purity is observed while using the product withdrawal strategy 4 (Table 4.4). The occurrence of contamination can be explained by critical values of nucleation factors - supersaturation of the counter-enantiomer(S^D) and asymmetry of the solution ($asym^L$). From the experimental part, it is known that a low value of $asym^L$ accomplishes purity decrease as well as a high value of S^D. The asymmetry of the solution can be calculated from:

$$asym^L = \frac{c^L}{c^L + c^D}$$

[5.13]

Since the nuclei are formed in the upper part, it is essential to assess nucleation risk at the highest possible position, $h = H$. The maximum supersaturation value is reached when $h = H$. The lowest value of solution asymmetry can be detected at the same position. From now on, $S^D = S^D(H)$ and $asym^L = asym^L(H)$.

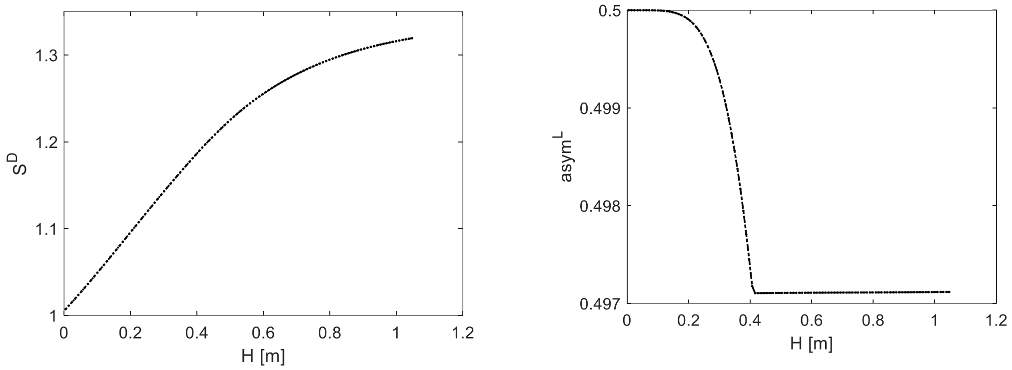

Figure 5.8 Simulated distributions of Supersaturation of the counter-enantiomer (S^D) over the crystallizer height (left), and solution asymmetry ($asym^L$), (right) related to the Reference case.

Considering the results of the experimental study, the following restrictions may be proposed:

$$S^D \leq 1.4$$
$$asym^L \geq 0.48$$

[5.14]

Two geometries are simulated using withdrawal strategies 3 and 4 (referring to Table 4.4). The corresponding data on productivity, bed height, solution asymmetry, and supersaturation of the counter-enantiomer are given in Table 5.4.

Table 5.4 Corresponding data on simulation results

Strategy	Geometry	Bed height, $h_s [cm]$	Productivity, $Pr^L\ [gl^{-1}h^{-1}]$	S^D	$asym^L$
4	Reference	63.5	112.59	1.33	0.471
3	Reference	43.5	80	1.3255	0.481
4	Adjusted	35.5	144	1.41	0.478
3	Adjusted	26.5	112	1.4	0.482

As shown in Table 5.4, lowering a fluidized bed eliminates the risks of nucleation. It moves the value of the nucleation factors to the permissible region (marked in green in figure 5.9 right).

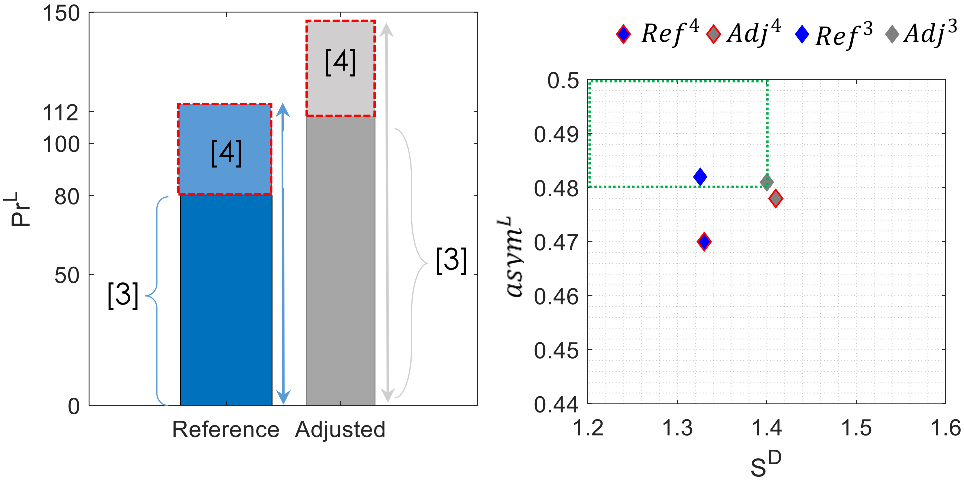

Figure 5.9 Simulation data on productivity (left) and nucleation factors (right) corresponding to the studied geometries – reference (Ref) and Adjusted (Adj). The red region in the left diagram is the difference in productivity between withdrawal strategies 3 (when the absence of nucleation is confirmed) and 4 (when the decrease in purity is detected). The green rectangle in the right diagram indicates the range of permissible values for the nucleation factors - supersaturation of the counter-enantiomer (S^D) and asymmetry of the solution ($asym^L$). The number of the simulated strategy is indicated by the index.

Although the proposed approach does not assess nucleation kinetics, it predicts the risk of nuclei present in the upper part of the reactor. On the one hand, crystallizer geometry allows the value of productivity to be significantly increased. On the other hand, detected nucleation risks will require lower bed height, resulting in less productivity. Ideally, the optimized parameter set for the crystallizer should be formed so that there are no nucleation risks detected. The photo-sensor can be placed in the highest possible position to permit the applicability of the withdrawn strategy with the most elevated bed. The crystallizer geometry is considered efficient as long as the above constraints and technical limitations are met. The list of optimization variables for model-based design is given in Table 5.5.

Table 5.5 List of optimization variables

x_1	H	Crystallizer height
x_2	H_1	Height of conical section
x_3	R_1	Radius of the bottom
x_4	R_2	Radius of the top
x_5	T_{cryst}	Crystallizer Temperature
x_6	$u_{empty\ tube}$	Empty tube velocity

Considering all of the above, [5.12] now reads

$$OF_1\left\{\begin{matrix} H \\ H_1 \\ R_1 \\ R_2 \\ T_{cryst} \\ u_{empty\ tube} \end{matrix}\right\} = Pr^L \to max \left| \begin{matrix} H \leq 1.3 \\ H_1 \geq h_{prod} \\ H_{prod} + \Delta h_p < h_s \\ S^D \leq 1.4 \\ asym^L \geq 0.48 \end{matrix}\right. \qquad [5.15]$$

To implement the product withdrawal strategy, the parameters H_{prod} and Δh_p with constant values are used. The location of the sensor position (h_s), responsible for the bed height is calculated based on the generated value of H, taking into account the withdrawn segment, $h_s = H - \Delta h_p$.

Table 5.6 Strategy parameters

Sensor position	h_s	$maximal\ possible (based\ on\ H)$
Outlet position	H_{prod}	$0.335\ [m]$
Withdrawal distance	Δh_p	$0.085\ [m]$

Optimization results

Combined with experiment results, model-based optimization is applied to provide an optimal apparatus's design and operation procedure for the cooling crystallization of asparagine monohydrate. Using the model, continuous operating systems can be designed to minimize nucleation factors and increase productivity.

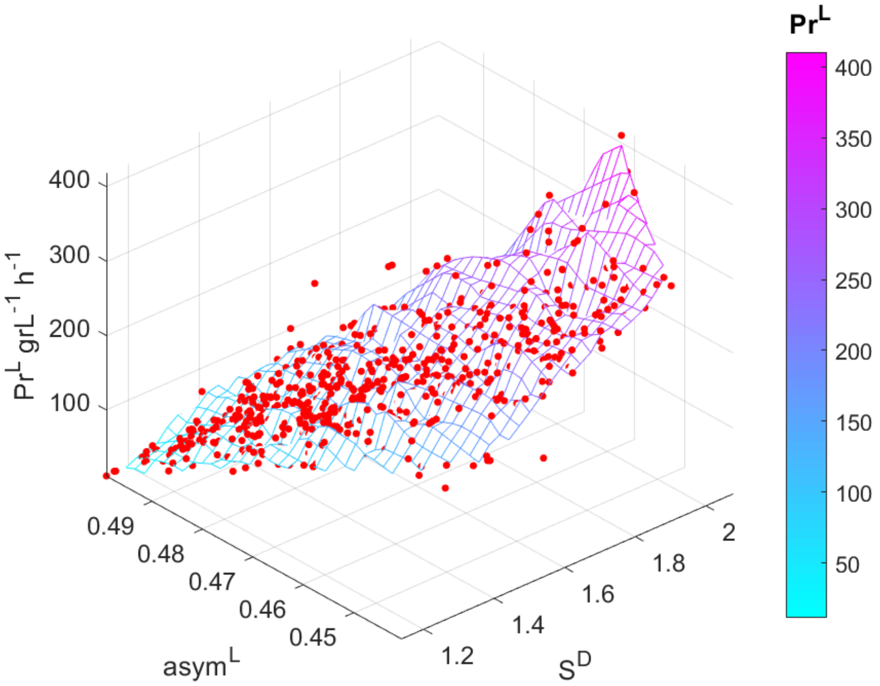

Figure 5.10 The results of the final optimization procedure applying the CMA-ES algorithm; obtained solution space consisting of 750 points representing the optimization round. The number of individuals inside the population, $\lambda = 50$. A linearized surface is used to visualize regions of the productivity values.

Using the CMA-ES algorithm, the optimal set of geometrical and operating parameters is determined by the objective function and constraints given in [5.15]. A comparison of all obtained numerical solutions is conducted to determine whether the optimal parameter set is superior. Figure 5.10 demonstrates values of simulated productivity and the corresponding nucleation factors. Interpolating linearly, productivity values are divided into classes and represented in a surface form. Figure 5.10 indicates that all the obtained values complying with the given optimization restrictions are located in the region with the lowest productivity values. High productivity is most likely to occur at the boundary between two classes.

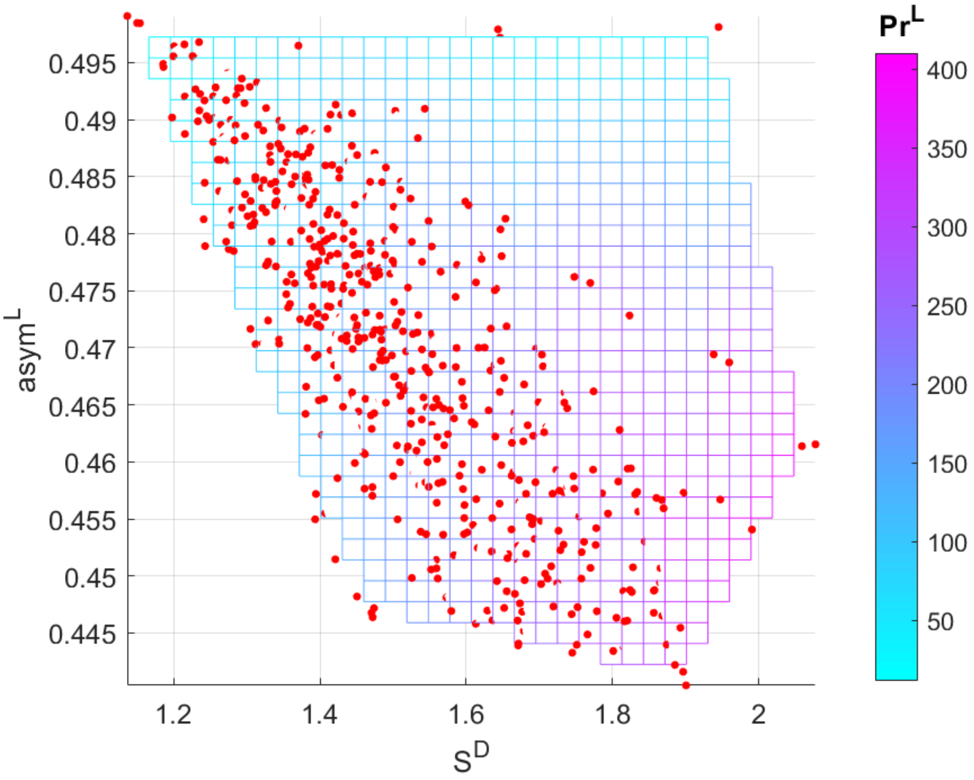

Figure 5.11 Simulation results obtained by using the CMA-ES algorithm. Provided solution space can be divided into classes based on productivity values. The class indicated by the blue grid represents low productivity values but satisfactory conditions in terms of model constraints. Gradient transition shows an increase in productivity in the direction of purple. The area of acceptable solutions characterizes by low productivity values, while the purple region contains values with predominantly high productivity but does not satisfy the optimization conditions.

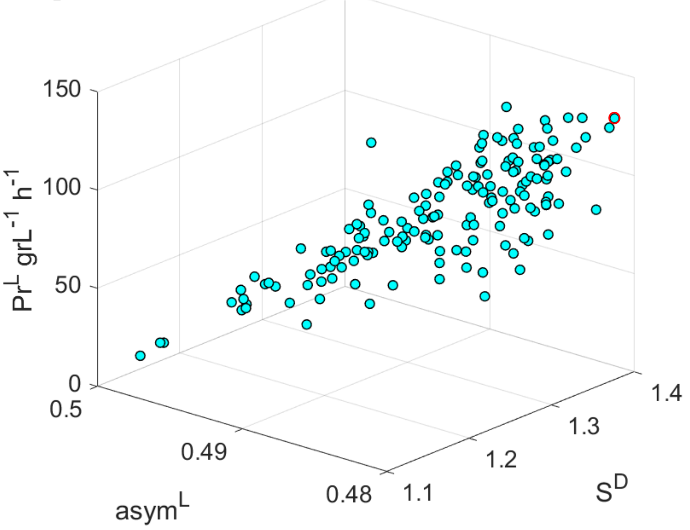

Figure 5.12 The results of the CMA-ES algorithm evaluation after 12 iterations; only points that meet optimization conditions are shown. The point with the higher productivity value is marked in red.

Numerical solutions that satisfy all the constraints are shown in figure 5.11. The maximum productivity achieved during the CMA-ES execution procedure is equal to $128.7\ gl^{-1}h^{-1}$, this value exceeds the productivity achieved earlier by applying withdrawal strategies 3 and 4. In Figure 5.12, it can be seen that two runs of the crystallizer simulated earlier result in the acceptable values of the nucleation factors, the same as assessment of the Optimized parameter set.

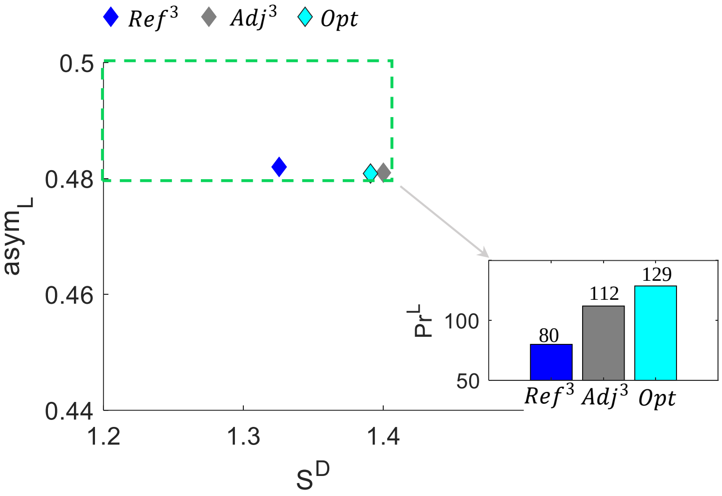

Figure 5.13 Comparative results of the three studied geometries where the values of productivity for the Reference and Adjusted geometries are used based on simulating withdrawal strategy 3, and the best point obtained while optimization procedure selected for the optimized geometry, Opt. The green rectangle defines the permissible space for nucleation factors.

The geometric parameters of the crystallizer obtained in mathematical optimization are shown in Figure 5.14. The corresponding operating parameters are summarized in Table 5.7. As a result of the obtained recommendations, the high productivity of the process can be achieved by designing a crystallizer with the listed parameters. As already suggested in (Mangold et al., 2016), the main requirement is to increase the crystallizer width (R_1 and R_2). Additionally, assumptions are made about the reduction of the cylindrical crystallizer column. Consequently, high productivity is achieved, and no product contamination is eliminated.

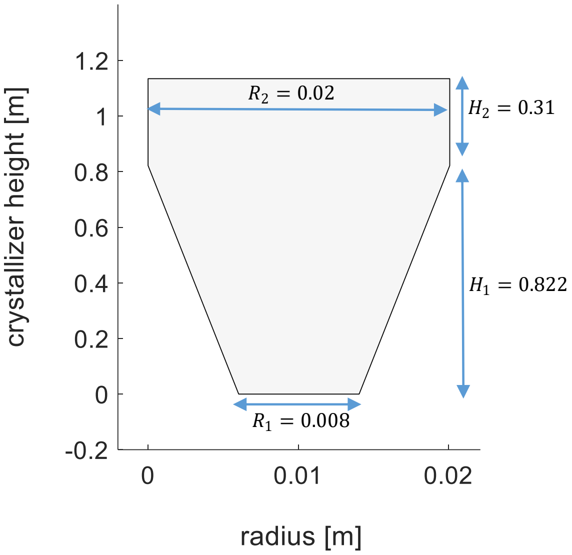

Figure 5.14 Scheme of the Optimized crystallizer geometry. Parameters obtained by mathematical optimization using the CMA-ES genetic algorithm.

Table 5.7 List of operating parameters based on the optimization results

Empty tube velocity of liquid phase	$u_{empty\ tube}$	$0.0083\ [ms^{-1}]$
Volumetric feed flow rate	$\dot{V}_{in}$	$37.44\ [lh^{-1}]$
Crystallizer temperature (middle position)	T_{cryst}	$303.84\ [K]$
Sensor position	h_s	$1.04\ [m]$

Following are the results demonstrating the influence of geometry and operation mode on the performance of the crystallization process concerning the productivity and purity of the product:

1. Simulation analysis of nucleation factors for the Reference geometry indicated a risk of potential product contamination, which was confirmed experimentally.
2. Using the information obtained on solution asymmetry and supersaturation limits, mathematical restrictions can be formulated to prevent product contamination during optimization.
3. The provided study found that the selection of parameters corresponding to the reactor geometry and operating mode permitted various productivity and purity changes.
4. Applied parallel computations significantly accelerated the process of obtaining numerical solutions.

5. Mathematical optimization has resulted in a 15% increase in productivity while maintaining the stability of the process and negating product contamination risks.

5.6 Summary of the model-based process optimization

A systematic model-based optimization approach is implemented to crystallize asparagine monohydrate in a fluidized bed reactor continuously. The steady-state optimization, considering imposed constraints, made it possible to design an efficient set of geometry and operating conditions based on the attainable regions. In addition, it was possible to identify the existing dependencies between the manipulated variables and nucleation factors that determine the applicability of one or another simulated geometry. The minimization of nucleation risks is a significant challenge in continuous pharmaceutical manufacturing. Safe regions of nucleation factors are discussed within this study to minimize such risks. Several control variables are adopted to enable a more effective optimization to address the dynamic optimization problem. Identification and comparison of optimal profiles for crystallization temperature, volumetric flow rate, and geometrical parameters are performed. It is demonstrated that the proposed optimal design of the crystallizer setup increases productivity, and additionally, it allows the evaluation of the nucleation factors once the proposed geometry is simulated.

6. Conclusions

The presented work is devoted to studying, modeling, and optimizing the enantioselective crystallization process. On the way to modeling, attention is paid to the theoretical description of the crystallization foundations, process variability, and the study of phase transition diagrams. In addition, an industry-relevant process of conversion from batch crystallization to continuous by applying fluidized bed modes is considered. Continuing the work of Daniel Binev (Binev, 2015), a coupled system consisting of two tubular crystallizers connected via a tank with a racemic mixture is described to ensure parallel crystallization of both enantiomers in each crystallizer.

The theoretical section discusses kinetic phenomena like primary nucleation and subsequent crystal growth. By introducing a crystal mill, the reactor is continuously seeded with crystalline material replacing the function of nucleation. Eventually, the large particles settle at the bottom, are crushed in the mill, and returned to the reactor for further growth. The applicability of a fluidized bed concept makes it possible to avoid the undesirable distribution of obtained crystals.

Modeling the crystallization process performed within this work is based on the concepts proposed by (Hulburt and Katz, 1964) and (Ramkrishna, 2000). Population balance equations describe the evolution of solid phases, allowing one to estimate crystal size distribution. The numerical solution of the balance equations allows one to draw conclusions about the evolution of the solid and liquid phases, the temperature variations, and the amount of time it takes for the system to reach a steady state under various operating conditions.

According to the research, the following results are achieved:

- The information available in the literature on the preferential crystallization of enantiomers is studied. The classification of approaches to separating racemic mixtures for the production of conglomerates is discussed, along with the variety of reactor setups for providing a saturated solution in continuous crystallization.
- A mathematical model that describes the process of preferential crystallization in a fluidized bed is developed. The proposed modeling environment is characterized by the thermodynamic and kinetic parameters of the system under study, the parameters of the crystallizer geometry, and the operating conditions. The use of the model allows making predictions about the main characteristics of the process, such as productivity or

theoretical yield and the size of the crystals. The main advantage of the developed model is distinguishing between the crystals of the target and counter-enantiomer, which is considered as a useful tool to assess the purity of the obtained conglomerate.

- To validate the model, the numerical solution is compared with the experimental results. A chemical system of asparagine monohydrate and water is selected for verification. Considering the potential efficiency of a fluidized bed concept, the choice of the chemical system can be explained by the density difference between the solvent and solid material. Model validation is performed by comparing the mean crystal size, productivity, and standard deviation of samples. Based on the agreement between simulations and experiments, the model proves to be a valuable tool.
- The choice of variables for model-based optimization is based on the performed local sensitivity analysis.
- Two approaches to optimizing the process are considered. Optimization of operating parameters such as inlet flow rate and initial liquid concentration is performed to assess the change in the purity of the product obtained. The presented Pareto front demonstrates a compromise between yield and product purity, achieved using various parameter combinations.
- The application part focuses on optimizing the crystallizer geometry and adjusting the operating mode to maximize productivity and ensure process robustness. The key idea behind the proposed approach relies on an empirical threshold to assess the likelihood of product contamination. The mathematical optimization performed using a genetic algorithm resulted in a 15% increase in productivity compared to the Reference case by determining the geometrical and operational parameters. Moreover, the provided optimization procedure ensures the stability of the process and, more important, the absence of product contamination.

References

(Aamir et al., 2010)	Aamir, E., Nagy, Z.K., Rielly, C., 2010. Optimal seed recipe design for crystal size distribution control for batch cooling crystallisation processes. Chem. Eng. Sci. 65, 3602-3614.
(Ager, 2005)	Ager, D., 2005. Handbook of Chiral Chemicals (2nd ed.). CRC Press, Boca Raton.
(Ahuja, 1998)	Ahuja, S., 1998. Chiral Separations, Applications and Technology. J. Liq. Chromatogr. Relat. Technol. 21, 1076-1078.
(Alvarez and Myerson, 2010)	Alvarez, A., Myerson, A., 2010. Continuous plug flow crystallization of pharmaceutical compounds. Cryst. Growth Des. 10, 2219–2228.
(Anderson et al., 2020)	Anderson, J., Gillen, K., Wright, J., Adams, C., Hughes, I., 2020. Optical rotation of white light. Am. J. Phys. 88(247).
(Anderson, 2001)	Anderson, N.G., 2001. Practical Use of Continuous Processing in Developing and Scaling Up Laboratory Processes. Org. Process Res. 5, 613-621.
(Annales de chimie, 1806)	Annales de chimie et de physique. Ser. 1,v. 57-58, 1806-07.
(Annales de chimie, 1809)	Annales de chimie et de physique. Ser.1 v. 72, 1809.
(Ariëns, 1984)	Ariëns, E.J., 1984. Stereochemistry, a basis for sophisticated nonsense in pharmacokinetics and clinical pharmacology. Eur. J. Clin. Pharmacol. 26, 663–668.
(Asimov, 1994)	Nicol prism. (n.d.) >The Free Library. (2014). Retrieved Dec 29 2021 from https://www.thefreelibrary.com/Nicol+prism.-a017279126
(Batchelor, 2000)	Batchelor, G. K., 2000. An Introduction to Fluid Dynamics. Cambridge University Press, Cambridge.
(Belviso, 2015)	Belviso, B.D., 2015. Crystal Purity. Encyclopedia of Membranes. Springer, Berlin, Heidelberg.
(Binev et al., 2016)	Binev, D., Seidel-Morgenstern, A., Lorenz, H., 2016. Continuous Separation of Isomers in Fluidized Bed Crystallizers. Cryst. Growth Des. 16 (3), 1409-1419.
(Binev, 2015)	Binev, D., 2015. Continuous fluidized bed crystallization. Ph.D. thesis. Otto vonGuericke University, Magdeburg.
(Boros et al., 2016)	Boros, A., Majumder, A., Nagy, Z.K., 2016. Multi-Impurity Adsorption Model for Modeling Crystal Purity and Shape Evolution during Crystallization Processes in Impure Media. Cryst. Growth Des.16 (2), 555-568.
(Brown et al., 2020)	Brown, C., Maldonado, D., Vassileiou, A., Johnston, B., Florence, A., 2020. Data Mining Crystallization Kinetics. ChemRxiv. Cambridge: Cambridge Open Engage.
(Bück, 2012)	Bück, A. 2012. Model-based measurement and control of fluidised bed spray granulation processes. Ph.D. thesis. Otto vonGuericke University, Magdeburg.
(Burcham and Jarmer, 2013)	Burcham, C., Jarmer, D., 2013. Industrial Crystallization of Pharmaceuticals: Capability Requirements to Support an Outsourcing Paradigm. Pharm. 14.
(Büskens and Maurer, 2001)	Büskens C., Maurer H., 2001. Sensitivity Analysis and Real-Time Optimization of Parametric Nonlinear Programming Problems. In: Grötschel M., Krumke S.O., Rambau J. (eds) Online Optimization of Large Scale Systems. Springer, Berlin, Heidelberg.

(Cascella, 2021)	Cascella, F., 2021. Resolution of enantiomers of chiral compounds using crystallization processes: from fundamental studies to process development. Ph.D. thesis. Otto vonGuericke University, Magdeburg.
(Chhabra et al., 2013)	Chhabra, N., Aseri, M.L., Padmanabhan, D., 2013. A review of drug isomerism and its significance. Int. J. Appl. Basic Med. Res. 3(1), 16-18.
(Coutts and Baker, 1989)	Coutts, R.T., Baker, G.B., 1989. Implications of chirality and geometric isomerism in some psychoactive drugs and their metabolites. Chirality 1, 99-120.
(Cundall and Strack, 1979)	Cundall, P.A., Strack, O.D.L., 1979. A discrete numerical model for granular assemblies. Géotechnique 29(1), 47-65.
(Dang et al., 2019)	Dang, V.H., Vien, N.A., Chung, T. A., 2019. Covariance matrix adaptation evolution strategy in reproducing kernel Hilbert space. Genet. Program. Evolvable Mach. 20, 479–501.
(Dauphin et al., 2014)	Dauphin, Y.N., Pascanu, R., Gulcehre, C., Cho, K., Ganguli, S., Bengio, Y., 2014. Identifying and attacking the saddle point problem in high-dimensional non-convex optimization. 27th International Conference on Neural Information Processing Systems. MIT Press, Cambridge, MA, 2933-2941.
(Dengale et al., 2016)	Dengale, S.J., Grohganz, H., Rades, T., Löbmann, K., 2016. Recent advances in co-amorphous drug formulations. Adv. Drug Delivery Rev. 100,116-125.
(Deore et al., 2019)	Deore, A., Dhumane, J., Wagh, R., & Sonawane, R., 2019. The Stages of Drug Discovery and Development Process. Asian J. Pharm. Res. Dev. 7(6), 62-67.
(Desikan et al., 2000)	Desikan, S., Anderson, S.R., Meenan, P.A., Toma, P.H., 2000. Crystallization challenges in drug development: scale-up from laboratory to pilot plant and beyond. Curr. Opin. Drug Discovery Dev. 3(6), 723-33.
(Diemer et al., 2005)	Diemer, R., Spahr, D., Olson, J., Magan, R., 2005. Interpretation of size reduction data via moment models. Powder Technol. 156, 83–94.
(Eichelbaum, 1995)	Eichelbaum M., 1995. Side effects and toxic reactions of chiral drugs: A clinical perspective. In: Degen G.H., Seiler J.P., Bentley P. (eds) Toxicology in Transition. Archives of Toxicology 17. Springer, Berlin, Heidelberg.
(Elsner et al., 2011)	Elsner, M. P., Ziomek, G., Seidel-Morgenstern, A., 2011. Simultaneous preferential crystallization in a coupled batch operation mode. Part II: Experimental study and model refinement. Chem. Eng. Sci. 66(6), 1269-1284.
(Eslahpazir et al., 2011)	Eslahpazir, M., Wittmann, C., Krull, R., 2011. Computational Fluid Dynamics. Comprehensive Biotechnology. Academic Press, New York.
(Eymard et al., 2000)	Eymard, R., Gallouët, T., Herbin, R., 2000. Finite volume methods. Handbook of Numerical Analysis, Elsevier 7, 713-1018.
(Fayzullin et al., 2014)	Fayzullin, R.R., Lorenz, H., Bredikhina, Z.A., Bredikhin, A.A. Seidel-Morgenstern, A., 2014. Solubility and Some Crystallization Properties of Conglomerate Forming Chiral Drug Guaifenesin in Water. J. Pharm. Sci. 103, 3176-3182.
(Franks et al., 2004)	Franks, M.E., Macpherson, G.R., Figg, W., 2004. Thalidomide. Lancet 363, 1802-1811.
(Frenkel, 1924)	Frenkel, J., 1924. Theorie der Adsorption und verwandter Erscheinungen. Physik 26, 117–138.

(Fujiwara et al., 2005)	Fujiwara, M., Nagy, Z.K., Chew, J.W., Braatz, R.D., 2005. First-principles and direct design approaches for the control of pharmaceutical crystallization. J. Process Control 15(5), 493-504.
(Gal, 2012)	Gal, J., 2012. The Discovery of Stereoselectivity at Biological Receptors: Arnaldo Piutti and the Taste of the Asparagine Enantiomers—History and Analysis on the 125th Anniversary, Chirality.
(Gal, 2019)	Gal, J., 2019. Louis Pasteur, Chemical Linguist: Founding the Language of Stereochemistry. Helv. Chim. 102,8.
(Gänsch et al., 2021)	Gänsch, J., Huskova, N., Kerst, K., Temmel, E., Lorenz, H., Mangold, M., Janiga, G., Seidel-Morgenstern, A., 2021. Continuous enantioselective crystallization of chiral compounds in coupled fluidized beds. Chem. Eng. J. 422.
(Gänsch, 2017)	Gänsch, J. 2017. Continuous fluidized bed crystallization. Master's thesis. Otto von Guericke University, Magdeburg.
(García et al., 1989)	García, C.E., Prett, D.M., Morari, M., 1989. Model predictive control: Theory and practice—A survey. Automatica (Oxf) 25, 335-348.
(Geller et al., 1996)	Геллер Б.Э., Геллер А.А., Чиртулов В.Г., 1996. Практическое руководство по физикохимии волокнообразующих полимеров. Химия, Москва.
(Ghosh and Fischer, 2006)	Ghosh, A., Fischer, P., 2006. Chiral Molecules Split Light: Reflection and Refraction in a Chiral Liquid. Phys. Rev. Lett. 97.
(Gibbs, 1873)	Gibbs, J. W., 1873. A Method of Geometrical Representation of the Thermodynamic Properties of Substances by Means of Surfaces. Trans. Conn. Acad. Arts Sci. 2, 382–404.
(Gibilaro, 2001)	Gibilaro, L., 2001. Fluidization-Dynamics: the Formulation and Applications of A Predictive Theory for the Fluidized State. Butterworth-Heinemann, Oxford.
(Gillespie, 2007)	Gillespie, D.T., 2007. Stochastic Simulation of Chemical Kinetics. nnu. Rev. Phys. Chem. 58, 35-55.
(Griffin et al., 2015)	Griffin, D., Grover, M., Kawajiri, Y., Rousseau, R., 2015. Mass-Count Plots for Crystal Size Control. Chem. Eng. Sci. 137, 338-351.
(Hager and Wellein, 2011)	Hager, G., Wellein, G., 2011. Introduction to High Performance Computing for Scientists and Engineers. CRC Press, Boca Raton.
(Han, 1969)	Han, C.D., 1969. A Control Study of Isothermal Mixed Crystallizers. Ind. Eng. Chem. Process 8, 150-158.
(Hansen, 2006)	Hansen, N., 2006. The CMA Evolution Strategy: A Comparing Review. StudFuzz 192, 75–102.
(Herfurth et al., 2016)	Herfurth, J., Mahnken, K., Fabian, J. Ulrich, J., 2016. Crystalline Layer Formation of Highly Viscous Supersaturated Liquids. Chem. Eng. Technol. 39, 1219-1223.
(Hill and Marty, 2008)	Hill, M.D., Marty, M.R., 2008. Amdahl's Law in the Multicore Era. Computer 41, 33-38.
(Hill and Ng, 1996)	Hill, P.J. Ng, K.M., 1996. Statistics of multiple particle breakage. AIChE J. 42, 1600-1611.
(Hu et al., 2005)	Hu, Q., Rohani, S., Jutan. A., 2005. Modelling and optimization of seeded batch crystallizers. Comput. Chem. Eng. 4, 911-918.

(Hulburt and Katz, 1964)	Hulburt, H.M., Katz, S., 1964. Some problems in particle technology: A statistical mechanical formulation. Chem. Eng. Sci. 19, 555-574.
(Huskova et al., 2021)	Huskova, N., Mangold, M., Seidel-Morgenstern, A., 2021. Optimization of a Continuous Fluidized Bed Process for the Separation of Enantiomers by Preferential Crystallization. Comput. Aided Process Eng. 50, 381-386.
(Hütter et al., 2005)	Huetter, M., Rutledge, G.C., Armstrong, R.C., 2005. Crystal shapes and crystallization in continuum modeling, Phys. Fluids 17.
(Hwang et al., 1979)	Hwang, C.L., Syed, A., Masud, M.D., 1979. Multiple Objective Decision Making — Methods and Applications. Springer, Berlin, Heidelberg.
(Igarashi and Ooshima, 2020)	Igarashi, K., Ooshima, 2020. Advances in Organic Crystal Chemistry. Springer , Singapore.
(Jagota et al., 2013)	Jagota, V., Sethi, A., Kumar, D.K., 2013. Finite Element Method: An Overview. Walailak J. Sci. & Tech. 10, 1-8.
(Janse, 1974)	Janse, A.H. 1974. Nucleation and crystal growth in batch crystallizers. Ph.D.thesis, TU Delft, Delft.
(Jaques et al., 1981)	Jaques, J., Collet, A., Wilen, S.H., 1981. Enantiomers, Racemates, and Resolutions. J. Wiley & Sons, Inc., New York.
(Jha et al, 2017)	Jha, S.K., Karthika, S., Radhakrishnan, T.K., 2017. Modelling and control of crystallization process. Res. Eff. Tech. 3, 94-100.
(Jiang and Braatz, 2019)	Jiang, M., Braatz, R.D., 2019. Designs of continuous-flow pharmaceutical crystallizers: developments and practice. CrystEngComm. 21, 3534-3551.
(Jones, 2002)	Jones, A.G., 2002. Crystallization Process Systems. Butterworth-Heinemann, Oxford.
(Kantorovich and Akilov, 1982)	Kantorovich, L. V., Akilov, G. P., 1982. Functional Analysis. Pergamon Press, New York.
(Karpiński and Bałdyga, 2019)	Karpiński, P.H., Bałdyga, J., 2019. Handbook of Industrial Crystallization, Chapter 12: Batch Crystallization. Cambridge University Press, Cambridge.
(Kim et al., 2009)	Kim, D. Y., Paul, M., Rapke, J. U., Wozny, G., Yang, D. R., 2009. Modelling of crystallization process and optimization of the cooling strategy. Korean J.Chem.Eng. 26, 1220-1225.
(Köhler et al., 2001)	Köhler, R., Mohl, K., Schramm, H., Zeitz, M., Kienle, A., Mangold, M., Stein, E., Gilles, E., 2001. Method of Lines within the Simulation Environment DIVA for Chemical Processes. Adaptive Method of Lines, 371-406.
(Köllges and Vetter, 2018)	Köllges, T., Vetter, T., 2018. Design and Performance Assessment of Continuous Crystallization Processes Resolving Racemic Conglomerates. Cryst. Growth Des. 18, 1686-1696.
(Kunii and Levenspiel, 1991)	Kunii, D., Levenspiel, O., 1991. Fluidization Engineering. Butterworth-Heinemann, Oxford.
(L'vov and Umantsev, 2021)	L'vov, P.E., Umantsev, A.R., 2021. Two-Step Mechanism of Macromolecular Nucleation and Crystallization: Field Theory and Simulations. Cryst. Growth Des. 21, 366-382.
(Lakerveld and Benyahia, 2020)	Lakerveld, R., Benyahia, B., 2020. Chapter 4 Process Control. In The Handbook of Continuous Crystallization, The Royal Society of Chemistry, London, 172-218.

(Li et al., 2016)	Li, R., Zhang, X., Dong, H., Li, Q., Shuai, Z. and Hu, W., 2016. Gibbs–Curie–Wulff Theorem in Organic Materials: A Case Study on the Relationship between Surface Energy and Crystal Growth. Adv. Mater. 28, 1697-1702.
(Lim et al., 2010)	Lim, C.K., Bhushan, R., Martens, J., 2010. Amino Acids: Chromatographic Separation and Enantioresolution. Biomed. Chromatogr. 24, 1029-1029.
(Liu, 2021)	Liu, X., 2021. Organic chemistry. Kwantlen Polytechnic University Press, Surrey, British Columbia.
(Lorenz and Seidel-Morgenstern, 2014)	Lorenz, H., Seidel-Morgenstern, A., 2014. Processes To Separate Enantiomers. Angew. Chem., Int. Ed. 53, 1218-1250.
(Louie, 2019)	Louie, A., Louie, J., 2019. Case Report: Retinal Toxicity Secondary to Ritonavir. Optom. Vis. Sci. 96, 376-381.
(Majumder and Nagy, 2013)	Majumder, A., Nagy, Z.K., 2013. Fines removal in a continuous plug flow crystallizer by optimal spatial temperature profiles with controlled dissolution. AIChE J. 59, 4582-4594.
(Mandelkern, 2016)	Mandelkern, L., 2016. Crystallization of Polymers: Kinetics and Mechanisms. Cambridge University Press, Cambridge.
(Mangold et al., 2015)	Mangold, M., Feng, L., Khlopov, D., Palis, S., Benner, P., Binev, D., Seidel-Morgenstern A., 2015. Nonlinear model reduction of a continuous fluidized bed crystallizer. J. Comput. Appl. Math. 289, 253–266.
(Mangold et al., 2016)	Mangold, M., Khlopov, D., Temmel, E., Lorenz, H., Seidel-Morgenstern, A., 2016. Modelling Geometrical and Fluid-Dynamic Aspects of a Continuous Fluidized Bed Crystallizer for Separation of Enantiomers. Chem. Eng. Sci. 160, 281-290.
(Mangold et al., 2021)	Mangold, M., Huskova, N., Gänsch, J., Seidel-Morgenstern, A., 2021. Linear Analysis of a Continuous Crystallization Process for Enantiomer Separation. Processes 8(11): 1337.
(Marchisio and Fox, 2005)	Marchisio, D.L., Fox, R.O., 2005. Solution of population balance equations using the direct quadrature method of moments. J. Aerosol Sci. 36, 43-73.
(MathWorks, 2016)	MATLAB, The MathWorks Inc. Natick, Massachusetts, United States; [9.1.0.960167], Version 2016b.
(Mazzotti et al., 2018)	Mazzotti, M., Vetter, T., Ochsenbein, D., 2018. Chapter 10: Crystallization Process Modeling in Polymorphism in the Pharmaceutical Industry: Solid Form and Drug Development, Wiley-VCH Verlag, Weinheim.
(McConathy and Owens, 2003)	McConathy, J., Owens, M., 2003. Stereochemistry in Drug Action. J. Clin. Psychiatry 2, 70-73.
(Meierhenrich, 2008)	Meierhenrich, U., 2008. When Crystals Deliver Chirality to Life. In: Amino Acids and the Asymmetry of Life. Advances in Astrobiology and Biogeophysics. Springer, Berlin, Heidelberg.
(Meisler, 2014)	Meisler, K.T., 2014. Multi-dimensional population balance models of crystallization processes. Ph.D. thesis. Technical University of Denmark, Copenhagen.
(Mersmann and Bartosch, 1998)	Mersmann, A., Bartosch, K., 1998. How to predict the metastable zone width. J. Cryst. Growth 183, 240-250.
(Mersmann, 2001)	Mersmann, A., 2001. Crystallization Technology Handbook. Taylor & Francis Inc, Abingdon.
(Mesbah et al., 2010)	Mesbah, A., Landlust, J., Huesman, A., Kramer, H., Jansens, P.J., Van den Hof, P.M.J., 2010. A model-based control

	framework for industrial batch crystallization processes. Chem. Eng. Res. Des. 88(9), 1223-1233.
(Midler, 1975)	Midler, M., 1975. Process for production of crystals in fluidized bed crystallizers. U. S. Pat., 3892539.
(Midler, 1976)	Midler, M., 1976. Crystallization system and method using crystal fracturing external to a crystallization column. U. S. Pat., 3996018.
(Miers and Isaac, 1907)	Miers, H., Isaac, F., 1907. The spontaneous crystallisation of binary mixtures. Experiments on Salol and Betol. R. Soc. Lond. 79, 322–351.
(Missirlis and Tjaferis, 1995)	Missirlis, N.M., Tjaferis, F.I, 1995. Parallel block methods for solving linear systems. Paral. Alg. Appl. 5, 57-68.
(Moore et al., 2021)	Moore, J.S., Wendorff, T., Hahn, A., 2021. Stereoisomerism and Smell. Chemical Education Digital Library (ChemEd DL).
(Moreno and Soriano-García, 1999)	Moreno, A., Soriano-García, M., 1999. Crystal-growth kinetics of protein single crystals along capillary tubes in the gel-acupuncture technique. Acta Crystallogr., Sect. D: Biol Crystallogr. 55(2), 577-80.
(Mullin, 2001)	Mullin, J.W., 2001. Crystallisation, 4th Edition, Butterworth Heinemann, Oxford.
(Murakami, 2007)	Murakami H., 2007. From Racemates to Single Enantiomers - Chiral Synthetic Drugs over the last 20 Years. Top.Curr.Chem. 269, 273-99.
(Myerson, 2002)	Myerson, A., 2002. Handbook of Industrial Crystallization 2nd Edition. Butterworth-Heinemann, Boston.
(Nagy and Agachi, 1997)	Nagy, Z., Agachi, S., 1997. Model predictive control of a PVC batch reactor. Comp. Chem. Eng. 21(6), 571-591.
(Nagy and Braatz, 2003)	Nagy, Z.K., Braatz, R.D., 2003. Robust nonlinear model predictive control of batch processes. AIChE J. 93(7), 1776-1786.
(Nagy and Braatz, 2012)	Nagy, Z.K., Braatz, R.D., 2012. Advances and New Directions in Crystallization Control. Annu. Rev. Chem. Biomol. Eng. 3(1), 55-75.
(Nagy et al., 2011)	Nagy, Z.K., Aamir, E., Rielly, C.D., 2011. Internal Fines Removal Using Population Balance Model Based Control of Crystal Size Distribution under Dissolution, Growth and Nucleation Mechanisms. Cryst. Growth Des. 11 (6), 2205-2219.
(Nagy et al., 2019)	Nagy, Z.K., Fujiwara, M., Braatz, R. D., 2019. Monitoring and Advanced Control of Crystallization Processes. In A. Myerson, D. Erdemir, & A. Lee (Eds.), Handbook of Industrial Crystallization. Cambridge University Press, Cambridge, 313-345.
(Nilsen et al., 2007)	Nilsen, O., Mohn, C.E., Kjekshus, A., Fjellvåg, H., 2007. Analytical model for island growth in atomic layer deposition using geometrical principles. J. Appl. Phys. 102, 024906.
(Nizhegorodova et al., 2015)	Nizhegorodova, Y., Belov, N., Berezkin, V., Yampol'skii, Y., 2015. Determination of solubility coefficients and sorption isotherms of gases in polymers by means of isothermal desorption with a chromatographic detection. Russ. J. Phys. Chem. 89, 502-509.
(Nývlt, 1985)	Nývlt, J., 1985. The Kinetics of Industrial Crystallization. Elsevier Science Ltd.

(Orehek et al., 2012)	Orehek, J., Teslić, D., Likozar, B., 2012. Continuous Crystallization Processes in Pharmaceutical Manufacturing: A Review. Org. Process Res. Dev. 25 (1), 16-42.
(Ostwald, 1897)	Ostwald, W., 1897. Studien über die Bildung und Umwandlung fester Körper
(Palis et al., 2013)	Palis, S., Binev, D., Lorenz, H., Seidel-Morgenstern, A., Kienle, A., 2013. Population balance modeling of crystallization in a fluidized bed. Proceedings on BIWIC 2013 20th International Workshop on Industrial Crystallization, 252-259.
(Paroli, 2012)	Paroli, F., 2012. Industrial Crystallizers Design and Control. In Industrial Crystallization Process Monitoring and Control (eds A. Chianese and H.J.M. Kramer).
(Petroianu, 2010)	Petroianu, G. A., 2010. History of organophosphate synthesis: the very early. Int. J. Pharm. Res. 65, 306-311.
(Petrusevska-Seebach, 2012)	Petrusevska-Seebach, K. 2012. Overcoming Yield Limitations When Resolving Racemates by Combination of Crystallization and/or Chromatography with Racemization. Ph. D. thesis. Otto von Guericke University, Magdeburg.
(Priambodo et al., 2017)	Priambodo, R., Shih, Y.-J., Huang, Y.-H., 2017. Phosphorus recovery as ferrous phosphate (vivianite) from wastewater produced in manufacture of thin film transistor-liquid crystal displays (TFT-LCD) by a fluidized bed crystallizer (FBC). RSC Adv. 7, 40819-40828.
(Qamar et al., 2013)	Qamar, S., Galan, K., Elsner, M.P., Hussain, I., Seidel-Morgenstern, A., 2013. Theoretical investigation of simultaneous continuous preferential crystallization in a coupled mode. Chem. Eng. Sci. 98, 25-39.
(Ramkrishna, 2000)	Ramkrishna, D. 2000. Population Balances: Theory and Applications to Particulate Systems in Engineering. Academic Press, San Diego.
(Randolph and Larson, 1988)	Randolph, A.D., Larson, M.A., 1988. Theory of Particulate Processes. Academic Press, New York.
(Reichelt and Shampine, 2017)	Reichelt, M.W., Shampine, L.F., 1984-2017. The MathWorks, Inc.
(Reynolds, 2010)	Reynolds, G., 2010. Modelling of pharmaceutical granule size reduction in a conical screen mill. Chem. Eng. J. 164, 383-392.
(Richardson and Zaki, 1954)	Richardson, J.F. , Zaki, W.N., 1954. The sedimentation of a suspension of uniform spheres under conditions of viscous flow. Chem. Eng. Sci. 3(2), 65-73.
(Ridder et al., 2016)	Ridder, B.J., Majumder, A., Nagy, Z. K., 2016. Parametric, Optimization-Based Study on the Feasibility of a Multisegment Antisolvent Crystallizer for in Situ Fines Removal and Matching of Target Size Distribution. Ind. Eng. Chem. Res. 55 (8), 2371-2380.
(Rougeot and Hein, 2015)	Rougeot, C., Hein, J.E., 2015. Application of Continuous Preferential Crystallization to Efficiently Access Enantiopure Chemicals. Org. Process Res. Dev. 19 (12), 1809-1819.
(Sakurai, 2005)	Sakurai, H., Funakoshi, S., Adachi, Y., 2005. New developments of insulinomimetic dinuclear vanadyl(IV)-tartrate complexes. Pure Appl. Chem. 77(9), 1629-1640.
(Salvatori and Mazzotti, 2017)	Salvatori, F., Mazzotti, M., 2017. Manipulation of Particle Morphology by Crystallization, Milling, and Heating Cycles—A Mathematical Modeling Approach. Ind. Eng. Chem. Res. 56 (32), 9188-9201.

(Schliemann et al., 2011)	Schliemann, M., Bullinger, E., Borchers, S., Allg ower, F., Scheurich, P., 2011. Heterogeneity reduces sensitivity of cell death for TNF-Stimuli. BMC Systems Biology 5.
(Schmelzer and Abyzov, 2017)	Schmelzer, J., Abyzov, A., 2017. How Do Crystals Nucleate and Grow: Ostwald's Rule of Stages and Beyond. Thermal Physics and Thermal Analysis. Springer, Heidelberg.
(Schöll et al., 2007)	Schöll, J., Lindenberg, C., Vicum, L., Broziob, J., Mazzotti, M., 2007. Precipitation of α l-glutamic acid: determination of growth kinetics, Faraday Discuss. 136, 247-264.
(Scott and Mercer, 1997)	Scott, A., Mercer, E.I., 1997. Concise Encyclopedia: Biochemistry and Molecular Biology, Walter de Gruyter, Inc., New York.
(Shih et al., 2017)	Shih Y.J., Ruffel, R., Abarca, M., G. de Luna, M.D., Huang, Y.-H., Lu, M.C., 2017. Recovery of phosphorus from synthetic wastewaters by struvite crystallization in a fluidized-bed reactor: Effects of pH, phosphate concentration and coexisting ions. Chemosphere 173, 466-473.
(Singh et al., 2010)	Singh, R., Gernaey, K., Gani, R., 2010. An ontological knowledge-based system for the selection of process monitoring and analysis tools. Comput. Chem. Eng. 34, 1137-1154.
(Speirs, 1962)	Speirs, A., 1962. Thalidomide and congenital abnormalities. Lancet 279 (7224), 303-305.
(Stranski and Krastanow, 1938)	Stranski, I. N., Krastanow, L., 1938. Zur Theorie der orientierten Ausscheidung von Ionenkristallen aufeinander. Abhandlungen der Mathematisch-Naturwissenschaftlichen Klasse IIb. Akademie der Wissenschaften Wien. 146, 797–810.
(Stynes, 2007)	Stynes, M., 2007. Numerical Treatment of Partial Differential Equations, Springer, Berlin, Heidelberg.
(Sudholt, 2015)	Sudholt, D., 2015. Parallel Evolutionary Algorithms. Springer Handbook of Computational Intelligence. Springer, Berlin, Heidelberg.
(Syrris Blog, 2021)	Syrris Blog [https://www.syrris.com/applications/what-is-crystallization-and-what-are-the-methods-of-crystallization/]
(Tavare, 1995)	Tavare, N.S., 1995. Crystallization Kinetics. In: Industrial Crystallization. The Springer Chemical Engineering Series. Springer, Boston, MA.
(Temmel and Lorenz, 2020)	Temmel, E., Lorenz, H., 2020. Advances in Industrial Crystallization. Crystals 10, 997.
(Temmel et al., 2018)	Temmel, E., Gänsch, J., Lorenz, H., Seidel-Morgenstern, A., 2018. Measurement and Evaluation of the Crystallization Kinetics of l-Asparagine Monohydrate in the Ternary l-/d-Asparagine/Water System. Cryst. Growth Des.18 (12), 7504-7517.
(Tokunaga et al., 2018)	Tokunaga, E., Yamamoto, T., Ito, E., 2018. Understanding the Thalidomide Chirality in Biological Processes by the Self-disproportionation of Enantiomers. Sci. Rep. 8, 17131.
(Tóth et al., 2012)	Tóth, G., Tegze, G., Pusztai, T., Gránásy, L., 2012. Heterogeneous crystal nucleation: the effect of lattice mismatch. Phys. Rev. Lett. 108, 025502.
(Trampuž et al., 2021)	Trampuž, M., Teslić, D., Likozar, B., 2021. Crystal-size distribution-based dynamic process modelling, optimization, and scaling for seeded batch cooling crystallization of Active

	Pharmaceutical Ingredients (API). Chem. Eng. Res. Des. 165, 254-269.
(Tung et al., 2009)	Tung, H.-H., Paul, E.L., Midler, M., McCauley, J.A. , 2009. Crystallization of Organic Compounds: An Industrial Perspective, Wiley-AIChE.
(Vekilov, 2007)	Vekilov, P.G., 2007. What Determines the Rate of Growth of Crystals from Solution? Cryst. Growth Des. 7 (12), 2796-2810.
(Velikov, 2002)	Velikov, K.P., Christova, C.G., Dullens, R.P., van Blaaderen, A., 2002. Layer-by-layer growth of binary colloidal crystals. Science 296(5565), 106-9.
(Vent, 1975)0	Vent, W., 1975. Evolutionsstrategie — Optimierung technischer Systeme nach Prinzipien der biologischen Evolution. Frommann-Holzboog-Verlag. Stuttgart.
(Vikhar, 2016)	Vikhar, P.A., 2016. Evolutionary algorithms: A critical review and its future prospects. 2016 International Conference on Global Trends in Signal Processing, Information Computing and Communication (ICGTSPICC), 261-265.
(Wadell, 1935)	Wadell H., 1933. Sphericity and Roundness of Rock Particles, J. Geol. 41(3), 310–331.
(Wei et al., 2017)	Wei, X., Tanaka, T., Hirakawa, T., Yomogida, Y., Kataura, H., 2017. Determination of Enantiomeric Purity of Single-Wall Carbon Nanotubes Using Flavin Mononucleotide. J. Am. Chem. Soc. 139 (45), 16068-16071.
(West, 2011)	West, C., 2011. Chiral recognition in separation methods. Mechanisms and applications. Anal Bioanal Chem 400, 5–6.
(Wikipedia, 2008)	Growth models, 2008; from https://en.wikipedia.org/wiki/Crystal_growth
(Wolfe, 1969)	Wolfe, P., 1969. Convergence Conditions for Ascent Methods. SIAM Rev., 11(2), 226–235.
(Wong et al., 2012)	Wong, S.Y., Tatusko, A.P., Trout, B.L., Myerson, A.S. , 2012. Development of Continuous Crystallization Processes Using a Single-Stage Mixed-Suspension, Mixed-Product Removal Crystallizer with Recycle. Cryst. Growth Des. 12 (11), 5701-5707.
(Worlitschek and Mazzotti, 2004)	Worlitschek, J., Mazzotti, M., 2004. Model-Based Optimization of Particle Size Distribution in Batch-Cooling Crystallization of Paracetamol. Cryst. Growth Des. 4 (5), 891-903.
(Wu et al., 2015)	Wu, J., Huang, D., Pang, K., Hsu, S., Tyring, S., 2015. Thalidomide: dermatological indications, mechanisms of action and side-effects. Br. J. Dermatol. 153, 254-273.
(Wunderlich, 1993)	Wunderlich, B., 1993. Unsolved Problems of Crystallization and Melting of Flexible Macromolecules. Crystallization of Polymers. NATO ASI ser., Ser. B. Phys. 405.
(Xiouras, 2019)	Xiouras, C. 2019. Intensified Crystallization Processes for the Separation of Enantiomers. Ph.D. thesis. Katholieke Universiteit Leuven, Leuven.
(Yang and Nagy, 2014)	Yang, Y., Nagy, Z.K., 2014. Model-Based Systematic Design and Analysis Approach for Unseeded Combined Cooling and Antisolvent Crystallization (CCAC) Systems. Cryst. Growth Des. 14 (2), 687-698.
(Yu et al., 2004)	Yu, L.X., Lionberger, R.A., Raw, A.S., DÕCosta, R., Wu, H., Hussain, A.S., 2004. Applications of process analytical

	technology to crystallization processes. Adv. Drug Delivery Rev. 56, 349–369.
(Yu et al., 2007)	Yu, Z.-Q., Chew, J. W., Chow, P., Tan, R.B.H., 2007. Recent Advances in Crystallization control: An Industrial Perspective. Adv. Drug Delivery Rev. 85, 893-905.
(Zhang et al., 2012)	Zhang, H., Alvarez, A.J., Quon, J.,Evans, J., Myerson, A.S., Trout, B., 2012. Development of Continuous Anti-Solvent/Cooling Crystallization Process using Cascaded Mixed Suspension, Mixed Product Removal Crystallizers. Org. Process Res. Dev. 16 (5), 915-924.
(Zhang et al., 2017)	Zhang, D., Xu, S., Du,S., Wang, J., Gong, J., 2017. Progress of Pharmaceutical Continuous Crystallization, Engineering 3(3), 354-364.
(Zhao et al., 2007)	Zhao, H., Maisels, A., Matsoukas, T., Zheng, C., 2007. Analysis of Four Monte Carlo Methods for the Solution of Population Balances in Dispersed Systems. Powder Technol. 173, 38-50.
[Huskova et al., 2021, ISIC]	Huskova, N., Mangold, M., Lorenz, H., & Seidel-Morgenstern, A. (2021). Crystallizer geometry optimization applying the process model for the Separation of Enantiomers by Preferential Crystallization. Poster presented at ISIC 21 - 21st International Symposium on Industrial Crystallization, Virtually.
[Huskova et al., 2021, ProcessNet]	Huskova, N., Mangold, M., Lorenz, H., & Seidel-Morgenstern, A. (2021). Improvement and optimization of the process model for the Separation of Enantiomers by Preferential Crystallization. Talk presented at Jahrestreffen der ProcessNet-Fachgruppe Kristallisation 2021. virtuell. 2021-03-18 - 2021-03-19.

List of symbols

$A(h)$	Cross-section area	m^2
A_F	Cross-section area free of particles	m^2
av_{in}	Mean size of initial seeds	Mm
B_{nuc}	Nucleation rate	$\mathrm{m}^{-3}\mathrm{s}^{-1}$
b	Fragment distribution function	
c_{in}	Liquid phase inlet concentration of enantiomer (D or L)	$kg_{solute}\,kg_{solution}^{-1}$
c	Liquid phase concentration of enantiomer (D or L)	$kg_{solute}\,kg_{solution}^{-1}$
c^*	Liquid phase saturation concentration (D or L)	$kg_{solute}\,kg_{solution}^{-1}$
$c_{p_{liquid}}$	Average heat capacity of the liquid	$\mathrm{J\,kg}^{-1}\mathrm{K}^{-1}$
$c_{p_{solid}}$	Heat capacity of the solid phase	$\mathrm{J\,kg}^{-1}\mathrm{K}^{-1}$
c_W	Drag coefficient	
E_g	Activation energy of growth	kJmol^{-1}
F_B	Buoyancy force	$kgms^{-2}$
F_D	Drag force	$kgms^{-2}$
F_G	Gravity force	$kgms^{-2}$
G	Grow rate	ms^{-1}
g	Standard gravity	ms^{-2}
H	Total length of crystallizer	m
H_1	Height of conical section of crystallizer	m
H_2	Height of cylindrical section of crystallizer	m
H_{Prod}	Position of the product outlet	m
h	Height coordinate of crystallizer	m
h_{liquid}	Liquid enthalpy at reference temperature	Jkg^{-1}
h_M	Position of mill connection	
h_S	Position of the upper sensor	m
h_{solid}	Particle enthalpy at reference temperature	Jkg^{-1}
i	Index for one enantiomer	
j	Index for other enantiomer	
$K_1 \ldots K_4$	Solubility parameters	
K_i	Integral coefficient	
K_p	Proportional coefficient	
k_g	Growth rate constant	ms^{-1}
L	Internal coordinate/particle diameter	µm

L_c	Critical crystal size	µm
m	Mass of crystalline material	kg
$m(L)$	Mass of a particle of size L	kg
$\dot{m}$	Mass flow	kg s^{-1}
m_k	Moment of distribution	
m_{in}	Mass of initial seeding crystals	
N_{total}	Total number of particles	
$n(h, L, t)$	Number size density of crystals	$\mathrm{m^{-3}m^{-1}}$
$\hat{n}(h, L, t)$	Net number of particles introduced to system	
n_g	Growth rate order	
$n_M(L, t)$	Number size density of crystals in the mill	$\mathrm{m^{-3}m^{-1}}$
Pr	Productivity	$\mathrm{g\ L^{-1}h^{-1}}$
p	Number of daughters coming from mill	
p_j	Variable parameter for the sensitivity analysis	
R	Universal gas constant	$JK^{-1}mol^{-1}$
R_1	Radius at the crystallizer inlet	m
R_2	Radius of the cylindrical section	m
S	Supersaturation	
S_{kj}	Sensitivity	
$S1$	Upper photo sensor	
$S2$	Lower photo sensor	
S_b	Breakage kernel	
S_0	Kinetic parameter in breakage kernel	
s_{L3}	Standard deviation	µm
t	Time	s
T	Temperature	$℃/K$
T_{cool}	Coolant temperature	$℃/K$
T_{cryst}	Temperature (at middle position)	$℃/K$
T_{in}	Inlet temperature	$℃/K$
T_{out}	Temperature at outlet position	$℃/K$
T_{sat}	Saturation temperature	$℃/K$
$u_{empty\ tube}$	Empty tube velocity of liquid phase	$\mathrm{ms^{-1}}$
υ_p	Particle velocity	$\mathrm{ms^{-1}}$
υ_f	Fluid velocity	$\mathrm{ms^{-1}}$
V_F	Volume of liquid	$\mathrm{m^3}$

V_M	Volume of mill	m^3
V_p	Volume occupied by particles	m^3
V_{Prod}	Volume of withdrawn product suspension	m^3
V_{sec}	Volume of crystallizer section	m^3
V_{total}	Total volume of crystallizer	m^3
$\dot{V}_{in}$	Volumetric feed flow rate	$\mathrm{m}^3\mathrm{s}^{-1}$
$\dot{V}_M$	Volumetric flow rate to/from particle mill	$\mathrm{m}^3\mathrm{s}^{-1}$

Greek symbols

α	Cone opening angle	°
α_{cool}	Heat transfer coefficient	$\mathrm{W\ m}^{-2}\mathrm{K}^{-1}$
σ_{in}	Standard deviation of initial crystal distribution	µm
$\epsilon(h)$	Volume fraction of the fluid	
$\epsilon_{desired}$	Desired fluid fraction at sensor position	
ΔH_{cryst}	Crystallization enthalpy	Jkg^{-1}
Δh_p	Height of withdrawn product suspension	m
Δh_S	Distance between S1 and S2	m
ρ_{liquid}	Average liquid density	kgm^{-3}
ρ_{solid}	Density of the solid phase	kgm^{-3}
Δt	Interval between product withdrawals	h
ΔT	Temperature difference	$℃/K$
φ	Sphericity	
ω	Density difference	kgm^{-3}

Abbreviations

Asn·H_2O	Asparagine monohydrate-water
CMA-ES	Covariance matrix adaptation evolution strategy
COBC	Continuous oscillatory baffled crystallizer
CPC	Continuous preferential crystallization
CPM	Continuous pharmaceutical manufacturing
C-ref-L	Left crystallizer with the reference geometry
CSD	Crystal size distribution
D- Asn·H_2O	D-Asparagine monohydrate-water
D-ref-L	Right crystallizer with the reference geometry
FBC	Fluidized bed crystallizer
FDA	Food and Drug Administration
FDM	Finite-difference methods
FEM	Finite element methods
FVM	Frank-van der Merwe theory of crystal growth
FVM	Finite-volume methods
HIV	Human immunodeficiency viruses
L- Asn·H_2O	L-Asparagine monohydrate-water
MOL	Method of lines
MPC	Model predictive control
MSMPR	Mixed suspension mixed product crystallizer
ODE	Ordinary differential equation
PAT	Process analytical technology
PBE	Population balance equation
PBM	Population balance modelling
PDE	Partial differential equation
PFR	Plug flow reactor
PSD	Particle size distribution
QbD	Quality by design
SIMD	Single instruction multiple data
SISD	Single instruction single data
SK	Stranski-Krastanov model of crystal growth
SLE	Solid-Liquid Equilibria
SMOM	Standard method of moments
VW	Volmer-Weber crystal growth theory

Appendix I. Simulation results for the D Crystallizer

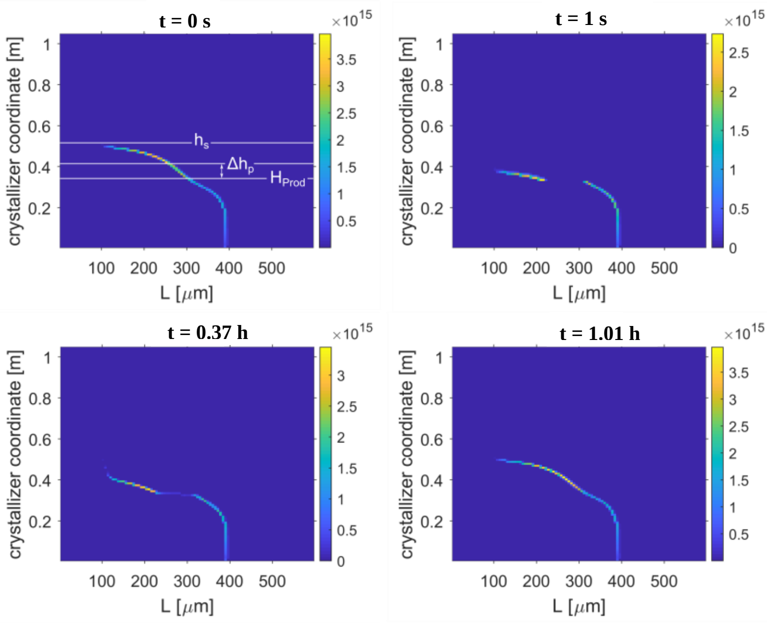

Figure A1. Simulated number size densities $n(h, L, t)$ for the parameters corresponding to the D-crystallizer (Parameters are listed in Table 4.3). The figure shows four snapshots illustrating the location of different sizes of crystals within the crystallizer covering a period of 1 h: Immediately before product removal, immediately after product removal, at a later time point during the cycle, and finally at the end of the cycle (right before the next product removal).

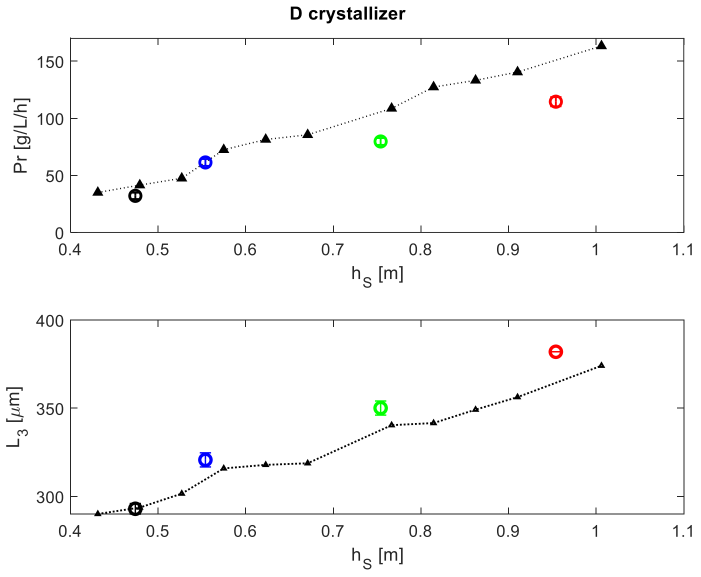

Figure A2. Influence of the upper sensor position, h_S, on the productivity, Pr (left), and the mean product crystal size, L_3. Black points mark the simulated productivity and mean crystal size for the different withdrawal strategies (see Table 4.6) in different crystallizer runs. Simulated values of the productivity and mean crystal size are marked blue. The height of the withdrawn segment (Δh_p) is equal 0.12 m for the first strategy (when $h_s = 0.49\ m$), and 0.085m for all others applied strategies. Shown simulation results correspond to crystallizer Cref-D, geometry and operating parameters are given in Table 4.3.

Appendix II. Derivation of the energy balance and the temperature equation

In the following, it is assumed that there is no difference between the solid and the liquid phase. The energy balance for a volume element with cross-sectional area $A(h)$ and height Δh gives

$$\begin{aligned}
&\frac{d}{dt}\cdot\left(A(h)\cdot\Delta h\cdot\epsilon\cdot\rho_{liquid}\cdot h_{liquid}+\ A(h)\cdot\Delta h\cdot\epsilon\cdot\int_0^\infty n\cdot\frac{\pi}{6}\cdot L^3\cdot\rho_{solid}\cdot h_{solid}\cdot dL\right)\\
&=\ \dot{V}\cdot\rho_{liquid}h_{liquid}(h)-\ \dot{V}\cdot\rho_{liquid}h_{liquid}(h+\Delta h)\\
&+A\cdot\Delta h\cdot\int_0^\infty n(h,L,t)\cdot\frac{\pi}{6}\cdot L^3\cdot v_p(h,L)\cdot\rho_{solid}\cdot h_{solid}\cdot dL\\
&-A\cdot\Delta h\cdot\int_0^\infty n(h+\Delta h,L,t)\cdot\frac{\pi}{6}\cdot L^3\cdot v_p(h+\Delta h,L)\cdot\rho_{solid}\cdot h_{solid}\cdot dL\\
&+\dot{V}_M\cdot\int_h^{h+\Delta h}\int_0^\infty(n_M(L,t)\cdot\frac{\pi}{6}\cdot L^3\cdot\rho_{solid}h_{solid}(T_M)-n(h,L,t)\cdot\frac{\pi}{6}\cdot L^3\\
&\qquad\qquad\cdot\rho_{solid}h_{solid}(T))\cdot dL\cdot\delta\cdot(h-h_M)\cdot\Delta h\\
&+\dot{q}_{cool}\cdot\Delta h\cdot A_{HE}
\end{aligned}$$

[Eq.A.1]

In the above equation, the first line on the right-hand side stands for enthalpy transport with the liquid phase, the following two lines for enthalpy transported by particles into and out of the control volume, the fourth line contains enthalpy exchange between mill and crystallizer. The fifths line describes the heat flux from the coolant.

$$\dot{q}_{cool}=\alpha\cdot(T_{cool}-T)$$

[Eq.A.2]

Equation [Eq.A.2] determines the heat flux density per unit area, where A_{HE} is the heat exchange area per unit length. For a cylindrical crystallizer it is described by

$$A_{HE}=\pi\cdot d$$

[Eq.A.3]

The limiting case $\Delta h\rightarrow 0$ simplifies the energy balance equation to

$$\begin{aligned}
&\frac{d}{dt}\cdot\left(A(h)\cdot\epsilon\cdot\rho_{liquid}\cdot h_{liquid}+\ A(h)\cdot\epsilon\cdot\int_0^\infty n\cdot\frac{\pi}{6}\cdot L^3\cdot\rho_{solid}\cdot h_{solid}\cdot dL\right)\\
&=-\frac{\partial}{\partial h}\cdot\left(\ \dot{V}\cdot\rho_{liquid}h_{liquid}(h)\right)\\
&-\ -\frac{\partial}{\partial h}\cdot\left(A\cdot\int_0^\infty n(h,L,t)\cdot\frac{\pi}{6}\cdot L^3\cdot v_p(h,L)\cdot\rho_{solid}\cdot h_{solid}\cdot dL\right)\\
&+\dot{V}_M\cdot\int_0^\infty\left(n_M(L,t)\cdot\frac{\pi}{6}\cdot L^3\cdot\rho_{solid}h_{solid}(T_M)-n(h,L,t)\cdot\frac{\pi}{6}\cdot L^3\cdot\rho_{solid}h_{solid}(T)\right)\\
&\qquad\qquad\cdot dL\cdot\delta\cdot(h-h_M)\\
&+\dot{V}_M\cdot\left(\rho_{liquid}h_{liquid}(T_M)-\rho_{liquid}h_{liquid}(T)\right)\cdot\delta\cdot(h-h_M)\\
&+\alpha\cdot\pi\cdot d\cdot(T_{cool}-T)
\end{aligned}$$

[Eq.A.4]

Since $\int_0^\infty n \cdot \frac{\pi}{6} \cdot L^3 \cdot dL = 1 - \epsilon$, the left side of the [Eq.A.4] can be replaced as

$$\frac{d}{dt} \cdot \left(A(h) \cdot \epsilon \cdot \rho_{liquid} \cdot h_{liquid} + A(h) \cdot \int_0^\infty n \cdot \frac{\pi}{6} \cdot L^3 \cdot \rho_{solid} \cdot h_{solid} \cdot dL \right)$$
$$= \frac{d}{dt} \cdot \left(A(h) \cdot \epsilon \cdot \rho_{liquid} \cdot h_{liquid} + A(h) \cdot (1 - \epsilon) \cdot \rho_{solid} \cdot h_{solid} \right)$$

[Eq.A.5]

Considering the total mass balance equation given in Chapter 3 of this work [Eq.3.27], the following equation may be written as follows

$$A(h) \cdot \left(\epsilon \cdot \rho_{liquid} \cdot h_{liquid} \right) \cdot \frac{\partial}{\partial t}$$
$$= A \cdot \epsilon \cdot \rho_{liquid} \cdot \frac{\partial h_{liquid}}{\partial t} + A \cdot h_{liquid} \cdot \frac{\partial}{\partial t} \left(\epsilon \cdot \rho_{liquid} \right)$$
$$= A \cdot \epsilon \cdot \left(\rho_{liquid} \cdot c_{p_{liquid}} \right) \cdot \frac{\partial T}{\partial t}$$
$$+ h_{liquid} \cdot \left(-\frac{\partial}{\partial h} \cdot \left(\dot{V} \cdot \rho_{liquid} \right) + \rho_{solid} \cdot A \cdot \int_0^\infty G \cdot \frac{\partial n}{\partial L} \cdot \frac{\pi}{6} \cdot L^3 \cdot \partial L \right)$$

[Eq.A.6]

By using the population balance equation [Eq.3.10], relation for the solid phase reads

$$A \cdot \frac{\partial}{\partial t} \cdot \left(\int_0^\infty n \cdot \frac{\pi}{6} \cdot L^3 \cdot \partial L \cdot \rho_{solid} \cdot h_{solid} \right)$$
$$= A \cdot \rho_{solid} \cdot h_{solid} \cdot \int_0^\infty \frac{\partial n}{\partial t} \cdot \frac{\pi}{6} \cdot L^3 \cdot dL + A \cdot \int_0^\infty n \cdot \frac{\pi}{6} \cdot L^3 \cdot dL \cdot \rho_{solid} \cdot c_{p_{solid}} \cdot \frac{\partial T}{\partial t}$$
$$+ A \cdot (1 - \epsilon) \cdot \rho_{solid} \cdot c_{p_{solid}} \cdot \frac{\partial T}{\partial t} + A \cdot \rho_{solid} \cdot h_{solid} \cdot \int_0^\infty \frac{\partial n}{\partial t} \cdot \frac{\pi}{6} \cdot L^3 \cdot dL$$
$$= A \cdot (1 - \epsilon) \cdot \rho_{solid} \cdot c_{p_{solid}} \cdot \frac{\partial T}{\partial t} + \rho_{solid} \cdot h_{solid} \cdot \int_0^\infty \frac{\pi}{6} \cdot L^3 \cdot \left(-\frac{\partial}{\partial h} \cdot \left(A \cdot v_p \cdot n \right) \right.$$
$$\left. - A \cdot G \cdot \frac{\partial n}{\partial L} + \dot{V}_M \cdot (n_M - n) \cdot \delta \cdot (h - h_M) \cdot dL \right.$$

[Eq.A.7]

Inserting [Eq.A.6] and [Eq.A.7] into the energy balance gives

$$A \cdot \epsilon \cdot \rho_{liquid} \cdot c_{p_{liquid}} \cdot \frac{\partial T}{\partial t}$$
$$+ A \cdot (1 - \epsilon) \cdot \rho_{solid} \cdot c_{p_{solid}} \cdot \frac{\partial T}{\partial t}$$
$$+ h_{liquid} \cdot \left(-\frac{\partial}{\partial h} \cdot \left(\dot{V} \cdot \rho_{liquid} \right) + \rho_{solid} \cdot A \cdot \int_0^\infty G \cdot \frac{\partial n}{\partial L} \cdot \frac{\pi}{6} \cdot L^3 \cdot dL \right)$$
$$+ \rho_{solid} h_{solid}(T)$$
$$\cdot \int_0^\infty \frac{\pi}{6} \cdot L^3 \cdot \left(-\frac{\partial}{\partial h} \cdot \left(A \cdot v_p \cdot n \right) - A \cdot G \cdot \frac{\partial n}{\partial L} + \dot{V}_M \cdot (n_M - n) \cdot \delta \right.$$
$$\left. \cdot (h - h_M) \right) \cdot dL$$

$$
\begin{aligned}
&= -h_{liquid} \cdot \frac{\partial}{\partial h} \cdot \left(\dot{V} \cdot \rho_{liquid}\right) - \dot{V} \cdot \left(\rho_{liquid} \cdot c_{p_{liquid}}\right) \cdot \frac{\partial T}{\partial h} \\
&-\rho_{solid} \cdot h_{solid} \cdot \frac{\partial}{\partial h} \cdot \left(A \cdot \int_0^\infty n \cdot \frac{\pi}{6} \cdot L^3 \cdot v_p \cdot dL\right) \\
&-A \cdot \int_0^\infty n \cdot \frac{\pi}{6} \cdot L^3 \cdot v_p \cdot dL \cdot \rho_{solid} \cdot c_{p_{solid}} \cdot \frac{\partial T}{\partial h} \\
&+\dot{V}_M \cdot \int_0^\infty \left(n_M \cdot \frac{\pi}{6} \cdot L^3 \cdot \rho_{solid} h_{solid}(T_M) - n \cdot \frac{\pi}{6} \cdot L^3 \cdot \rho_{solid} h_{solid}(T)\right) \cdot dL \cdot \delta \cdot (h - h_M) \\
&+\dot{V}_M \cdot \left(\rho_{liquid} h_{liquid}(T_M) - \rho_{liquid} h_{liquid}(T)\right) \cdot \delta \cdot (h - h_M) \\
&+\alpha \cdot \pi \cdot d \cdot (T_{cool} - T)
\end{aligned}
$$

[Eq.A.8]

Cancelling the same terms, [Eq.A.8] can be rearranged

$$
\begin{aligned}
&A \cdot \epsilon \cdot \rho_{liquid} \cdot c_{p_{liquid}} \cdot \frac{\partial T}{\partial t} + A \cdot (1 - \epsilon) \cdot \rho_{solid} \cdot c_{p_{solid}} \cdot \frac{\partial T}{\partial t} \\
&+ h_{liquid} \cdot \rho_{solid} \cdot A \cdot \int_0^\infty G \cdot \frac{\partial n}{\partial L} \cdot \frac{\pi}{6} \cdot L^3 \cdot dL \\
&+ \rho_{solid} h_{solid}(T) \cdot \int_0^\infty \frac{\pi}{6} \cdot L^3 \cdot \left(-A \cdot G \cdot \frac{\partial n}{\partial L} + \dot{V}_M \cdot (n_M - n) \cdot \delta \cdot (h - h_M)\right) \cdot dL = \\
&- \dot{V} \cdot \rho_{liquid} \cdot c_{p_{liquid}} \cdot \frac{\partial T}{\partial h} \\
&- A \cdot \int_0^\infty n \cdot \frac{\pi}{6} \cdot L^3 \cdot v_p \cdot dL \cdot \rho_{solid} \cdot c_{p_{solid}} \cdot \frac{\partial T}{\partial x} \\
&+ \dot{V}_M \cdot \int_0^\infty \left(n_M \cdot \frac{\pi}{6} \cdot L^3 \cdot \rho_{solid} h_{solid}(T_M) - n \cdot \frac{\pi}{6} \cdot L^3 \cdot \rho_{solid} h_{solid}(T)\right) \cdot dL \cdot \delta \cdot (h - h_M) \\
&+ \dot{V}_M \cdot \left(\rho_{liquid} h_{liquid}(T_M) - \rho_{liquid} h_{liquid}(T)\right) \cdot \delta \cdot (h - h_M) \\
&+ \alpha \cdot \pi \cdot d \cdot (T_{cool} - T)
\end{aligned}
$$

$$\Leftrightarrow$$

$$
\begin{aligned}
&\left(A \cdot \epsilon \cdot \rho_{liquid} \cdot c_{p_{liquid}} + A \cdot (1 - \epsilon) \cdot \rho_{solid} \cdot c_{p_{solid}}\right) \cdot \frac{\partial T}{\partial t} \\
&+ \Delta H_{cryst} \cdot \rho_{solid} \cdot \mathrm{A} \cdot \int_0^\infty G \cdot \frac{\partial n}{\partial L} \cdot \frac{\pi}{6} \cdot L^3 \cdot dL \\
&+ \rho_{solid} h_{solid}(\mathrm{T}) \cdot \int_0^\infty \frac{\pi}{6} \cdot L^3 \cdot \dot{V}_M \cdot n_M \cdot \delta \cdot (h - h_M) \cdot dL \\
&- \rho_{solid} h_{solid}(\mathrm{T}) \cdot \int_0^\infty \frac{\pi}{6} \cdot L^3 \cdot \dot{V}_M \cdot n \cdot \delta \cdot (h - h_M) \cdot dL \\
&= \left(- \dot{V} \cdot \rho_{liquid} \cdot c_{p_{liquid}} - A \cdot \int_0^\infty n \cdot \frac{\pi}{6} \cdot L^3 \cdot v_p \cdot dL \cdot \rho_{solid} \cdot c_{p_{solid}}\right) \cdot \frac{\partial T}{\partial h} \\
&+ \dot{V}_M \cdot \int_0^\infty \left(n_M \cdot \frac{\pi}{6} \cdot L^3 \cdot \rho_{solid} h_{solid}(T_M)\right) \cdot dL \cdot \delta \cdot (h - h_M) \\
&- \dot{V}_M \cdot \int_0^\infty \left(n_M \cdot \frac{\pi}{6} \cdot L^3 \cdot \rho_{solid} h_{solid}(T)\right) \cdot dL \cdot \delta \cdot (h - h_M) \\
&+ \dot{V}_M \cdot \left(\rho_{liquid} h_{liquid}(T_M) - \rho_{liquid} h_{liquid}(T)\right) \cdot \delta \cdot (h - h_M)
\end{aligned}
$$

$$+\ \alpha \cdot \pi \cdot d \cdot (T_{cool} - T)$$

[Eq.A.9]

Cconsidering the differences between the two types of enantiomers marked as index i / j, the final temperature equation is as follows

$$\begin{aligned}
&\Big(A(h) \cdot \epsilon \cdot (\rho_{liquid} \cdot c_{p_{liquid}}) + A(h) \cdot (1-\epsilon) \cdot \ \rho_{solid} \cdot c_{p_{solid}}\Big) \cdot \frac{\partial T}{\partial t} = \\
&- \Bigg(\dot{V}\ \cdot \rho_{liquid} \cdot c_{p_{liquid}} - A \cdot \rho_{solid} \cdot c_{p_{solid}} \\
&\qquad\qquad \cdot \left(\int_0^\infty v_{p,i} \cdot n_i \cdot \frac{\pi}{6} \cdot L_i^3 \cdot dL_i + \int_0^\infty v_{p,j} \cdot n_j \cdot \frac{\pi}{6} \cdot L_j^3 \cdot dL_j\right)\Bigg) \cdot \frac{\partial T}{\partial h} \\
&- \Delta H_{cryst} \cdot \rho_{solid} \cdot \mathrm{A} \cdot \left(\int_0^\infty G \cdot \frac{\partial n_i}{\partial L_i} \cdot \frac{\pi}{6} \cdot L_i^3 \cdot dL_i + \int_0^\infty G \cdot \frac{\partial n_j}{\partial L_j} \cdot \frac{\pi}{6} \cdot L_j^3 \cdot dL_j\right) \\
&+ \dot{V}_M \cdot \left((\rho_{liquid} \cdot c_{p_{liquid}}) + \rho_{solid} \cdot c_{p_{solid}} \cdot \int_0^\infty n_M \cdot \frac{\pi}{6} \cdot L^3 \cdot dL\right) \cdot (T_M - T) \\
&\qquad\qquad \cdot \delta(h - h_M) \\
&+ \alpha_{cool}\ \cdot \pi\ \cdot (T_{cool} - T)
\end{aligned}$$

[Eq.A.10]